VISUAL PROCESSING OF NATURALISTIC IMAGES: FREE VIEWING, GUIDED VISUAL SEARCHING, AND MEMORIZATION

Von der Fakultät für Mathematik, Informatik und Naturwissenschaften der RWTH Aachen University zur Erlangung des akademischen Grades eines Doktors der Naturwissenschaften genehmigte Dissertation

vorgelegt von

Christian Matthias Kiefer
Master of Science

aus

Köln

Berichter:

Universitätsprofessor Dr. rer. nat. N. Jon Shah
Universitätsprofessor Dr. rer. nat. Sonja Grün
Universitätsprofessor Dr. rer. nat. Ansgar Steland

Tag der mündlichen Prüfung: 28.08.2023

EIDESSTATTLICHE ERKLÄRUNG

Ich, Christian Matthias Kiefer,

erkläre hiermit, dass diese Dissertation und die darin dargelegten Inhalte die eigenen sind und selbstständig, als Ergebnis der eigenen originären Forschung, generiert wurden.

Hiermit erkläre ich an Eides statt:

1. Diese Arbeit wurde vollständig oder größtenteils in der Phase als Doktorand dieser Fakultät und Universität angefertigt;
2. Sofern irgendein Bestandteil dieser Dissertation zuvor für einen akademischen Abschluss oder eine andere Qualifikation an dieser oder einer anderen Institution verwendet wurde, wurde dies klar angezeigt;
3. Wenn immer andere eigene- oder Veröffentlichungen Dritter herangezogen wurden, wurden diese klar benannt;
4. Wenn aus anderen eigenen- oder Veröffentlichungen Dritter zitiert wurde, wurde stets die Quelle hierfür angegeben. Diese Dissertation ist vollständig meine eigene Arbeit, mit der Ausnahme solcher Zitate;
5. Alle wesentlichen Quellen von Unterstützung wurden benannt;
6. Wenn immer ein Teil dieser Dissertation auf der Zusammenarbeit mit anderen basiert, wurde von mir klar gekennzeichnet, was von anderen und was von mir selbst erarbeitet wurde;
7. Ein Teil oder Teile dieser Arbeit wurden zuvor veröffentlicht in:

   Kiefer, Christian M., Junji Ito, Ralph Weidner, Frank Boers, Nadim Jon Shah, Sonja Grün, and Jürgen Dammers. 2022. "Revealing Whole-Brain Causality Networks during Guided Visual Searching." *Frontiers in Neuroscience* 16. https://www.frontiersin.org/articles/10.3389/fnins.2022.826083/full

_____ _____

Ort, Datum Unterschrift

ZUSAMMENFASSUNG

Unter natürlichen Bedingungen werden Augenbewegungen dazu genutzt, um aktiv visuelle Informationen über die Umgebung zu sammeln. Dieser Prozess wird auch „aktives Sehen“ („active vision“) genannt. Obwohl solche Augenbewegungen die Basis für das Sehen im Alltag bilden, hat sich die Forschung in der Vergangenheit oft auf vereinfachte, künstliche Szenarien mit eingeschränkten Augenbewegungen konzentriert. Die Mechanismen des aktiven Sehens sind daher im Vergleich noch weitgehend unerforscht. Insbesondere ist es noch unklar, wie zielgerichtetes Verhalten, z.B. im Rahmen der Suche nach einem bestimmten Objekt, die visuelle Verarbeitung beeinflusst. In dieser Dissertation wurden in einer Studie mit 31 Probanden drei Arten des aktiven Sehens untersucht: eine zielgerichtete Suche, eine Gedächtnisaufgabe und das freie Betrachten. Für alle drei Aufgaben wurden den Probanden lebensnahe Bilder mit eingebetteten Objekten präsentiert.
Um die Frage, wie zielgerichtetes Verhalten die visuelle Verarbeitung beeinflusst, zu beantworten, wurden die kausalen Verbindungen im Gehirn für die Suchaufgabe und das freie Betrachten bestimmt. Die so entstandenen Netzwerke wurden anschließend miteinander verglichen. Zunächst wurden dafür Regionen mit signifikanter, Fixations-bezogener evozierter Aktivität mittels „spatiotemporal cluster permutation testing“ bestimmt. Anschließend wurden zwischen diesen Regionen Netzwerke von direktionalen Verbindungen mittels „generalized partial directed coherence“ berechnet. Vier Regionen, der *Gyrus supramarginalis*, der *Gyrus temporalis superior*, die *Gyri temporali transversi*, und die hintere Inselrinde, formten zusammen während des freien Betrachtens einen Cluster in beiden Hemisphären, welcher äußerst stark vernetzt war. Ein nahezu identischer Cluster entstand ebenfalls während der Suchaufgabe in der rechten Hemisphäre, wobei der *Gyrus supramarginalis* einen zentralen Knotenpunkt in den Netzwerken bildete. Basierend auf diesen Ergebnissen ist es wahrscheinlich, dass alle vier Regionen an der Steuerung der Aufmerksamkeit und an der visuellen Verarbeitung beteiligt sind. Insbesondere könnte der rechte *Gyrus supramarginalis* für die Integration von visuellen, Objekt-bezogenen Informationen zuständig sein. Des Weiteren könnte eine Verbindung darauf hinweisen, dass der rechte *Gyrus supramarginalis* das supplementäre Augenfeld mit Informationen versorgt, um die Prioritätskarte, welche die Augenbewegungen zum Zielobjekt leitet, zu aktualisieren.

Zum Abschluss wurde der auf Zeitreihen basierende „random convolutional kernel transformation” (ROCKET) Klassifikator auf die Fixations-bezogene evozierte Aktivität von Objektfixationen, welche während der Gedächtnisaufgabe und während des freien Betrachtens durchgeführt wurden, angewandt. Zuvor ungesehene Fixationsdaten konnten mit einer Genauigkeit von 93 % erfolgreich klassifiziert werden. Mit der gleichen Methode konnten die Ruhemessungen von verschiedenen Probanden ebenfalls mit einer Genauigkeit von 93 % voneinander unterschieden werden. Dies scheint der erste Machbarkeitsnachweis für neuronale Fingerabdrücke basierend auf Zeitreihen mittels ROCKET zu sein.

ABSTRACT

Under natural conditions, eye movements are used to actively gather visual information from the environment, a process referred to as 'active vision'. Despite active vision forming the basis for visual exploration in everyday life, research has often focused on simplified, artificial scenarios with restricted eye movements. As a result, the mechanisms underlying active vision remain comparatively unexplored. Particularly, it is unclear how goal-directed behavior such as during the search for a particular object influences the visual processing during active vision. In this dissertation, three distinct modes of active vision were investigated in a study of 31 subjects: performing a guided visual search and memorizing objects were compared to the free viewing of naturalistic images. Magnetoencephalography was used in conjunction with an eye-tracking system to simultaneously record the brain activity and the eye movements during the tasks while the subjects were viewing naturalistic images with embedded objects.
To answer the question of how visual processing is affected by goal-directed behavior, causal interactions in the brain were compared for the free viewing and the visual searching tasks. First, regions of interest exhibiting significant fixation-related evoked activity were determined using spatiotemporal cluster permutation testing. Then, using generalized partial directed coherence, the whole-brain causality networks between these regions were computed. Four regions, namely the supramarginal gyrus, the superior temporal gyrus, the transverse temporal gyri, and the posterior insula, formed during free viewing a cluster in both hemispheres that was highly inter-connected. A near-identical cluster emerged during searching in the right hemisphere with the right supramarginal gyrus as a central node in the network. Based on the results, all four regions are likely involved in guiding attention and visual processing. Specifically, the right supramarginal gyrus might be involved in the integration of visual input related to objects. Furthermore, it might provide the supplementary eye field with information for the purpose of updating the search priority map, which guides the eye movements towards the search target.

Finally, the random convolutional kernel transformation (ROCKET) classifier for time series was applied to the fixation-related evoked activity of object fixations performed during the memorization and the free viewing tasks. It was possible to classify unseen fixation data based on the task with 93% accuracy. Furthermore, with the same method it was also possible to differentiate between subjects based on resting-state recordings with 93% accuracy. This appears to be the first proof of concept that neuronal fingerprinting can be achieved directly on time series data using ROCKET.

TABLE OF CONTENTS

ABBREVIATIONS

AIC	Akaike information criterion
AR(p)	Autoregressive model of order p
BIC	Bayesian information criterion
dc SQUID	Direct current superconducting quantum interference device
DSM	Distributed source model
dSPM	Dynamic statistical parametric map
EEG	Electroencephalography
FDR	False discovery rate
FIF	Fractal image format
fMRI	Functional magnetic resonance imaging
FRA	Fixation-related evoked activity
FRP	Fixation-related evoked potential
FV	Free viewing
FWER	Family-wise error rate
GPDC	Generalized partial directed coherence
HQIC	Hannan-Quinn information criterion
ICA	Independent component analysis
M1	Primary motor cortex
MCP	Multiple comparison problem
ME	Memorizing
MEG	Magnetoencephalography
MFS	Modulation and feedback signal
MNE	Minimum-norm estimates
MRI	Magnetic resonance imaging
MVAR(p)	Multivariate autoregressive model of order p
PDC	Partial directed coherence
rf SQUID	Radio frequency superconducting quantum interference device
ROCKET	Random convolutional kernel transformation
S1	Primary somatosensory cortex
SCPT	Spatiotemporal cluster permutation test
SE	Standard error of regression
SI	Sensor input
SNR	Signal-to-noise ratio
SPM	Statistical parametric map
SQUID	Superconducting quantum interference device
TCPT	Temporal cluster permutation testing
TSC	Time series classification
VS	Visual searching

REGIONS OF INTEREST

BSTS	Banks superior temporal sulcus
C	Cuneus
EC	Entorhinal cortex
FG	Fusiform gyrus
ICC	Isthmus cingulate cortex
IPC	Inferior parietal cortex
ITG	Inferior temporal cortex
LG	Lingual gyrus
LOC	Lateral occipital cortex
MTG	Middle temporal gyrus
ParaCeL	Paracentral lobule
PCC	Posterior cingulate cortex
PeriCC	Pericalcarine cortex
PHG	Parahippocampal gyrus
PI	Posterior insula
PreC	Precuneus
SMG	Supramarginal gyrus
SPC	Superior parietal cortex
STG	Superior temporal gyrus
TTG	Transverse temporal gyrus

PHYSICAL UNITS

k	kilo, 10^{3}
m	milli, 10^{-3}
µ	micro, 10^{-6}
n	nano, 10^{-9}
p	pico, 10^{-12}
f	femto, 10^{-15}

Hz	Hertz
m	Meter
s	Seconds
T	Tesla
V	Volt
Wb	Weber

FIGURES

1 INTRODUCTION[1]

In any kind of scientific experiment, conditions are typically tightly controlled in order to isolate specific properties of the subject of interest. With regards to the study of how the human brain processes visual information, this was often achieved by using simple, artificial stimuli such as bars, gratings, letters, or simplified scenarios like reading paradigms (Dimigen et al. 2011; Marton and Szirtes 1988b, 1988a), controlled saccade tasks (Brouwer et al. 2013; Dandekar et al. 2012; Kazai and Yagi 1999; Thickbroom and Mastaglia 1985; Thickbroom et al. 1991; Yagi 1981), or visual search tasks with artificial stimuli (Treisman 1982; Wolfe 1994a). Naturalistic stimuli such as photographs or movies have generally been avoided due to their high complexity.

Although the complexity of studies can be reduced by using artificial stimuli, it is not guaranteed that conclusions drawn from these experiments can be transferred to the more complex cases of naturalistic stimuli or much less to the real world (Rao et al. 2007). In fact, several studies have pointed out discrepancies in the processing of naturalistic stimuli and of simple visual stimuli (Wolfe 1994b; Vinje and Gallant 2000; Ossandón et al. 2010; Snow et al. 2011; Kaunitz et al. 2014; Sonkusare, Breakspear, and Guo 2019; Snow and Culham 2021).

As opposed to the simplified experimental paradigms where continuous fixations on a specific point are required or where the sudden appearance of stimuli trigger the execution of eye movements, natural still images (photographs) are explored through self-paced gaze shifts over longer periods of time ('active vision') (Nikolaev, Meghanathan, and van Leeuwen 2016). From such experiments with unconstrained eye movements, new insights can be gained (Kamienkowski et al. 2012). Unfortunately, it is difficult to draw parallels across subjects and/or trials due to the eye movements being self-paced—the paths taken during the exploration will virtually never be the same for any two trials. However, the combination of high temporal resolution neuroimaging with eye tracking may present a feasible solution to this problem as it delivers a comprehensive record of the visual system (Nikolaev, Meghanathan, and van Leeuwen 2016). By recording the timings and locations of saccades and fixations, the eye tracker enables the inference of which visual information is being processed at what time and the neuronal response to said information can then be recorded through neuroimaging. Eye tracking has been established as an important source of complementary information for the study of the visual system. It has been used in conjunction with several imaging modalities such as functional magnetic resonance imaging (fMRI) (Jo, Ito, et al. 2019; Agtzidis et al. 2020) electroencephalography (EEG) (Ossandón et al. 2010; Kamienkowski et al. 2012; Kaunitz et al. 2014; Seidkhani et al. 2017; Jo, Kellermann, et al. 2019), and magnetoencephalography (MEG) (Parr et al. 2019).

The electrophysical response following a fixation is called the fixation-related evoked potential (FRP) for EEG and the fixation-related evoked field (FRF) for MEG

[1] The introduction is based on the introduction of (Kiefer et al. 2022).

(Nikolaev, Meghanathan, and van Leeuwen 2016; Ossandón et al. 2010). The FRP has been reported to be a neural marker of natural visual processing, thus enabling the study of neural responses during the natural visual exploration with unrestricted, voluntary eye movements (Nikolaev, Meghanathan, and van Leeuwen 2016; Ossandón et al. 2010). Furthermore, there is evidence that the FRP is affected by both top-down guidance and bottom-up sensory processing as the FRP has been found to reflect the cognitive processes of object identification and object recognition (Kamienkowski et al. 2012; Kaunitz et al. 2014). In a recent study of visual searching, it was also found that it is possible to determine whether subjects were looking at target or non-target objects based on the FRP (Finke et al. 2016).

In order to interact efficiently and effectively with the environment, the brain has to process information selectively according to current goals. Such task-dependent, selective information processing has also been identified during studies of visual processing where attentional selection is generally said to be governed by two types of competing mechanisms: bottom-up and top-down processing (Delorme et al. 2004; Sobel et al. 2007; Theeuwes 2010). Bottom-up processing refers to the case where salient properties of the visual stimuli automatically and involuntarily capture the attention while, during top-down processing, attentional selection is under control of the observer (Sobel et al. 2007). Top-down processes can draw on prior knowledge to guide attention to objects most likely to help accomplish the observer's goals (Sobel et al. 2007).

One example for such task-dependent, selective information processing was that it could be distinguished based on modulations of functional connectivity networks whether participants were tasked to either identify which animals were depicted in video clips or what these animals were doing (Wen et al. 2019). Furthermore, it is thought that goal-directed behavior may lead to additional top-down processes (Chen and Zelinsky 2006). However, how large-scale functional networks are modulated by goal-directed processing during active vision is still not fully understood.

As outlined earlier, the FRP can be used to study naturalistic visual processing and how it is influenced by goal-directed behavior (involving top-down processing). Therefore, the FRP lends itself to studying whole-brain connectivity networks during naturalistic visual tasks. In particular, two recent studies addressed the question of how connectivity networks are affected by bottom-up and top-down processes during visual searching and memorizing tasks as compared to freely viewing natural images through simultaneous EEG and fMRI recordings (Jo, Ito, et al. 2019; Jo, Kellermann, et al. 2019). The authors found that a) the visual ventral stream exhibited different functional structures with task-dependent activations in visual areas V1 and V4; and that b) backward connections in the ventral visual stream were strengthened during searching, while forward connections were strengthened during memorizing. However, with the saccade-fixation cycle being as short as 250 ms (see section 7.3.1), the fast neural processes following fixations cannot be adequately represented using fMRI, and while EEG provides a sufficiently high temporal resolution, it suffers from a relatively poor spatial resolution. Finally, in their causality analysis, they only investigated interactions between a small subset of regions (inferior temporal gyrus, V1, and V4), which exhibited significant

differences in activity between the three tasks. Thus, areas, which were similarly active across all three tasks, were dismissed. However, this decision may have led to the identification of false-positive connections. For a true representation of network dynamics, all relevant areas have to be included in the connectivity network analysis (Geweke 1984; Granger 1980).
These issues can be addressed by employing MEG to record the whole-brain activity. The advantage of MEG is that it has an adequate temporal resolution for capturing the fast visual processes similar to EEG but provides a more accurate spatial resolution and including the entire brain during the analysis should allow for more accurate representations of the network dynamics.

Therefore, whole-brain MEG and eye tracking were combined in this dissertation to investigate natural visual processing of still images (photographs) via the FRF using the same paradigm as employed by (Jo, Ito, et al. 2019; Jo, Kellermann, et al. 2019). The results for three experimental conditions, free viewing (FV), guided visual searching (VS), and memorizing (ME), were analyzed to answer two major research questions: 1) how does the goal-directed behavior during the search task affect the communication in the brain as compared to the free viewing and 2) can the MEG time series recordings be used to decode human behavior on single FRF epochs (memorizing vs. freely viewing)?

Neural fingerprinting, i.e., the differentiation of individuals based on neuroimaging recordings, has become an increasingly popular research topic over the last few years with the emergence of open datasets and improved analytical tools (da Silva Castanheira et al. 2021b). While the ongoing activity at rest has long been considered as brain noise (Başar 1990; Stein, Gossen, and Jones 2005; Uddin 2020; da Silva Castanheira et al. 2021b), it is becoming increasingly clear that this "noise" carries complex information that is specific to the individual. For example, it was possible to identify individuals in a cohort based on recordings from various imaging modalities such as structural MRI (Valizadeh et al. 2018; Wachinger et al. 2015), fMRI (Amico and Goñi 2018; Bari et al. 2019; Finn et al. 2015; Kaufmann et al. 2017; Miranda-Dominguez et al. 2014), functional near-infrared spectroscopy (de Souza Rodrigues et al. 2019), EEG (Fraschini et al. 2015; Kong et al. 2019; Rocca et al. 2014), and MEG (Sareen et al. 2021; da Silva Castanheira et al. 2021a, 2021b). Furthermore, it was demonstrated that this data could also be used to predict individual traits such as attention abilities, working memory, or intelligence (Finn et al. 2015; A. S. Greene et al. 2018; Yamashita et al. 2018; Yoo et al. 2018; Rosenberg et al. 2020). In an experiment with monozygotic twins, it was shown that the counterpart to an individual could be identified with high accuracies suggesting that there is a strong genetic component to the activity patterns (Demuru et al. 2017). The ability to make inferences at the individual level and to map individual traits to behavior and cognition might even open up avenues for personalized medicine and psychiatry (Waller et al. 2017).

However, with few exceptions, these classification methods relied for their features on second order statistical measures such as functional connectomes or power spectral densities on which their classification algorithms were built (da Silva Castanheira et al. 2021b), which leads to additional layers of complexity. This leads

to the third major research question: 3) is it possible to identify individuals based directly on single-epoch time series of MEG resting-state recordings?

The dissertation is structured as follows:

Chapter 2 provides the most basic information required to understand which processes in the brain generate the tiny but measurable magnetic induction outside of the head and which instrumentation is required to detect these signals with sufficient sensitivity. It also discusses methods for the projection of the signals measured outside the head to the brain, a process referred to as source localization. In particular, minimum-norm estimates (MNE) and dynamic statistical parametric mapping (dSPM) are illustrated (Hämäläinen and Ilmoniemi 1994; Dale et al. 2000). Brain signals were reconstructed with dSPM in this dissertation.

Chapter 3 describes spatiotemporal cluster permutation testing (Maris and Oostenveld 2007), a method which was used in this dissertation to identify regions in the brain with significant activity in response to fixation onset.

Chapter 4 covers the concepts of Granger causality for identifying directed interactions between simultaneously recorded time series (Granger 1969). Generalized partial directed coherence (GPDC), an advanced methods for the estimation of directed interactions in the frequency domain for the multivariate case, is presented (Baccalá, Sameshima, and Takahashi 2007).

Chapter 5 addresses machine learning applications for time series classification. RandOm Convolutional KErnel Transformation (ROCKET) is introduced as a state-of-the-art method for multivariate time series classification (Dempster, Petitjean, and Webb 2020).

Chapter 6 describes the experimental setup. The stimuli and task protocol with free viewing, guided visual searching, and memorization tasks were similar to what was used in previous studies (Jo, Ito, et al. 2019; Jo, Kellermann, et al. 2019). The data was acquired using MEG, eye tracking, and MRI. 31 participants were included in the analysis.

The final three chapters before the general discussion present original research. Chapter 7 discusses the analysis of behavioral data. This includes the task performance during the guided visual search and memorization tasks and statistics about the eye movements such as fixation duration or saccade direction.

Chapter 8 explores the first major research question of how cognitive tasks shape the visual processing in the human brain. Specifically, it was investigated how the goal-directed behavior during a guided visual search influences the networks in the brain as compared to freely viewing naturalistic images. SCPT was used to identify regions in the brain with significant fixation-related evoked activity (FRA)[2] during the two tasks and directed interactions between these regions were uncovered using GPDC.

[2] The source-localized activity based on the FRF.

Chapter 9 illustrates how ROCKET can be used to classify single-epoch time series with respect to the second and third major research questions. First, activity from single fixations was classified based on whether the fixations were performed during the free viewing or the memorization task. Second, resting-state data was used for neural fingerprinting, i.e., subjects could be differentiated based on their neural activity during rest.

Chapter 10 concludes the dissertation with a general discussion and an outlook for future development.

2 THE BASICS OF MAGNETOENCEPHALOGRAPHY

Changes in ion concentrations between intra- and extracellular compartments drive many processes in the living human body. As per Ampère's law, the resulting electric currents produce magnetic induction whose strength can be measured from the outside of the body. This dissertation focuses on MEG, which is a noninvasive method for the remote detection of changes in the extremely weak magnetic induction produced by neuronal activity from the outside of the head (Cohen 1968). It is known for its exceptional time resolution of under 1 ms and a moderate spatial resolution of 2-3 mm for sources in the cerebral cortex under favorable conditions (Hämäläinen et al. 1993).

This chapter will provide the reader with the most basic information to understand which processes in the brain are responsible for the measurable magnetic induction outside of the head and the instrumentation that provides the necessary sensitivity for detection will be illustrated. Finally, the basics of source localization—how the signals measured outside of the head can be projected onto the brain—are outlined.

2.1 THE HUMAN BRAIN[3]

The human brain consists of three main anatomic regions: the brainstem, the cerebellum, and the cerebrum (Figure 1). The cerebrum is the largest part of the brain. It sits on top of the brain stem and the cerebellum. The longitudinal fissure separates the cerebrum into two hemispheres while the Rolandic fissure and the Sylvian fissure further divide each hemisphere into four lobes: frontal, parietal, temporal, and occipital lobe. The cerebrum's outmost layer is a 2–4 mm thick sheet of gray tissue called the cerebral cortex under which the cerebrum consists mostly of white matter—nerve fibers linking different cortical areas with one another and also connecting the cortex to other brain structures.

The human brain is a highly complex, organized structure. With a total surface area of about 2500 cm^2, a complicated way of folding is necessary for the cortex to fit into the cranial cavity. The resulting folds and ridges are called sulci and gyri, respectively. There are at least 10^{10} neurons, electrically excitable cells, in the cerebral cortex (Rutecki 1992; Hämäläinen et al. 1993). They are connected through a network of 10^{14} interconnections also known as synapses through which information is passed.
Different regions of the cortex are associated with different functions. For example, the primary somatosensory cortex, S1, processes tactile stimuli from the skin. S1 lies posterior to the Rolandic fissure while M1, the primary motor cortex, is situated anterior to the Rolandic fissure. The primary visual cortex is located at the back of the head in the occipital cortex.

[3] Unless stated otherwise, the information in this section was taken from the highly informative paper by Matti Hämäläinen and colleagues on the basics of magnetoencephalography (Hämäläinen et al. 1993).

Various functions have been associated with the cerebellum such as motor coordination, motor learning, sensory-motor integration and timing (Ohyama et al. 2003) while the brainstem is said to be responsible for basic vital functions such as heartbeat blood pressure, breathing, sleep, and the control of consciousness (Ángeles Fernández-Gil et al. 2010). Furthermore, the brainstem connects the cerebrum to the spinal cord (Ángeles Fernández-Gil et al. 2010).

When the brain processes information, small currents flow in the neural network. The currents then induce tiny magnet fields. If enough neurons fire at the same time and the current directions are aligned, changes in these magnetic fields can be measured noninvasively from outside the skull using superconducting quantum interference device (SQUID) magnetometers. This effect is known as magnetoencephalography (MEG).
There is a complementary effect called electroencephalography (EEG) where electric potential differences generated by the same synchronous neuronal activity in the brain can be measured using electrodes placed on the scalp.

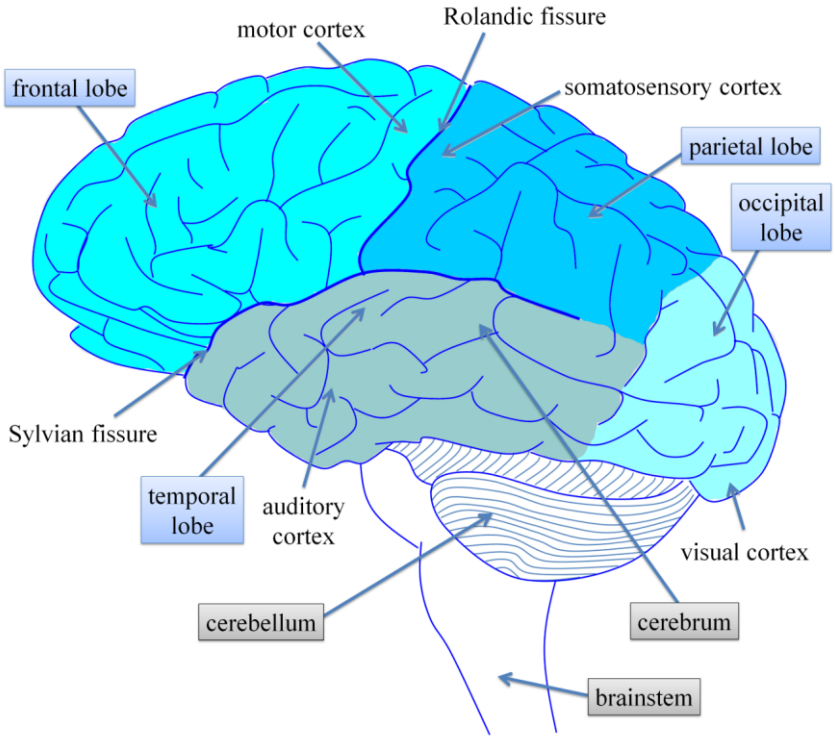

Figure 1: Illustration of the anatomy of the human brain as seen from the left side. Figure reprinted from (Breuer 2016). Copyright 2016 by Lukas Breuer.

2.2 NEURONAL ACTIVITY[4]

A neuron is made up of the cell body (soma) containing the nucleus, the cell protrusions called dendrites, and the axon, which is a single, long extremity leading away from the soma. The neurons in the cortex can be divided into two groups: stellate cells and pyramidal cells. For stellate cells, the dendrites extend radially

[4] Unless stated otherwise, the information in this section was taken from the highly informative paper by Matti Hämäläinen and colleagues on the basics of magnetoencephalography (Hämäläinen et al. 1993).

from the soma and for pyramidal cells, the dendrites are oriented parallel to each other and perpendicular to the cortical surface.
Like other cells, there is an insulating membrane surrounding the neuron. Different ion concentrations within the cell and the surrounding tissue can be maintained through so-called ion pumps—protein molecules, which can transport ions across the membrane against the concentration gradient. For example, the NA-K pump exchanges three Na^+ from within the neuron with two K^+ ions from the extracellular surroundings. A neuron in its resting state has a membrane potential of about –70 mV and deviations from this potential drive neuronal activity. Input from neighboring neurons via thousands of synapses can influence the membrane potential. Excitatory synapses, which increase the membrane potential, are typically found at the dendrites while inhibitory synapses, which decrease the membrane potential, tend to be located at the soma. There are two types of neuronal activity, the postsynaptic potential and the action potential.

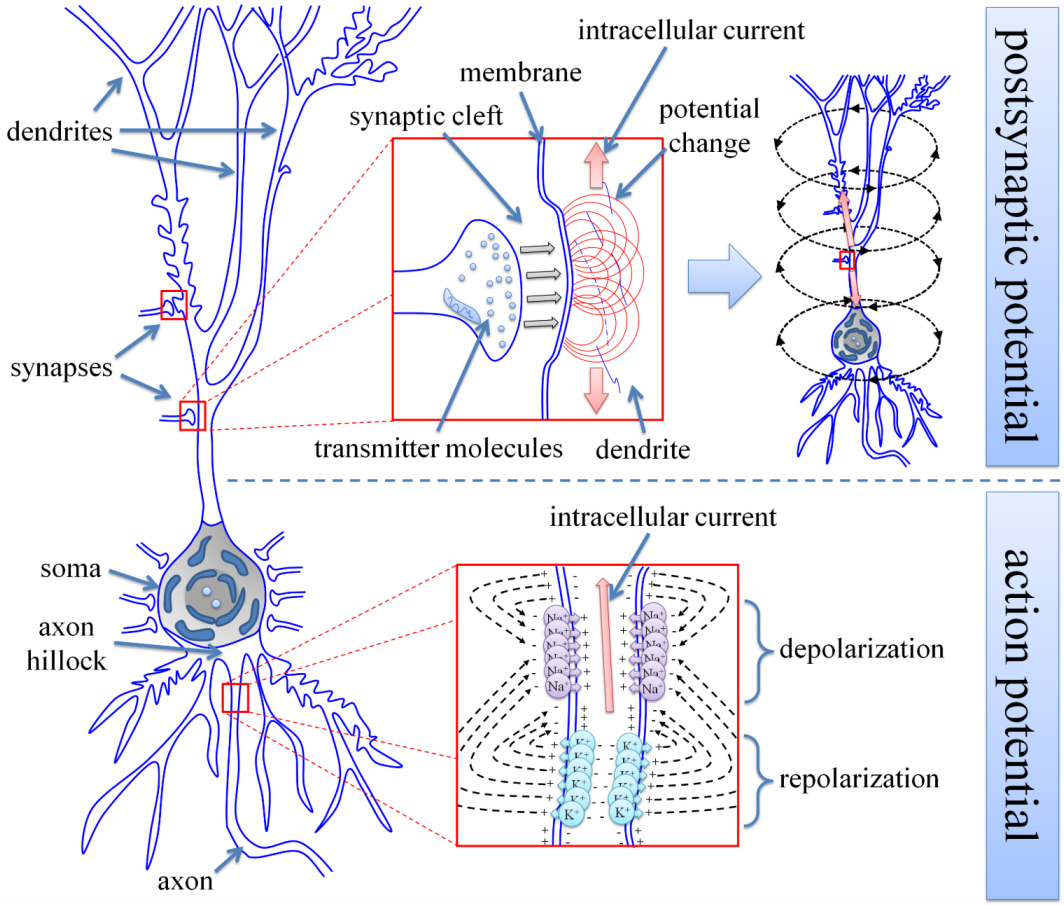

Figure 2: A pyramidal neuron with illustrations of the postsynaptic potential and the action potential. Intracellular currents are indicated by red arrows while black dashed lines show the magnetic fields associated with the potentials. Figure reprinted from (Breuer 2016). Copyright 2016 by Lukas Breuer.

The postsynaptic potential:

The synapses can release neurotransmitter molecules to the synaptic cleft. When these molecules arrive at the postsynaptic cell, the transmissibility of its membrane changes for certain ions. If sodium channels open up, the resulting current flows into the cell while the current flows out of the cell if potassium or chloride channels open up. This current can then flow along the interior of the postsynaptic cell with the strength of the current source decreasing with the distance from the synapse.

Due to the influx of ions, the potential across the membrane changes. The amplitude of the postsynaptic potential is of the order of +10 mV compared to the baseline level lasting for several tens to hundreds of milliseconds.

The action potential:
If a stimulus causes the intracellular potential at the axon hillock to surpass the threshold of approximately –40 mV, the neuron fires an action potential. At the hillock and along the axon, there are voltage-gated sodium channels, which open when the membrane depolarizes. The influx of sodium ions causes further depolarization along the axon membrane with more sodium channels opening. This wave of depolarization propagates from the axon hillock towards the dendrites at the axon's end. From there, the stimulus is transmitted to the next cells via the synapses. Repolarization begins when the intracellular potential reaches about +20 mV and voltage-gated potassium channels open. The outflow of potassium ions out of the cell causes the potential to decrease again to pre-firing levels. Typically, the action potential has a duration of approximately a millisecond, and it reaches an amplitude of +100 mV compared to the resting potential.

There are two reasons why the postsynaptic potential in pyramidal cells (with parallel dendrites) is most likely to produce a signal detectable with MEG. First, thousands of simultaneously active neurons are necessary to result in a current large enough to generate measurable magnetic induction and, without the need for rigorous synchronization, the duration of the currents is sufficiently long for an effective summation. Furthermore, the currents should be oriented in the same direction to avoid signal cancellation. Second, the field of an action potential decays faster with distance as compared to the field of a postsynaptic potential. The action potential can be described by two oppositely oriented currents forming a current quadrupole whose field decays with distance $1/r^4$ while the currents from postsynaptic potentials can be approximated by current dipoles whose fields decay with distance $1/r^3$ where r is the distance from the source.

2.3 Environmental, instrumental, and biomagnetic noise[5]

The magnetic noise level in a laboratory is usually magnitudes higher than the neuromagnetic field responses generated in the human brain (Figure 3). Environmental noise sources may include power lines, electric motors, elevators, moving cars or trains whose influence can be reduced by magnetically shielding the recording room. The shielding often consists of high permeability μ-metal, a ferromagnetic nickel-iron alloy, and sheets of copper and aluminum for reducing low and high frequency noise, respectively.
In contrast to these environmental noise sources, biomagnetic noise cannot be reduced through magnetic shielding as it originates from the subject's body inside the recording room. The biological processes generating the strongest magnetic

[5] Unless stated otherwise, the information in this section was taken from the highly informative paper by Matti Hämäläinen and colleagues on the basics of magnetoencephalography (Hämäläinen et al. 1993).

fields are the contraction of the heart and activation of the skeletal muscles. Furthermore, eye movements and eye blinks can contaminate the recordings due to the eyes' close vicinity to the detection coils. Ocular and cardiac artifacts can be removed in a common data preprocessing step using independent component analysis (ICA).
The largest field intensity from the normal awake brain is due to spontaneous activity, e.g., the α-rhythm can have an amplitude of 1–2 pT. Greater amplitudes are usually the result of abnormal conditions such as spikes during epileptic seizures. Often it is not spontaneous activity that is of interest but the brain's response to sensory stimulation whose amplitudes are of the order of several tens or hundreds of femtotesla. The background activity, i.e., the brain activity that occurs during the stimulation but is not directly related to the stimulus itself, is another factor limiting the signal-to-noise ratio (SNR).

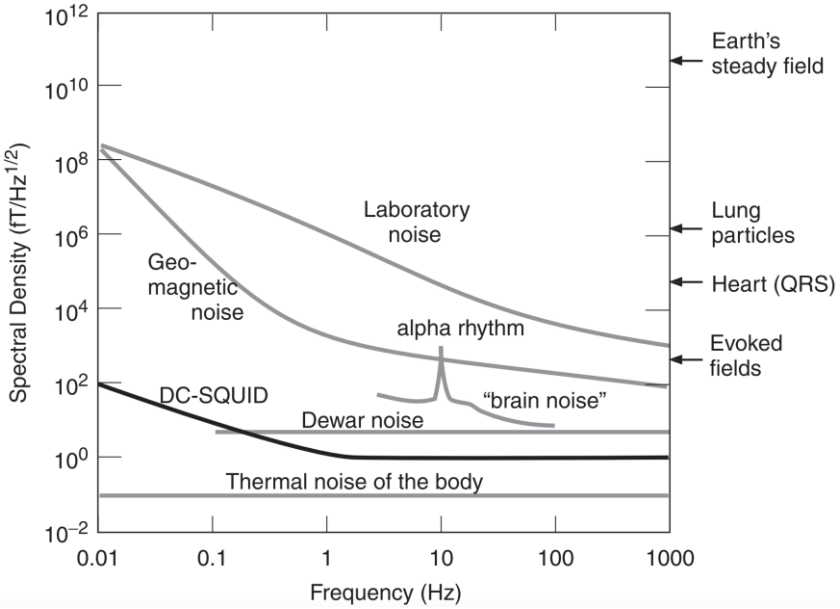

Figure 3: Magnetic field strengths of various environmental and biological (noise) sources. Figure reprinted from (Parkkonen 2010). Copyright 2010 by Oxford Publishing Limited.

2.4 SUPERCONDUCTING QUANTUM INTERFERENCE DEVICES

Due to the extremely small neural currents measured on a scale of nanoampere (10^{-9} A), the magnetic inductions measured outside of the head are typically of the order of femtotesla (10^{-15} T) (Baillet 2017). There are only a few detectors capable of detecting these tiny fields, one of which is the superconducting quantum interference device (SQUID).

To achieve the high sensitivity, SQUIDs combine the physical phenomena of flux quantization and Josephson tunneling (Weinstock 1996). Flux quantization describes the phenomenon where, in a closed superconducting loop, the magnetic flux is quantized in units of the flux quantum $\Phi_0 = h/2e = 2.068e^{-15}$ Wb (Deaver and Fairbank 1961; Doll and Näbauer 1961). So, if an external magnetic flux is applied to the superconducting loop, a screening current starts flowing through the ring, which either increases or decreases the magnetic flux to the closest integral multiple of the flux quantum. Josephson predicted in 1962 that Cooper pairs can tunnel

across thin insulating sections (so-called Josephson junctions) from one superconductor to another without a drop in voltage as long as the current is smaller than the critical current, I_c, of the Josephson junction (Josephson 1962). This effect is called Josephson tunneling.

There are two main types of SQUID, the direct current (dc) SQUID developed in 1964 (Jaklevic et al. 1964) and the radio frequency (rf) SQUID developed in 1965 (Zimmerman, Thiene, and Harding 1970). Both are made up of a superconducting ring which is, in the case of the rf SQUID, interrupted by one and, in the case of the dc SQUID, interrupted by two Josephson junctions. Due to the higher sensitivity, nowadays dc SQUIDs are used in most applications (Fagaly 2006). This is also the case for the MEG system at Forschungszentrum Jülich and, therefore, only the dc SQUID will be described in more detail.

Figure 4 depicts the schematics of a dc SQUID. A constant bias current, I_{bias}, is applied to the superconducting ring so that the two Josephson junctions are wired in parallel and, for identical Josephson junctions, one half of the bias current, $I_B = I_{bias}/2$, flows through each half of the loop (Fagaly 2006). The bias current is chosen in such a way that the current I_B through one of the junctions puts the point of operation halfway between superconducting and resistive behavior on the *I-V* curve (left side of Figure 5) (Fagaly 2006). To avoid hysteretic behavior in the *I-V* curve, shunt resistors are used (Tesche and Clarke 1977; Fagaly 2006).

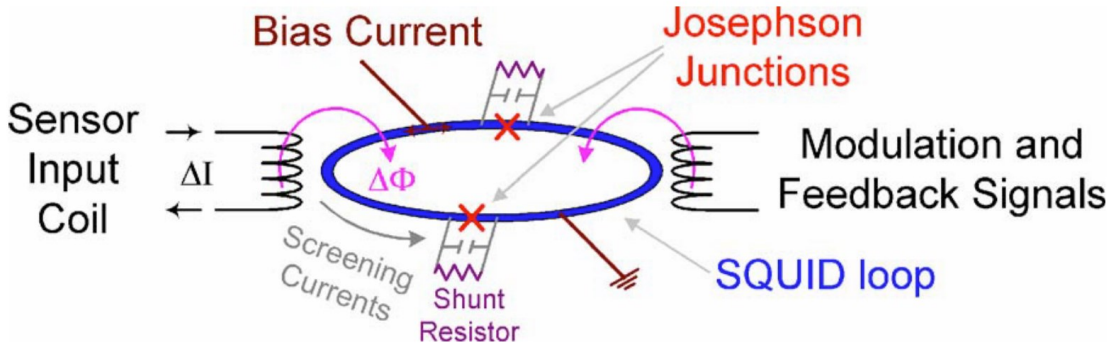

Figure 4: Schematics of a dc SQUID with two Josephson junctions. The self-capacitance of the junctions is represented by the capacitors. Figure reprinted from (Fagaly 2006). Copyright 2006 by American Institute of Physics.

Through inductive coupling, a sensor input (SI) coil and a modulation and feedback signal (MFS) coil are connected to the superconducting loop (Fagaly 2006). Therefore, current changes at the SI coil result in a changing magnetic flux, Φ, through the superconducting loop (Fagaly 2006). Due to flux quantization, a screening current, I_{screen}, starts flowing through the ring (Fagaly 2006). In one half of the ring, the screening current enhances the total current through the junction ($I = I_B + I_{screen} > I_c$) while in the other half, the total current through the junction is reduced ($I = I_B - I_{screen} < I_c$) (Fagaly 2006). The voltage that drops off across the junctions changes periodically with the external magnetic flux and with the period being the flux quantum (right side of Figure 5) (Fagaly 2006).

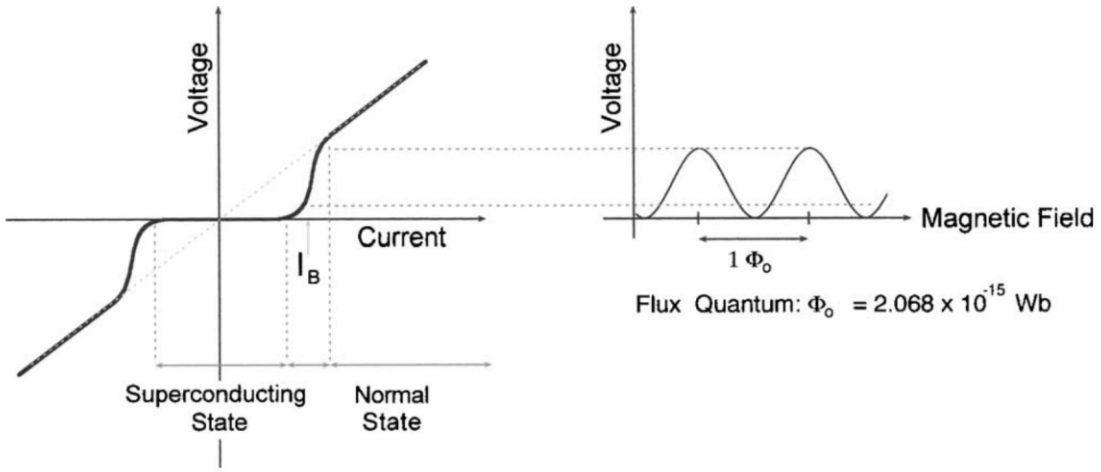

Figure 5: Left: *I-V* curve for the bias point of a single Josephson junction. Right: Voltage versus externally applied magnetic flux at a constant bias current. Figure reprinted from (Fagaly 2006). Copyright 2006 by American Institute of Physics.

Based on the drop in voltage, external feedback can be applied through the MFS coil to counteract the changes in the screening current and to lock the SQUID to a unique point in the Φ-*V* curve (Fagaly 2006). Due to the sinusoidal behavior, SQUIDs are usually operated at the point where the change in voltage is linear in the change in magnetic flux, i.e., at the steepest point of the Φ-*V* curve where the derivative $\partial V/\partial \Phi$ is at its maximum (Fagaly 2006). Thus, the feedback current becomes a direct measure of the changes in external flux applied to the SQUID (Fagaly 2006).

2.5 PICK-UP COIL CONFIGURATIONS[6]

Since the diameters of SQUIDs are typically very small, often less than 1 mm, high magnetic flux densities would be necessary to produce measurable signals. However, as alluded to in the previous section, it is possible to inductively couple signal input to the SQUID. This can be achieved using flux transformers, which come in various configurations. The choice of configuration can have a profound effect on the detected signal. Flux transformers usually consist of one or more pick-up coils, optional compensation coils, and a signal coil on top of the SQUID. With the typical pick-up coil diameter ranging from one to two centimeters it is possible to collect magnetic flux from a larger area and channel it through the SQUID. However, there is a tradeoff between sensitivity and spatial resolution when choosing an appropriate size of the pick-up coil.

The simplest configuration, called a magnetometer (Figure 6a), consists of a single pick-up coil without any compensation coils. It measures B_z, the component of the magnetic flux in the *z*-direction. A first-order axial gradiometer can be constructed by connecting two coaxial coils in series with the upper compensation coil wound oppositely to the lower pickup coil (Figure 6c). Thus, the first-order axial gradiometer measures the derivative $\partial B_z/\partial z$ of the magnetic flux in the *z*-direction. If there is homogeneous flux through both coils, the generated voltage is effectively cancelled out. Since the amplitude of magnetic fields generated by a dipole

[6] Unless stated otherwise, the information in this section was taken from (Parkkonen 2010).

decreases quickly with $1/r^3$, (Fagaly 2006), signal detection of sources close to the pickup coil is relatively unaffected by the attenuation through the compensation coil. However, for distant (noise) sources, the magnetic field is comparatively homogenous leading to signal cancellation (Fagaly 2006; Parkkonen 2010). As a rule of thumb, an adequate distance between pick-up and compensation coil is one to two times the distance from the pick-up coil to the source (Vrba et al. 1982; Duret and Karp 1983; Hämäläinen et al. 1993; Breuer 2016).

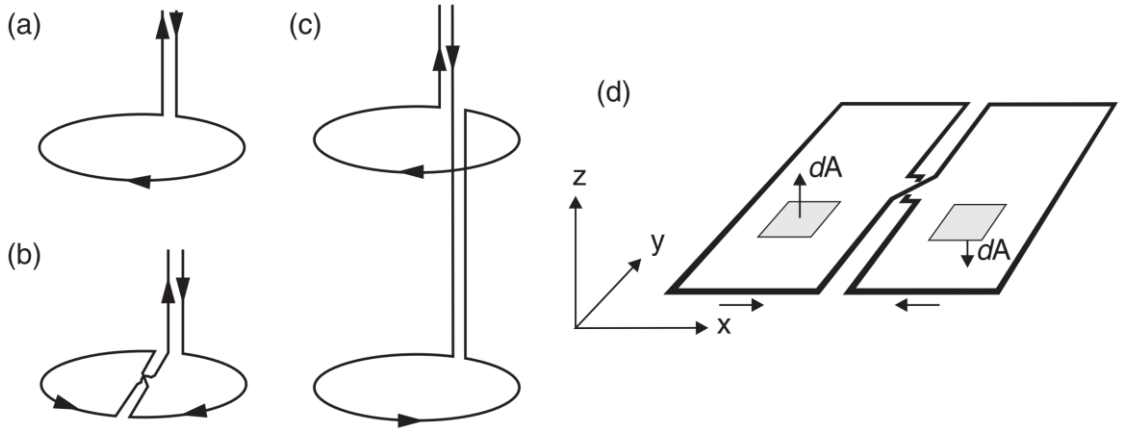

Figure 6: Flux transformer configurations: a) magnetometer, b) planar gradiometer, c) axial gradiometer, d) integration of magnetic flux through a planar gradiometer measuring $\partial B_z/\partial x$. Figure reprinted from (Parkkonen 2010). Copyright 2010 by Oxford Publishing Limited.

Instead of placing two coils on top of one another, a first-order planar gradiometer can be constructed by placing two oppositely wound coils on the same plane for noise compensation in the x- or y-direction, i.e., the derivative $\partial B_z/\partial x$ or $\partial B_z/\partial y$ of the magnetic field is being measured. A common configuration is the so-called double-D arrangement (Figure 6b, d). One advantage over axial gradiometers is that the arrangement is more compact in size. Additionally, off-diagonal gradiometers offer a narrower and shallower spatial sensitivity pattern (Hämäläinen et al. 1993). Thus, it is possible to measure signals more accurately with less overlapping signals from neighboring regions (Hämäläinen et al. 1993).

Compared to the gradiometer configurations, the simple magnetometer necessitates a low-noise environment during the recordings (Fagaly 2006). However, due to the lack of signal cancellation, magnetometers also provide the best sensitivity for deep sources.

2.6 Source localization of MEG signals

A common step in MEG analysis is source localization where one attempts to reconstruct the combination of current sources in the brain, which gave rise to the observed signal at the SQUID sensors (Hämäläinen et al. 1993; Jensen and Hesse 2010). This is also known as the inverse problem (Hämäläinen et al. 1993).
However, when only the magnetic field outside of a conductor is known, the current distribution inside the conductor cannot be determined uniquely as shown by Helmholtz in 1853 (Helmholtz 1853). If there are multiple sources active at the same time, the resulting field is a superposition of the contributing components (superposition principle), and an infinite number of current distributions can be

found that all result in the same magnetic induction field outside of the head (Hämäläinen et al. 1993). Furthermore, there are certain finite conductor geometries where the fields generated by the primary current and the volume current cancel each other out so that the external field becomes zero (Hämäläinen et al. 1993). Another complication is that there are various noise sources that contaminate the recorded brain signals such as environmental noise or muscular activity (especially cardiac and ocular activity) (Hämäläinen et al. 1993).
Even though there is no unique solution to the inverse problem, there is a series of different approaches to tackle this problem: dipole methods (Mosher, Lewis, and Leahy 1992), distributed source analysis like minimum norm estimates (Dale et al. 2000; Hämäläinen and Ilmoniemi 1994; Pascual-Marqui 2002), spatial filters like beamforming methods (Gross et al. 2001; Van Veen et al. 1997), and more. All these methods make various, different assumptions in their attempt to limit the space of possible solutions but in the end they all have to adhere to same basic principles of electromagnetism, which will be elucidated below.

2.6.1 AN INTRODUCTION TO ELECTROMAGNETISM

In 1865, James Clerk Maxwell published in his seminal paper "A Dynamical Theory of the Electromagnetic Field" a set of equations, which describe the connection between electric and magnetic fields, electric charge and electric currents (Maxwell 1865). Maxwell's equations have since then been condensed into a commonly used set of four equations (Heaviside 1892):

$$\begin{aligned} \nabla \cdot \boldsymbol{E} &= \frac{\rho}{\varepsilon_0} \\ \nabla \times \boldsymbol{E} &= -\frac{\partial \boldsymbol{B}}{\partial t} \\ \nabla \cdot \boldsymbol{B} &= 0 \\ \nabla \times \boldsymbol{B} &= \mu_0 \boldsymbol{J} + \mu_0 \varepsilon_0 \frac{\partial \boldsymbol{E}}{\partial t}. \end{aligned} \tag{2.1}$$

ρ, ε_0, and μ_0 describe the charge density, the permittivity, and the permeability, respectively. The current density, electric field, and magnetic induction are denoted by $\boldsymbol{J}$, $\boldsymbol{E}$, and $\boldsymbol{B}$, respectively. Since the temporal dynamics of $\boldsymbol{J}$, $\boldsymbol{E}$, and $\boldsymbol{B}$ are relatively slow (below 1 kHz) the simplified quasi-static approximation of Maxwell's equations can be used (Hämäläinen and Hari 2002; Lopes Da Silva 2010):

$$\begin{aligned} \nabla \cdot \boldsymbol{E} &= \rho/\varepsilon_0 \\ \nabla \times \boldsymbol{E} &= 0 \\ \nabla \cdot \boldsymbol{B} &= 0 \\ \nabla \times \boldsymbol{B} &= \mu_0 \boldsymbol{J} \end{aligned} \tag{2.2}$$

The first equation states that electric charges are the sources of the electric field $\boldsymbol{E}$ while the fourth equation states that electric currents produce the magnetic induction $\boldsymbol{B}$. The current density produced by neuronal activity can be split into the primary current and the volume current (Hämäläinen et al. 1993):

$$\boldsymbol{J}(\boldsymbol{r}) = \boldsymbol{J}^p(\boldsymbol{r}) + \boldsymbol{J}^V(\boldsymbol{r}). \tag{2.3}$$

The primary current is a result of neural activity and flows mainly inside or in the vicinity of a neuron (Hämäläinen et al. 1993). The volume current flows passively in the surrounding tissue and completes the loop of ionic flow avoiding a buildup of charge (Hämäläinen et al. 1993; Breuer 2016). Both the primary and the volume current are responsible for the generation of the magnetic induction (Hämäläinen et al. 1993).

$$\boldsymbol{J}(\boldsymbol{r}) = \boldsymbol{J}^p(\boldsymbol{r}) + \sigma(\boldsymbol{r})\boldsymbol{E}(\boldsymbol{r}) = \boldsymbol{J}^p(\boldsymbol{r}) - \sigma(\boldsymbol{r})\nabla V(\boldsymbol{r}) \tag{2.4}$$

with σ being the macroscopic conductivity and V($\boldsymbol{r}$) being a scalar potential (Hämäläinen and Ilmoniemi 1994). By locating the primary current, the source of brain activity can be determined (Hämäläinen et al. 1993). As mentioned earlier in section 2.2, the primary currents measurable with MEG are the postsynaptic currents generated in the pyramidal cells.

2.6.2 THE FORWARD PROBLEM[7]

Given a primary current density $\boldsymbol{J}^p$ inside the brain it is straightforward to calculate the external magnetic induction field $\boldsymbol{B}$ outside of the head. This is called the forward problem. It is possible to find solutions to the aforementioned *inverse problem* by solving the forward problem for a given primary current density and comparing the results with the observed data. If the current density explains the measured data well, one potential solution has been found.
Ampère-Laplace's Law states that the magnetic induction field $\boldsymbol{B}$ at a given location $\boldsymbol{r}$ resulting from a current $\boldsymbol{J}$ at position $\boldsymbol{r}'$ is given by:

$$\boldsymbol{B}(\boldsymbol{r}) = \frac{\mu_0}{4\pi}\int \boldsymbol{J}(\boldsymbol{r}') \times \frac{(\boldsymbol{r}-\boldsymbol{r}')}{\|\boldsymbol{r}-\boldsymbol{r}'\|^3} d^3\boldsymbol{r}' \tag{2.5}$$

where $\|.\|$ denotes the Euclidean norm. By utilizing the identity $(\boldsymbol{r}-\boldsymbol{r}')/\|\boldsymbol{r}-\boldsymbol{r}'\|^3 = -\nabla(1/\|\boldsymbol{r}-\boldsymbol{r}'\|) = \nabla'^{(1/\|r-r'\|)}$ with $\nabla = \frac{\partial}{\partial x}\boldsymbol{e}_x + \frac{\partial}{\partial y}\boldsymbol{e}_y + \frac{\partial}{\partial z}\boldsymbol{e}_z$ and $\nabla' = \frac{\partial}{\partial x'}\boldsymbol{e}_{x'} + \frac{\partial}{\partial y'}\boldsymbol{e}_{y'} + \frac{\partial}{\partial z'}\boldsymbol{e}_{z'}$, equation (2.5) can be rewritten as:

$$\boldsymbol{B}(\boldsymbol{r}) = \frac{\mu_0}{4\pi}\int \boldsymbol{J}(\boldsymbol{r}') \times \nabla' \frac{1}{\|\boldsymbol{r}-\boldsymbol{r}'\|} d^3\boldsymbol{r}'. \tag{2.6}$$

In the next step, the identity $\boldsymbol{J}(\boldsymbol{r}') \times \nabla'(1/\|\boldsymbol{r}-\boldsymbol{r}'\|) = \big(\nabla' \times \boldsymbol{J}(\boldsymbol{r}')\big)/\|\boldsymbol{r}-\boldsymbol{r}'\| - \nabla' \times (\boldsymbol{J}(\boldsymbol{r}')/\|\boldsymbol{r}-\boldsymbol{r}'\|)$ and the assumption that $\boldsymbol{J}(\boldsymbol{r}')/\|\boldsymbol{r}-\boldsymbol{r}'\|$ vanishes on an infinitely distant surface are used to arrive at:

$$\boldsymbol{B}(\boldsymbol{r}) = \frac{\mu_0}{4\pi}\int \big(\nabla' \times \boldsymbol{J}(\boldsymbol{r}')\big) \frac{1}{\|\boldsymbol{r}-\boldsymbol{r}'\|} d^3\boldsymbol{r}'. \tag{2.7}$$

Finally, the magnetic induction field can be separated into contributions from the primary current and the volume current using equation (2.4):

[7] Unless stated otherwise, the information in this section was taken from the highly informative paper by Matti Hämäläinen and colleagues on the basics of magnetoencephalography (Hämäläinen et al. 1993).

$$\boldsymbol{B}(\boldsymbol{r}) = \frac{\mu_0}{4\pi}\int \nabla' \times \left(\boldsymbol{J}^p(\boldsymbol{r}') - \sigma(\boldsymbol{r}')\nabla' V(\boldsymbol{r}')\right)\frac{1}{\|\boldsymbol{r}-\boldsymbol{r}'\|}\,d^3\boldsymbol{r}'. \tag{2.8}$$

By using the identity $\nabla \times (\sigma\nabla V) = \nabla\sigma \times \nabla V = -\nabla \times (V\nabla\sigma)$ and performing the reverse of the transformations from equation (2.5) to equation (2.7), the following equation is obtained:

$$\begin{aligned}\boldsymbol{B}(\boldsymbol{r}) &= \frac{\mu_0}{4\pi}\int \nabla' \times \left(\boldsymbol{J}^p(\boldsymbol{r}') + V(\boldsymbol{r}')\nabla'\sigma(\boldsymbol{r}')\right)\frac{1}{\|\boldsymbol{r}-\boldsymbol{r}'\|}\,d^3\boldsymbol{r}' \\ &= \frac{\mu_0}{4\pi}\int \left(\boldsymbol{J}^p(\boldsymbol{r}') + V(\boldsymbol{r}')\nabla'\sigma(\boldsymbol{r}')\right) \times \frac{\boldsymbol{r}-\boldsymbol{r}'}{\|\boldsymbol{r}-\boldsymbol{r}'\|^3}\,d^3\boldsymbol{r}'.\end{aligned} \tag{2.9}$$

From Maxwell's equations in the quasi-static approximation ($\mu_0\boldsymbol{J} = \nabla \times \boldsymbol{B}$) and the fact that the divergence of a curl vanishes follows that $\nabla \cdot \boldsymbol{J} = 0$. Therefore, taking the divergence of equation (2.4) results in:

$$\nabla \cdot (\sigma\nabla V) = \nabla \cdot \boldsymbol{J}^p. \tag{2.10}$$

In regions with constant σ, this reduces to Poisson's equation $\Delta V = \nabla \cdot \boldsymbol{J}^p/\sigma$, which can be solved for V with proper boundary conditions (Sarvas 1987; Hämäläinen et al. 1993). At this point the only unknown needed for the computation of $\boldsymbol{B}$ and V is the conductivity σ, which depends on the geometry and the properties of the conducting medium. Usually, heavy numerical computations are required to solve equation (2.10). However, in certain conductor geometries it is possible to exploit symmetries such that an analytical solution can be found (Sarvas 1987). The spherically symmetric conductor is one such example (Sarvas 1987).

2.6.3 Spherically symmetric conductor

In the field of MEG, the head is typically divided into five different regions: gray and white matter, cerebrospinal fluid, the skull, and the scalp (Hämäläinen et al. 1993). Different models with different shapes for these areas exist. There are some variations that assume simplified forms such as concentric spheres (Sarvas 1987) or prolate and obloid spheroids (Cuffin and Cohen 1977). But there are also realistic approaches such as boundary element models (Bommel, Rockelein, and Urankar 1993; Cuffin 1990, 1995) or finite element models (Clerc, Dervieux, and Faugeras 2002; Wolters, Grasedyck, and Hackbusch 2004), which use the subject's head geometries obtained from anatomic images.
In this dissertation, the source space analysis was performed using the MNE python software package (Gramfort et al. 2014), which uses a linear collocation boundary element model (Mosher, Leahy, and Lewis 1999) with the isolated skull approach (Hämäläinen and Sarvas 1989) to solve the forward problem. However, only the steps involved in solving the forward problem for the simplest case of a uniform spherically symmetric conductor (Ilmoniemi, Hämäläinen, and Knuutila 1985) will be illustrated here.

It can be shown that the contribution of volume currents to the radial field component vanishes in the case of a uniform spherically symmetric conductor (Sarvas 1987; Hämäläinen et al. 1993). Equation (2.5) then reduces to (Sarvas 1987; Hämäläinen et al. 1993):

$$B_r = \boldsymbol{B}(\boldsymbol{r}) \cdot \boldsymbol{e}_r = \frac{\mu_0}{4\pi} \int \boldsymbol{J}^p(\boldsymbol{r}') \times \frac{\boldsymbol{r} - \boldsymbol{r}'}{\|\boldsymbol{r} - \boldsymbol{r}'\|^3} \cdot \boldsymbol{e}_r d^3\boldsymbol{r}', \tag{2.11}$$

where $\boldsymbol{e}_r = \boldsymbol{r}/|\boldsymbol{r}|$. Assuming further that the neural activity is restricted to a small area, the equivalent current dipole model can be used to explain the measured magnetic induction field. The current dipole $\boldsymbol{Q}$ at $\boldsymbol{r}_Q$ can be thought of as the entire current $\boldsymbol{J}^p(\boldsymbol{r})$ concentrated into a single infinitesimal point (Hämäläinen et al. 1993):

$$\boldsymbol{J}^p(\boldsymbol{r}) = \boldsymbol{Q}\delta(\boldsymbol{r} - \boldsymbol{r}_Q), \tag{2.12}$$

where δ is the Dirac delta function. By inserting equation (2.12) into equation (2.11), a simple equation for the estimation of the magnetic induction field of $\boldsymbol{Q}$ can be obtained (Sarvas 1987; Hämäläinen et al. 1993):

$$B_r(\boldsymbol{r}) = -\frac{\mu_0}{4\pi} \frac{\boldsymbol{Q} \times \boldsymbol{r}_Q \cdot \boldsymbol{e}_r}{\|\boldsymbol{r} - \boldsymbol{r}_Q\|^3}. \tag{2.13}$$

Additionally, since the total current density $\boldsymbol{J}$ is zero outside the conductor, it follows that $\nabla \times \boldsymbol{B} = 0$ (Hämäläinen et al. 1993). Therefore, $\boldsymbol{B}$ can be expressed as the gradient of a scalar potential outside of the spherically symmetric conductor: $\boldsymbol{B} = -\mu_0 \nabla U$. From $\nabla \cdot \boldsymbol{B} = 0$ in Maxwell's equations follows that U is harmonic and, given that U vanishes at infinity, it can be determined uniquely through the normal derivative on the surface of the conductor (Hämäläinen et al. 1993). Thus, U can be written in terms of a line integral along the radius with $\partial U/\partial r = -B_r/\mu_0$ as (Sarvas 1987; Hämäläinen et al. 1993):

$$U(\boldsymbol{r}) = -\int_{t=0}^{\infty} \nabla U(\boldsymbol{r} + t\boldsymbol{e}_r) \cdot \boldsymbol{e}_r dt = \int_{t=0}^{\infty} B_r(\boldsymbol{r} + t\boldsymbol{e}_r) dt \tag{2.14}$$

showing that, even though the tangential field components are affected by the volume currents in a spherically symmetric conductor, knowledge about the volume currents is not required for the estimation of the magnetic induction field $\boldsymbol{B}$ (Hämäläinen et al. 1993). In 1987, Sarvas solved the forward problem analytically for a magnetic induction field $\boldsymbol{B}$ generated by a current dipole in a spherically symmetric conductor (Sarvas 1987; Hämäläinen et al. 1993):

$$\boldsymbol{B}(\boldsymbol{r}) = \frac{\mu_0}{4\pi} \cdot \frac{F(\boldsymbol{r}, \boldsymbol{r}_Q) \cdot \boldsymbol{Q} \times \boldsymbol{r}_Q - (\boldsymbol{Q} \times \boldsymbol{r}_Q \cdot \boldsymbol{e}_r) \cdot \nabla F(\boldsymbol{r}, \boldsymbol{r}_Q)}{F(\boldsymbol{r}, \boldsymbol{r}_Q)^2} \tag{2.15}$$

with

$$F(\boldsymbol{r}, \boldsymbol{r}_Q) = \|\boldsymbol{d}\| \cdot (\|\boldsymbol{r}\| \cdot \|\boldsymbol{d}\| + \|\boldsymbol{r}\|^2 - \boldsymbol{r}_Q \cdot \boldsymbol{r}) \tag{2.16}$$

and

$$\nabla F(\boldsymbol{r}, \boldsymbol{r}_Q) = \left(\frac{\|\boldsymbol{d}\|^2}{\|\boldsymbol{r}\|} + \frac{\boldsymbol{d}\cdot\boldsymbol{r}}{\|\boldsymbol{d}\|} + 2\cdot\|\boldsymbol{d}\| + 2\cdot\|\boldsymbol{r}\|\right) - \left(\|\boldsymbol{d}\| + 2\cdot\boldsymbol{r} + \frac{\boldsymbol{d}\cdot\boldsymbol{r}}{\|\boldsymbol{d}\|}\right)\cdot\boldsymbol{r}_Q\,. \tag{2.17}$$

with $\boldsymbol{d} = \boldsymbol{r} - \boldsymbol{r}_Q$. Now that a solution to the forward problem has been found, the next step is to solve the inverse problem.

2.6.4 THE INVERSE PROBLEM

Since the MEG sensors are not fixed to the head unlike in EEG, different subjects can be seated differently and thus the signals at a specific sensor may not be directly comparable for two subjects. Therefore, it is a common step in MEG analysis to estimate the current densities that gave rise to the measured signal to circumvent this problem (Gramfort et al. 2013). Combining the activity with the structural brain images then also allows for the direct interpretation of the activity in the context of the underlying anatomy (Brookes et al. 2014). The inverse problem refers to the process of finding the current distribution that gave rise to the measured signal (Hämäläinen et al. 1993).
Unfortunately, given only the magnetic induction on the outside of a conductor, there exist an infinite number of valid current distributions inside the conductor that can explain the observed field (Helmholtz 1853; Hämäläinen and Ilmoniemi 1994). Therefore, the current distribution cannot be determined uniquely. Over the years, various source modeling techniques, that each pose different constraints on the space of possible solutions, have been proposed. A common concept in those methods is the use of the lead field, which is described in the next section.

2.6.4.1 THE LEAD FIELD

The lead field is a useful tool to describe the sensitivity of the pick-up coils to the magnetic field induced by currents at different locations (Hämäläinen and Ilmoniemi 1984). It is a vector field describing the sensor's sensitivity distribution, i.e., for any given current position $\boldsymbol{r}'$, the lead field specifies the direction of the current, which maximizes the output at the sensor and the gain with which the source current affects the output (Parkkonen 2010). Since both $\boldsymbol{E}$ and $\boldsymbol{B}$ are linearly related to $\boldsymbol{J}^p$, the magnetic induction b_i measured at the i^{th} sensor at position $\boldsymbol{r}_i$ can be written as (Hämäläinen et al. 1993; Parkkonen 2010):

$$b_i = \int \boldsymbol{L}_i(\boldsymbol{r}')\cdot\boldsymbol{J}^p(\boldsymbol{r}')d^3\boldsymbol{r}', \tag{2.18}$$

where $\boldsymbol{L}_i$ is the lead field of the i^{th} sensor. $\boldsymbol{L}_i$ depends on the pick-up coil configuration and the conductivity distribution $\sigma(\boldsymbol{r})$ of the tissue (Hämäläinen and Ilmoniemi 1994; Parkkonen 2010). Since these remain constant, the lead field has to be computed only once for each measurement. For a single current dipole at position $\boldsymbol{r_Q}$ (equation (2.12)), the lead field reduces to (Hämäläinen et al. 1993):

$$b_i(\boldsymbol{Q}, \boldsymbol{r_Q}) = \boldsymbol{L}_i(\boldsymbol{r_Q})\cdot\boldsymbol{Q}. \tag{2.19}$$

The magnetic flux through a sensor i consisting of a set of m planar coils is given by (Hämäläinen et al. 1993):

$$b_i(\boldsymbol{Q}, \boldsymbol{r_Q}) = \sum_{j=1}^{m} \int_{A_j} \boldsymbol{B}_{ij}(\boldsymbol{Q}, \boldsymbol{r_Q}) \cdot \boldsymbol{n}_{ij} dA_{ij}, \tag{2.20}$$

where $\boldsymbol{B}_{ij}$ is the magnetic induction at the j^{th} coil of the i^{th} sensor generated by the dipole $\boldsymbol{Q}$ and $\boldsymbol{n}_{ij}$ and A_{ij} are the normal vector and the area of the j^{th} coil of the i^{th} sensor, respectively. By inserting equation (2.20) into equation (2.19), all three components of the lead field $\boldsymbol{L}_i(\boldsymbol{r_Q})$ can be computed (Hämäläinen et al. 1993).

2.6.4.2 Minimum-norm estimate (MNE)

In contrast to the equivalent current dipole model, the minimum-norm estimate (MNE) is a so-called distributed source model (DSM) (Hämäläinen and Ilmoniemi 1994). MNE derives its name from the fact that the estimated primary current is the current with the smallest overall amplitude (in terms of a L2-norm) that is still capable of explaining the observed signal (Hämäläinen et al. 1993; Jensen and Hesse 2010). Instead of placing a single current dipole or a small number thereof in the brain, for a DSM the brain is discretized into a three-dimensional grid G with a current dipole at each grid point (Jensen and Hesse 2010). Any current distribution in the brain is then considered an element of the linear current space $\mathcal{F}$ containing all square-integrable current distributions confined to the set of points G (Hämäläinen et al. 1993). Since the neural brain activity is represented by the primary current density $\boldsymbol{J}^p$, the inverse problem is solved by estimating $\boldsymbol{J}^p$. Let $\boldsymbol{J}_1$ and $\boldsymbol{J}_2$ be two vectors of the current space, then the Euclidian inner product is defined as

$$\langle \boldsymbol{J}_1, \boldsymbol{J}_2 \rangle = \int_G \boldsymbol{J}_1(\boldsymbol{r}') \cdot \boldsymbol{J}_2(\boldsymbol{r}') dG. \tag{2.21}$$

The norm describes the overall amplitude of a current distribution:

$$\|\boldsymbol{J}_k\|^2 = \langle \boldsymbol{J}_k, \boldsymbol{J}_k \rangle = \int_G |\boldsymbol{J}_k(\boldsymbol{r}')|^2 dG. \tag{2.22}$$

Looking at equation (2.18), it becomes evident that only information about primary currents lying in the subspace $\mathcal{F}' = \text{span}(\boldsymbol{L}_1, \dots, \boldsymbol{L}_N)$ of $\mathcal{F}$ with N being the number of sensors can be obtained through measurements of $b_i = \langle \boldsymbol{L}_i, \boldsymbol{J}^p \rangle$ (Hämäläinen and Ilmoniemi 1984; Hämäläinen et al. 1993; Hämäläinen and Ilmoniemi 1994). Since it is impossible to obtain information about currents that are orthogonal to the subspace $\mathcal{F}'$, the lead fields form a natural basis for the estimation of the primary currents. The estimated primary current $\boldsymbol{J}^*$ can then be written as a linear combination of the lead fields (Hämäläinen and Ilmoniemi 1984; Hämäläinen et al. 1993):

$$\boldsymbol{J}^*(\boldsymbol{r}', t) = \sum_{j=1}^{N} w_j(t) \boldsymbol{L}_j(\boldsymbol{r}') = \boldsymbol{w}^T(t) \cdot \mathbf{L}(\boldsymbol{r}'). \tag{2.23}$$

The scalar weights w_j have to be determined in such a way that the estimated magnetic induction at the sensors $\boldsymbol{b}^*(t) = \left(b_1^*(t), \dots, b_N^*(t)\right)^T = \langle \mathbf{L}, \boldsymbol{J}^* \rangle$ recovers the

magnetic induction measured at the sensors $\boldsymbol{b}(t) = \left(b_1(t), \dots, b_N(t)\right)^T$ (Hämäläinen and Ilmoniemi 1984; Hämäläinen et al. 1993). This is equivalent to the minimization problem (Hauk 2004; Breuer 2016):

$$\min[\|\langle \mathbf{L}, \boldsymbol{J}^* \rangle - \boldsymbol{b}(t)\|^2]. \tag{2.24}$$

By using the L2-norm in equation (2.24), the MNE procedure becomes biased towards spatially smoothed solutions (Jensen and Hesse 2010). Solving the problem in (2.24) is equivalent to finding a solution to the set of equations given by (Hämäläinen and Ilmoniemi 1994):

$$\boldsymbol{b}(t) = \boldsymbol{\Gamma}\boldsymbol{w}(t), \tag{2.25}$$

where $\boldsymbol{\Gamma}$ is the inner product matrix of the lead fields with $\boldsymbol{\Gamma}_{ij} = \langle \boldsymbol{L}_i, \boldsymbol{L}_j \rangle$. To solve equation (2.25) for $\boldsymbol{w}$, $\boldsymbol{\Gamma}$ needs to be inverted. Since, generally, the number of grid points N_G is much larger than the number of sensors N, $\boldsymbol{\Gamma}$ can be almost singular with some very small eigenvalues resulting in potentially large errors in the computation of $\boldsymbol{w}$ (Hämäläinen et al. 1993). Regularization is necessary to avoid numerical instabilities (Sarvas 1987; Hämäläinen and Ilmoniemi 1994). Using singular value decomposition, the inner product matrix can be written as $\boldsymbol{\Gamma} = \mathbf{V}\boldsymbol{\Lambda}\mathbf{V}^T$, with $\mathbf{V}\mathbf{V}^T = \mathbf{I}$ and $\boldsymbol{\Lambda} = \mathrm{diag}(\lambda_1, \lambda_2, \dots, \lambda_N)$ where $\lambda_1 > \lambda_2 > \cdots > \lambda_N > 0$ are the eigenvalues of $\boldsymbol{\Gamma}$. Then, $\boldsymbol{\Gamma}^{-1} = \mathbf{V}\boldsymbol{\Lambda}^{-1}\mathbf{V}^T$**.** To obtain a regularized inverse $\tilde{\boldsymbol{\Gamma}}^{-1} = \mathbf{V}\tilde{\boldsymbol{\Lambda}}^{-1}\mathbf{V}^T$, $\boldsymbol{\Lambda}^{-1}$ can be replaced by

$$\tilde{\boldsymbol{\Lambda}}^{-1} = \mathrm{diag}(\lambda_1^{-1}, \dots, \lambda_k^{-1}, 0, \dots, 0), \tag{2.26}$$

with $k < N$ (Hämäläinen et al. 1993). After replacing $\boldsymbol{\Gamma}$ in equation (2.23), the estimated regularized primary current is given by (Hämäläinen and Ilmoniemi 1994):

$$\boldsymbol{J}^*(t) = \left(\tilde{\boldsymbol{\Gamma}}^{-1} \cdot \boldsymbol{b}(t)\right)^T \cdot \mathbf{L}. \tag{2.27}$$

A major advantage of a DSM is that it does not make assumptions about the number or nature of sources, only that the source currents be confined to a certain space, e.g., the brain (Hämäläinen and Ilmoniemi 1994). However, the MNE approach is known for being biased towards superficial sources, often severely misplacing deep sources onto the outer cortex (Dale et al. 2000; Pascual-Marqui 2002). This is a result of the MEG and EEG lead fields being attenuated with increasing source depth (Lin et al. 2006). Depth weighting has been suggested to counteract this bias (Lin et al. 2006).

2.6.4.3 Dynamic statistical parametric mapping[8]

Due to potentially different noise variance at different voxels, activation estimates as maps of raw signal strength are often avoided in fMRI. Instead, noise-normalized

[8] The derivation of the noise-normalized estimate of activity follows (Dale et al. 2000).

statistical parametric maps (SPMs) are used. Correspondingly, the usage of so-called dynamic SPMs (dSPM) was proposed in MEG, where estimated current values are normalized with the estimated noise at each source (Dale et al. 2000). As such, these SPMs provide information about the reliability of the estimated signal. By including a measurement noise term, $\boldsymbol{\eta}$, and considering all grid points simultaneously, equation (2.19) becomes

$$\boldsymbol{b}(t) = \mathbf{L} \cdot \boldsymbol{q}(t) + \boldsymbol{\eta}, \tag{2.28}$$

where the vector $\boldsymbol{q}(t) = \left(q_1(t), \dots, q_{3N_G}(t)\right)^T$ contains the three current dipole components for each of the N_G grid points. Assuming the dipole strength patterns follow a multivariate Gaussian distribution, the maximum *a posteriori* probability estimate for the current dipoles is equivalent to the linear Wiener estimate (Wiener 1949) given by

$$\boldsymbol{q}^*(t) = \mathbf{W}\boldsymbol{b}(t), \tag{2.29}$$

with the inverse operator $\mathbf{W} = \mathbf{R}\mathbf{L}^T(\mathbf{L}\mathbf{R}\mathbf{L}^T + \mathbf{C})^{-1}$ where $\mathbf{R} = \langle \boldsymbol{q}(t)\boldsymbol{q}(t)^T \rangle$ is the spatial covariance matrix of the dipole strength vector and $\mathbf{C} = \langle \boldsymbol{\eta}(t)\boldsymbol{\eta}(t)^T \rangle$ is the spatial (sensor) covariance matrix of the noise (Dale and Sereno 1993; Dale et al. 2000). Due to the linear nature of the Wiener estimate, it is straightforward to calculate for each dipole strength estimate the part of the variance that is due to the sensor noise

$$\mathrm{Var}(q_i^*) = \langle \left(\boldsymbol{W}_i \boldsymbol{\eta}(t)\right)^2 \rangle = \boldsymbol{W}_i \mathbf{C} \boldsymbol{W}_i^T \tag{2.30}$$

with q_i^* being the i^{th} element of the dipole strength vector $\boldsymbol{q}^*$ and $\boldsymbol{W}_i$ being the i^{th} row of the inverse operator $\mathbf{W}$. The noise-normalized estimate of activity for the i^{th} dipole component, z_i, can then be computed as

$$z_i(t) = \frac{q_i^*(t)}{\sqrt{\mathrm{Var}(q_i^*)}} = \frac{\boldsymbol{W}_i \cdot \boldsymbol{b}(t)}{\sqrt{\boldsymbol{W}_i \mathbf{C} \boldsymbol{W}_i^T}}. \tag{2.31}$$

Moreover, the subspace $\mathcal{F}'$ (cf. section 2.6.4.2) can be constrained further to improve the solution: By using information from a structural magnetic resonance imaging (MRI) scan, the MEG solution space can be narrowed down to the main cortical generators of MEG signals, which are located in the gray matter perpendicular to the cortical sheet.

3 CLUSTER-BASED METHODS FOR MASS-UNIVARIATE ANALYSES

Cognitive processes are often investigated by analyzing the cortical responses to certain events or stimuli (Pernet et al. 2015). Typically, these responses are not perfectly localized but distributed across multiple cortical areas (Pernet et al. 2015). Furthermore, there are often multiple experimental conditions to investigate differences in the brain's response (Maris and Oostenveld 2007). However, without prior knowledge about where and when to look for differences, every combination of location and time point has to be tested for significant differences (Maris and Oostenveld 2007; Pernet et al. 2015).

The multiple comparison problem (MCP) states that, for an increasing number of tests, it becomes impossible to control the family-wise error rate (FWER) which refers to the probability of falsely rejecting the null hypothesis for one or more tests (Maris and Oostenveld 2007). For example, for a typical MEG system with 248 sensors and a recording time of one second at a sampling frequency of 1,017.25 Hz, this would result in 252,278 separate tests. At a critical alpha-level of 5%, the null hypothesis would be rejected over 12,000 times just simply due to chance. A conservative approach to solve the MCP is known as the Bonferroni correction where the critical alpha-level is divided by the number of tests (Bonferroni 1936). It is also possible to control the false discovery rate (FDR) to deal with the MCP (Benjamini and Hochberg 1995). However, these methods assume statistical independence of the tests and thus can be too conservative (Maris and Oostenveld 2007; Pernet et al. 2015). Adjacent points in time and in space are for cortical responses typically highly correlated and these spatiotemporal dependencies have to be accounted for in the statistical tests (Pernet et al. 2015).

Cluster-mass methods approach the MCP by grouping adjacent test statistics into clusters and taking the sum of these values (Pernet et al. 2015). Thus, the entire data space is analyzed simultaneously in a mass-univariate approach testing all locations and time points at the same time (Pernet et al. 2015). An advantage of the cluster-mass methods is that they are an effective way of controlling the FWER without requiring a priori choices about locations or time points of effects (Pernet et al. 2015). Thus, it is possible to observe potentially unexpected effects (Pernet et al. 2015). One example for such a cluster-mass approach is spatiotemporal cluster permutation testing (Maris and Oostenveld 2007), which will be explained in more detail in the following sections. The method was used in chapters 8 and 9 to identify cortical regions with significant activations following fixation onset (fixation-related evoked activity).

3.1 SPATIOTEMPORAL CLUSTER PERMUTATION TESTING[9]

Spatiotemporal cluster permutation testing (SCPT) is a nonparametric statistical test in which the multiple comparisons problem (MCP) is addressed by exploiting the spatiotemporal structure of MEG data during the computation of the test statistic (see section 3.3). In this way it is possible to take prior knowledge about the expected effect into account, improving the sensitivity of the statistical test.

For MEG data, it is likely that samples from adjacent locations (e.g., sensors or vertices) and time points exhibit the same effect, a property which can be exploited. By clustering adjacent data points together and performing the test on the maximum cluster only, SCPT reduces the multitude of tests that would ordinarily have to be performed to a single test. In this way the MCP is eliminated. Furthermore, by incorporating the prior knowledge about the spatial and temporal dynamics of the data and performing the statistical tests on the clusters, the sensitivity of the tests can be increased drastically. For example, in a comparison between cluster- and non-cluster-based test statistics, the number of samples needed for cluster-based test statistics to reach significance was only 30% of the number of samples needed for non-cluster-based test statistics. However, there is also a drawback to this method. Since the distribution of cluster-level test statistics is unknown, it first has to be approximated by using a Monte-Carlo simulation.

The explanation of the procedure for SCPT is split into two parts. First, the general steps for a nonparametric permutation test are outlined (section 3.2) and then the calculation of the cluster-level test statistic that is specific to SCPT is explained (section 3.3).

3.2 THE NONPARAMETRIC PERMUTATION TEST

The nonparametric permutation test involves a four-step procedure that results in a valid statistical test where the FWER is equal to the critical alpha-level:

1. Calculate the test statistic based on the trials of the two experimental conditions
2. Compute the test statistic distribution via random permutations
    a. Combine the trials of the two experimental conditions into a single set
    b. Randomly partition the combined set of trials into two subsets whose sizes are equal to the number of trials in the original two sets of trials
    c. Calculate the test statistic on the random partition
    d. Construct a histogram of the maximum test statistic by repeating steps 2b and 2c an infinite number of times
3. Compute the *p*-value as the proportion of random partitions whose test statistic was larger than the original test statistic
4. Reject the null hypothesis if the *p*-value is smaller than the critical alpha-level

[9] Unless stated otherwise, the information in the following sections of this chapter was taken from (Maris and Oostenveld 2007).

By comparing the original test statistic (step 1) with the histogram created in step 2, the question can be answered how likely it is that the difference between the two conditions was simply a product of chance. The steps outlined above are universal and do not depend on the test statistic that is used. This means that the test statistic can be custom-tailored to the question of interest.

The statistical test is called a permutation test only if an infinite number of random partitions were used to create the histogram. Then, the histogram is called the permutation distribution and the associated *p*-value is the permutation *p*-value. However, in practice, this is not possible. Instead, steps 2b and 2c are repeated a large number of times to obtain a so-called Monte-Carlo estimate of the *p*-value. By increasing the number of repetitions, the confidence interval of the Monte-Carlo *p*-value can be made arbitrarily small.

3.3 CLUSTER-LEVEL TEST STATISTIC

For MEG data, it is likely that samples from adjacent sensors and time points exhibit the same effect. As the name suggests, the SCPT uses the spatiotemporal structure of the data to its advantage during the computation of the test statistic (steps 1 and 2c in section 3.2) by clustering together adjacent samples whose individual test statistics (e.g., *t*-values) are above a certain threshold. The calculation of the cluster-level test statistic is split into four steps:

1. Compute the individual test statistic for every sample (combination of location and time)
2. Collect all samples whose (absolute) individual test statistics are greater than a previously chosen threshold
3. Cluster together all collected samples of the same sign that are adjacent in space and time
4. Calculate the cluster-level test statistic by summing up the (absolute) individual test statistics within a cluster

The absolute values are used for a two-tailed test, and, for a one-tailed test, the signed values are used. It is important to note that only the maximum (absolute) cluster-level statistic found in step 4 is used to create the histogram in step 2 of the nonparametric testing procedure in section 3.2.

In neuroscientific experiments, there are often several processes of interest that can occur at the same time and, thus, not only the strongest but multiple clusters may be of interest. By using a vector-valued test statistic consisting of an ordered sequence of cluster-level test statistics one can test multiple clusters for significance at the same time. The first element of the vector-valued test statistic then contains the maximum cluster-level test statistic, the second element contains the second largest cluster-level test statistic and so on.
Similar to step 2d in section 3.2 where the maximum cluster-level test statistic is used to construct the permutation distribution, a permutation distribution for the second/third/etc. largest cluster can be constructed by using the second/third/etc. largest cluster-level test statistic. When using such a vector-valued test statistic, a multivariate permutation distribution is constructed in step 2d of section 3.2. A

vector-valued critical value can then be constructed in such a way that the probability of obtaining a vector-valued test statistic with at least one element surpassing the critical value in the corresponding dimension of the critical-value-vector is equal to the desired false alarm rate. Often a minimum-size requirement is used for the clusters to avoid considering clusters that are deemed too small to reflect physiological activity.

There are two clear advantages to using SCPT for the identification of regions with significant differences in activity between two tasks. First, SCPT solves the MCP without requiring prior knowledge about the data distribution. Second, SCPT enables the incorporation of prior knowledge of the spatiotemporal structure of the data (adjacent points are likely to show comparable dynamics) to improve the sensitivity of the tests. As long as the effect of interest lies in the tails of the data distribution, SCPT provides valid results. However, since it is a Monte-Carlo approach requiring a large number of repetitions, it is very computationally intensive. While the choice of the clustering threshold in step 2 of the computation of the cluster-level test statistic does not affect the FWER, it can have a profound impact on the sensitivity of the test. For example, if the threshold is too high, weak but long-lasting effects will not be detected. Therefore, finding an appropriate threshold is a nontrivial task.

4 EFFECTIVE CONNECTIVITY

In many cases, signals of interest are recorded in the form of multiple simultaneous time series. The statistical relationship among these signals is often investigated by calculating cross correlation functions in the time domain and ordinary coherence functions in the spectral domain (Ding, Chen, and Bressler 2006). However, measures such as ordinary coherence lack directionality and, as such, the results might not be entirely satisfactory (Ding, Chen, and Bressler 2006). For example, in the field of neuroscience, one typically is interested in the information exchange between brain areas, i.e., which areas of the brain drive activity in other areas. Measures that can quantify the influence of one area over another are typically referred to under the umbrella term of effective connectivity as opposed to functional connectivity which typically refers to connectivity measures lacking directionality (Friston 2011).

There are several different methods for the estimation of directed interactions between multivariate time series such as dynamic causal modeling (Friston, Harrison, and Penny 2003), phase transfer entropy (Lobier et al. 2014), phase slope index (Nolte et al. 2004), and directed information (Marko 1973; Massey 1990).
Methods such as directed transfer function (Kaminski and Blinowska 1991) and (generalized) partial directed coherence (Baccalá and Sameshima 2001; Baccalá, Sameshima, and Takahashi 2007) belong to a popular family of effective connectivity methods based on the concepts of Granger causality, which is explained in more detail in the following sections.

In chapter 8, the goal-directed behavior during the search task was investigated. Since a specific target has to be located, additional top-down components are expected to emerge during the search task as compared to the free viewing task. To identify these components, whole-brain effective connectivity networks were computed using generalized partial directed coherence (GPDC). GPDC was chosen based on its ability to effectively disentangle direct and indirect interactions and a good performance in noisy environments (Fasoula, Attal, and Schwartz 2013).

4.1 GRANGER CAUSALITY

In 1956, Wiener laid the groundwork for Granger causality in time series analysis on the general premise that cause precedes effect (Wiener 1956): *If the prediction of future values of a time series can be improved by including past values of a second time series, then there is said to be a causal influence of the second time series on the first*. This was at first only a theoretical construct until Granger devised a mathematical formulation in terms of autoregressive models in 1969 (Granger 1969): *If the variance of the autoregressive prediction error of a time series can be reduced by including past values of a second time series, then the second time series is said to have a causal influence on the first.*
Several important advancements in the field of Granger causality were made by Geweke (Geweke 1982, 1984). First, if there are more than two simultaneous recordings, caution is advised since the inferred, supposedly direct causal relation between two time series may then, in fact, be any mix of direct interactions and

indirect interactions mediated by a third time series. To address this issue, Geweke proposed the use of conditional Granger causality (see section 4.4). Second, one is often interested in the spectral representation of causal interactions and Geweke developed a technique to express time domain Granger causality in its frequency components. Last, Geweke also noted that Granger causality can be computed for multivariate sets of variables (see section 4.5).

4.2 AUTOREGRESSIVE MODELS[10]

Autoregressive models provide the mathematical framework for the calculation of Granger causality (Granger 1969; Florin 2010). A univariate time series X can be written as an autoregressive model of order p, AR(p), if X can be expressed as a linearly weighted sum of its past p values (W. H. Greene 2003; Lütkepohl 2005; Florin 2010):

$$X(t) = a_0 + a_1 X(t-1) + \cdots + a_p X(t-p) + \eta(t), \quad t = 1, \dots, N. \tag{4.1}$$

- $X(t)$ – time series at time point t
- a_i – coefficient of weight of the $X(t-i)$ term
- $\eta(t)$ – error term representing a white noise process
- N – number of time points
- p – model order

Similarly, an n-dimensional multivariate time series

$$\boldsymbol{X}(t) = [X_1(t), X_2(t), \dots, X_n(t)]^T, \tag{4.2}$$

i.e., a set of n simultaneously observed univariate time series, can be written as a multivariate autoregressive model of order p, MVAR(p), if $\boldsymbol{X}(t)$ can be expressed as a linearly weighted sum of its past p values:

$$\boldsymbol{X}(t) = \boldsymbol{A}_0 + \sum_{k=1}^{p} \mathbf{A}(k)\, \boldsymbol{X}(t-k) + \boldsymbol{E}(t), \tag{4.3}$$

where $\mathbf{A}(k)$ is an $(n \times n)$ matrix containing the autoregressive coefficients for the k^{th} time lag, $\boldsymbol{E}(t)$ is a $(n \times 1)$ vector of white-noise error terms representing the true error, and $\boldsymbol{A}_0$ is a fixed $(n \times 1)$ vector of intercept terms, which allows for nonzero mean values of $\boldsymbol{X}(t)$ (Geweke 1982; Florin 2010; Lütkepohl 2005).
If $\mathbf{A}$ is not known, it can be estimated from the sample data. The residual vector $\boldsymbol{\varepsilon}(t)$ then captures the deviation of the estimated values $\widehat{\boldsymbol{X}}(t) = \widehat{\boldsymbol{A}}_0 + \sum_{k=1}^{p} \widehat{\mathbf{A}}(k)\, \boldsymbol{X}(t-k)$ from the true values $\boldsymbol{X}(t)$, i.e., $\boldsymbol{\varepsilon}(t) = \boldsymbol{X}(t) - \widehat{\boldsymbol{X}}(t)$. One way of estimating $\mathbf{A} = \big(\boldsymbol{A}_0, \mathbf{A}(1), \dots, \mathbf{A}(p)\big)$ is to cast the MVAR model as an ordinary regression model for which the parameters can be estimated using least squares (section 4.2.3). There are two important points that have to be considered for the model estimation: stationarity of the time series and choice of the model order.

[10] Unless stated otherwise, the information in this section and its two sub-sections was taken from (Florin 2010).

4.2.1 STATIONARITY

A time series $X(t)$ has to be at least weakly stationary to be able to consistently estimate the coefficients (W. H. Greene 2003; Florin 2010), i.e., estimates of the autoregressive coefficients converge to the true coefficient values in probability for $N \to \infty$, where N is the number of data points. This implies that the major characteristics of the time series' underlying stochastic process do not change over time. Two conditions, mean and covariance stationarity, have to be met for a time series to be considered weak/ wide-sense stationary (W. H. Greene 2003; Florin 2010):

1. The expected value $E\big(X(t)\big) = \mu \; \forall \; t \in \mathbb{Z}$,
2. The autocovariance $Cov\big(X(s), X(t)\big) = E\big((X(s) - \mu)(X(t) - \mu)\big)$ depends only on the distance between time points $|t - s| \; \forall \; t, s \in \mathbb{Z}$.

The special case of $t = s$ in the second condition also implies a constant variance over time. Depending on which of these conditions is violated, three types of non-stationarity may arise: 1) a structural break, 2) a deterministic trend, or 3) a stochastic trend.

A structural break occurs when the mean or the covariance changes at a certain point in time in the data. This is highly relevant in the case of neural data since the recorded signals may be interpreted as a function of the underlying functional states of the brain. For example, when the neural system transitions from one state to another, structural breaks may be observed (Lopes Da Silva 2010; Florin 2010). As such, it may be inappropriate to treat the signal as stationary. Particular care has to be taken with respect to event-related studies where transitions between states might be triggered by the events. A windowing technique combined with subtracting the evoked response from the single trials may, for example, be used to mitigate the problem (Ding et al. 2000).
Structural breaks can commonly be identified by simple visual inspection but there are also statistical tests like the Chow-test, which can be applied to achieve the same (Chow 1960; Andrews and Ploberger 1994; Ploberger and Kramer 1992; Nyblom 1989; Hansen 2000; Florin 2010).

A deterministic trend is the result of a linear time trend in the data. Several methods can be used to transform the time series into a stationary series. One can either subtract the trend, differentiate the time series, or consider the time trend in the autoregressive equation.

A stochastic trend occurs if an infinite number of past points influence the present one. This is equivalent to the time series having a permanent memory and an infinite unconditional variance. Stochastic trends can be identified by testing for so-called unit roots (W. H. Greene 2003; Florin 2010). The concept of unit roots can be illustrated by rewriting the autoregressive model in terms of the lag operator L with:

$$L^i X(t) = X(t - i). \tag{4.4}$$

Equation (4.1) then becomes:

$$\left(1 - a_1 L - a_2 L^2 - \cdots - a_p L^p\right) X(t) = a_0 + \eta(t). \tag{4.5}$$

The left-hand side of equation (4.5) is called the characteristic polynomial. By setting the characteristic polynomial to zero and solving for L, the roots of the characteristic polynomial can be obtained (Lütkepohl 2005; Florin 2010). If all roots of the characteristic polynomial lie outside the complex unit circle ($|L| > 1$), the autoregressive process is stationary and similarly if at least one of the roots lies on or inside the complex unit circle, the process is not stationary (Lütkepohl 2005; Florin 2010). Nonstationary time series can be made stationary by differencing once for every unit root, i.e., $\Delta^d X(t) = (1 - L)^d X(t)$ where d is the number of unit roots (Lütkepohl 2005; Florin 2010). Popular tests for the identification of unit roots are the augmented Dickey-Fuller (ADF) and the Kwiatkowski-Phillips-Schmidt-Shin (KPSS) tests (W. H. Greene 2003; Kwiatkowski et al. 1992; Seabold and Perktold 2010).

Similar to equation (4.5), the MVAR model in equation (4.3) can be written in terms of the lag operator L (Lütkepohl 2005):

$$\left(\mathbf{I} - \mathbf{A}_1 L - \mathbf{A}_2 L^2 - \cdots - \mathbf{A}_p L^p\right) \boldsymbol{X}(t) = \boldsymbol{A}_0 + \boldsymbol{E}(t), \tag{4.6}$$

where $\mathbf{I}$ is the identity matrix and $\mathbf{A}(L) = \left(\mathbf{I} - \mathbf{A}_1 L - \mathbf{A}_2 L^2 - \cdots - \mathbf{A}_p L^p\right)$ is the characteristic polynomial. Multiplying equation (4.6) from the left with the adjoint of $\mathbf{A}(L)$ yields (Lütkepohl 2005):

$$|\mathbf{A}(L)| \boldsymbol{X}(t) = \mathrm{adj}\big(\mathbf{A}(L)\big)\big(\boldsymbol{A}_0 + \boldsymbol{E}(t)\big), \tag{4.7}$$

where $|\cdot|$ and $\mathrm{adj}(\cdot)$ denote the determinant and the adjoint of a matrix, respectively. It is important the note that the determinant is a scalar meaning that all components of $\boldsymbol{X}(t)$ have the same univariate AR operator $|\mathbf{A}(L)|$ in this representation (Lütkepohl 2005). If all roots of $|\mathbf{A}(L)|$ lie outside of the complex unit circle, the multivariate autoregressive process is stable, which implies stationarity (Lütkepohl 2005).

Now let there be d unit roots in $|\mathbf{A}(L)|$. If all other roots lie outside of the complex unit circle, $|\mathbf{A}(L)|$ can be rewritten as (Lütkepohl 2005):

$$|\mathbf{A}(L)| = \alpha(L)(1 - L)^d = \alpha(L)\Delta^d, \tag{4.8}$$

where Δ^d is the differencing operator and $\alpha(L)$ is invertible. Hence it becomes clear that $\Delta^d \boldsymbol{X}(t)$ represents a stationary process with stationary components upon differencing (Lütkepohl 2005).

In summary, stationarity of the time series is an important prerequisite for the validity of the estimated (multivariate) AR models. However, while stationarity can be achieved through differencing, it may pose problems when estimating MVAR models based on multivariate time series. For example, it is a prerequisite that the time series are not cointegrated as differencing may otherwise disturb the

relationships between the original variables (Lütkepohl 2005). A common method to test for cointegration prior to differencing is the Engle-Granger two step method (Engle and Granger 1987).

4.2.2 Model order selection

With infinite data length, it would not be necessary to specify a model order. Due to the law of large numbers, all redundant data lags in the coefficient matrices **A** would consistently become zero. Alas, since time series in real measurements are always finite, the choice of an appropriate model order becomes an important issue in AR modeling. Choosing a model order that is too low can lead to a poor representation of the data, whereas a model order that is too high may lead in practice to problems of model estimation (Bressler and Seth 2011).
Minimizing the Akaike information criterion (AIC) is a common procedure for estimating an appropriate model order (Akaike 1974; Florin 2010). For MVAR models, the AIC is defined as (Lütkepohl 2005):

$$\mathrm{AIC}(p) = \log\left[\det\left(\widehat{\boldsymbol{\Sigma}}\right)\right] + \frac{2n^2p}{N_{total}} \tag{4.9}$$

with p being the model order, n being the number of simultaneously observed time series, and N_{total}being the total number of data points from all the trials. $\widehat{\boldsymbol{\Sigma}}$ is an estimator of the white-noise covariance matrix, which can be obtained from the residuals $\boldsymbol{\varepsilon}(t)$ of the fitted MVAR model of order p (Lütkepohl 2005). Due to the fact that N_{total} is often very large for neurobiological data, the AIC may not achieve a minimum for a reasonable range of p (Ding, Chen, and Bressler 2006). Furthermore, asymptotically, there is a non-zero probability that the AIC overestimates the true model order (Lütkepohl 2005; Florin 2010). Here, two consistent estimators of the true model order, where the estimated model order converges to the true model order with increasing N_{total}, are presented. The Bayesian information criterion (BIC) (Schwarz 1978; Lütkepohl 2005; Florin 2010), defined as

$$\mathrm{BIC}(p) = \log\left[\det\left(\widehat{\boldsymbol{\Sigma}}\right)\right] + \frac{2n^2p}{N_{total}} \cdot \frac{\log N_{total}}{2}, \tag{4.10}$$

may perform better than the AIC in neurobiological applications as it can compensate for the large number of data points (Ding, Chen, and Bressler 2006). Instead of $0.5 \cdot \log N_{total}$, the Hannan-Quinn information criterion (HQIC) uses $\mathrm{loglog}\, N_{total}$ as a correction (Hannan and Quinn 1979; Lütkepohl 2005):

$$\mathrm{HQIC}(p) = \log\left[\det\left(\widehat{\boldsymbol{\Sigma}}\right)\right] + \frac{2n^2p}{N_{total}} \cdot \mathrm{loglog}\, N_{total}. \tag{4.11}$$

4.2.3 Multivariate least squares estimation[11]

Let there be an n-dimensional multivariate time series $\boldsymbol{X}(t) = [X_1(t), X_2(t), \dots, X_n(t)]^T$, which was produced by a stable (stationary) MVAR(p) process (eq. (4.3)). Here it will be assumed that the intercept $\boldsymbol{A}_0$, the coefficient

[11] This section is based on chapters 3.1 and 3.2 of (Lütkepohl 2005).

matrices $\mathbf{A}(k)$, and the covariance matrix $\mathbf{\Sigma}$ of the white-noise error terms are all unknown and have to be estimated from the sample data. Furthermore, it is assumed that for each of the n variables there is a sample of size M available with additional p pre-sample values for the sake of simplifying the notation. The following notation is now defined:

$$\begin{aligned}
\mathbf{X} &\coloneqq \big(\boldsymbol{X}(1), \dots, \boldsymbol{X}(M)\big) && (n \times M), \\
\mathbf{A} &\coloneqq \big(\boldsymbol{A}_0, \mathbf{A}(1), \dots, \mathbf{A}(p)\big) && \big(n \times (np+1)\big), \\
\boldsymbol{Z}(t) &\coloneqq \begin{bmatrix} 1 \\ \boldsymbol{X}(t) \\ \vdots \\ \boldsymbol{X}(t-p+1) \end{bmatrix} && \big((np+1) \times 1\big), \\
\mathbf{Z} &\coloneqq \big(\boldsymbol{Z}(1), \dots, \boldsymbol{Z}(M-1)\big) && \big((np+1) \times M\big), \\
\mathbf{E} &\coloneqq \big(\boldsymbol{E}(1), \dots, \boldsymbol{E}(M)\big) && (n \times M),
\end{aligned} \tag{4.12}$$

which allows to rewrite equation (4.3) in a compact form:

$$\mathbf{X} = \mathbf{A}\mathbf{Z} + \mathbf{E}. \tag{4.13}$$

By using the column stacking operator vec (see Appendix 11.1.2 for definition) the notation can be simplified further:

$$\begin{aligned}
\boldsymbol{x} &\coloneqq \mathrm{vec}(\mathbf{X}) && (nM \times 1), \\
\boldsymbol{\alpha} &\coloneqq \mathrm{vec}(\mathbf{A}) && \big((n^2p+n) \times 1\big), \\
\boldsymbol{e} &\coloneqq \mathrm{vec}(\mathbf{E}) && (nM \times 1).
\end{aligned} \tag{4.14}$$

The covariance matrix of $\boldsymbol{e}$ is given by $\mathbf{\Sigma_e} = \mathbf{I}_M \otimes \mathbf{\Sigma}$, where $\otimes$ is the Kronecker product (see Appendix 11.1.1 for definition) and $\mathbf{I}_M$ is the M-dimensional identity matrix. Applying the column stacking operator to both sides of equation (4.13) yields:

$$\boldsymbol{x} = (\mathbf{Z}^T \otimes \mathbf{I}_n)\boldsymbol{\alpha} + \boldsymbol{e}. \tag{4.15}$$

The multivariate least squares estimate (or generalized least squares estimate) is now the solution that minimizes:

$$\begin{aligned}
S(\boldsymbol{\alpha}) &= \boldsymbol{e}^T(\mathbf{I}_M \otimes \mathbf{\Sigma})^{-1}\boldsymbol{e} \\
&= \boldsymbol{x}^T(\mathbf{I}_M \otimes \mathbf{\Sigma^{-1}})\boldsymbol{x} + \boldsymbol{\alpha}^T(\mathbf{Z}\mathbf{Z}^T \otimes \mathbf{\Sigma^{-1}})\boldsymbol{\alpha} - 2\boldsymbol{\alpha}^T(\mathbf{Z} \otimes \mathbf{\Sigma^{-1}})\boldsymbol{x}.
\end{aligned} \tag{4.16}$$

Setting the partial derivative $\partial S(\boldsymbol{\alpha})/\partial \boldsymbol{\alpha}$ to zero yields the least squares estimator:

$$\begin{aligned}
\hat{\boldsymbol{\alpha}} &= ((\mathbf{Z}\mathbf{Z}^T)^{-1} \otimes \mathbf{\Sigma})(\mathbf{Z} \otimes \mathbf{\Sigma^{-1}})\boldsymbol{x} \\
&= ((\mathbf{Z}\mathbf{Z}^T)^{-1}\mathbf{Z} \otimes \mathbf{I}_M)\boldsymbol{x}.
\end{aligned} \tag{4.17}$$

If $\boldsymbol{X}(t)$ has a continuous distribution, $\mathbf{Z}\mathbf{Z}^T$ will be nonsingular resulting in the Hessian of $S(\boldsymbol{\alpha})$,

$$\frac{\partial^2 S(\boldsymbol{\alpha})}{\partial \boldsymbol{\alpha} \partial \boldsymbol{\alpha}^T} = 2(\mathbf{Z}\mathbf{Z}^T \otimes \boldsymbol{\Sigma}^{-1}), \tag{4.18}$$

being positive definite and ultimately confirming that $\hat{\boldsymbol{\alpha}}$ is a minimizing solution to equation (4.16).

4.2.4 Considerations for the estimation of multivariate autoregressive models

A useful indication that an estimated MVAR model is misspecified is that the residuals of the estimated model do not resemble white noise processes. This can be tested with the Li-McLeod Portmanteau (LMLP) test (W. K. Li and McLeod 1981; Lütkepohl 2005).

Furthermore, two tests have been suggested to assert whether the amount of data suffices for the estimation of the MVAR models (Ding et al. 2000; Schlögl and Supp 2006). First, a fundamental limitation of any time-frequency analysis is the uncertainty principle between the time and frequency domain. It states that the product of time and frequency resolution is always larger than some constant, i.e., $\Delta T \cdot \Delta F > c$, where ΔT is the time resolution and ΔF is the frequency resolution and $c = 1/\sqrt{m}$ when averaging an ensemble of m epochs. One can reasonably assume that the frequency resolution can be approximated by $\Delta F = F_s/p$, where F_s is the sampling frequency and p is the MVAR model order (Schlögl and Supp 2006). By substituting these values in the *T*-*F* uncertainty condition and rearranging for p, one arrives at the following condition for MVAR estimation (Schlögl and Supp 2006):

$$N_s\sqrt{m} > p, \tag{4.19}$$

where $N_s = \Delta T \cdot F_s$ is the number of samples per time series per epoch. Second, basic estimation theory states that the number of samples should be larger than the number of estimates. For n simultaneously recorded time series, there are $n(np + 1)$ values in the coefficient matrix $\mathbf{A}$ (cf. section 4.2.3) to be estimated from $n \cdot N_s \cdot m$ sample values resulting in the following condition (Schlögl and Supp 2006):

$$\frac{N_s m}{np + 1} > 1. \tag{4.20}$$

Finally, the consistency test allows to determine how much of the correlation structure in the data was captured by the fitted MVAR models (Ding et al. 2000).

4.3 PAIRWISE GRANGER CAUSALITY IN BIVARIATE TIME SERIES[12]

Let there be two simultaneously recorded, wide-sense stationary time series $X(t)$ and $Y(t)$, which can be written in their joint representation as two so-called unrestricted autoregressive models of order p:

$$X(t) = \sum_{k=1}^{p} a_1(k)X(t-k) + \sum_{k=1}^{p} b_1(k)Y(t-k) + \varepsilon_1(t), \tag{4.21}$$

$$Y(t) = \sum_{k=1}^{p} c_1(k)X(t-k) + \sum_{k=1}^{p} d_1(k)Y(t-k) + \eta_1(t), \tag{4.22}$$

where the autoregressive models contain past values of both $X(t)$ and $Y(t)$. The error terms of the unrestricted models are serially uncorrelated and their contemporaneous covariance matrix is given by (Geweke 1982; Ding, Chen, and Bressler 2006):

$$\mathbf{\Sigma} = \begin{pmatrix} \Sigma_1 & \Upsilon_1 \\ \Upsilon_1 & \Gamma_1 \end{pmatrix}, \tag{4.23}$$

where $\Sigma_1 = \mathrm{var}\big(\varepsilon_1(t)\big)$, $\Gamma_1 = \mathrm{var}\big(\eta_1(t)\big)$, and $\Upsilon_1 = \mathrm{cov}\big(\varepsilon_1(t), \eta_1(t)\big)$. In the so-called restricted autoregressive models, the variables are only regressed on past values of themselves:

$$X(t) = \sum_{k=1}^{p} a_2(k)X(t-k) + \varepsilon_2(t), \;\; \mathrm{var}\big(\varepsilon_2(t)\big) = \Sigma_2 \tag{4.24}$$

$$Y(t) = \sum_{k=1}^{p} b_2(k)Y(t-k) + \eta_2(t), \;\; \mathrm{var}\big(\eta_2(t)\big) = \Gamma_2. \tag{4.25}$$

If $X(t)$ and $Y(t)$ are independent, then the autoregressive coefficients $\{b_1(k)\}$ and $\{c_1(k)\}$ are uniformly zero and the unrestricted models are equal to the restricted models. Additionally, $\Upsilon_1 = 0$, $\Sigma_1 = \Sigma_2$, and $\Gamma_1 = \Gamma_2$. However, if past values of $Y(t)$ contain information relevant to the prediction of $X(t)$, the variance of the error term $\varepsilon_1(t)$ becomes smaller than the variance of $\varepsilon_2(t)$ and Y is said to Granger-cause X. Similarly, if the variance of $\eta_1(t)$ is smaller than the variance of $\eta_2(t)$, X is said to Granger-cause Y. The causal influences of Y on X and of X on Y can be quantified as (Granger 1969; Geweke 1982; Ding, Chen, and Bressler 2006):

$$F_{Y\to X} = \ln \frac{\Sigma_2}{\Sigma_1}, \tag{4.26}$$

[12] The derivation of pairwise Granger causality follows the introductory article to Granger causality by Ding and colleagues (Ding, Chen, and Bressler 2006) who in turn based their work on (Geweke 1982, 1984).

$$F_{X\to Y} = \ln\frac{\Gamma_2}{\Gamma_1}. \tag{4.27}$$

If $X(t)$ and $Y(t)$ are independent, $F_{Y\to X}$ and $F_{X\to Y}$ would both be equal to zero. On the other hand, a positive $F_{Y\to X}$ or $F_{X\to Y}$ would indicate the presence of a causal influence from Y on X or X on Y, respectively.

Unfortunately, the restricted and unrestricted autoregressive models are usually not known and as a result, estimates of the covariance matrices have to be computed based on the residuals $\varepsilon(t)$ of the estimated AR models. In equations (4.26) and (4.27), the covariance matrices are then replaced with their estimates $\hat{\Sigma}_1$, $\hat{\Sigma}_2$, $\hat{\Gamma}_1$, and $\hat{\Gamma}_2$. Statistical significance of, for example, $F_{Y\to X}$ can then be tested with an F-test where the null hypothesis reads "Y does not Granger-cause X" (Bressler and Seth 2011). The F-statistic is given by (Bressler and Seth 2011):

$$F_{p,T-2p-1} = \frac{(\mathrm{SSR}_r - \mathrm{SSR}_u)/p}{\mathrm{SSR}_u/(T-2p-1)}. \tag{4.28}$$

- SSR_r – sum of squared residuals of the estimated restricted autoregressive model
- SSR_u – sum of squared residuals of the estimated unrestricted autoregressive model
- T – number of observations or number of recorded data points
- p – model order

It is important to note that this result is only of limited use in neuroscience since there is usually a complex system of multiple interacting time series. And, as Granger stated, a third time series influencing the first two may lead to spurious causality results since the causal relation between the two time series may then be direct, indirect through mediation by the third time series, or a combination of both (Granger 1980; Ding, Chen, and Bressler 2006).

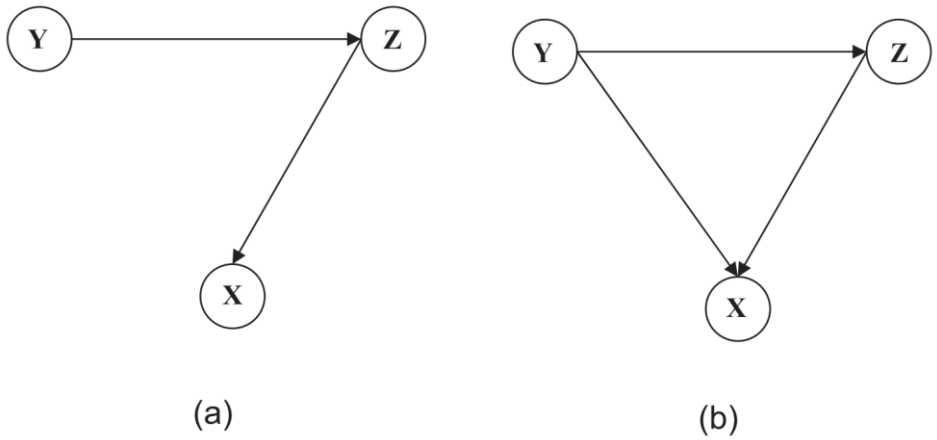

Figure 7: Two separate causality patterns which cannot be distinguished by simple pairwise Granger causality. Figure reprinted from (Ding, Chen, and Bressler 2006). Copyright 2006 by John Wiley and Sons.

4.4 Trivariate time series and conditional Granger causality[13]

To disentangle direct from indirect interactions, conditional Granger causality may be used (Geweke 1982, 1984; Ding, Chen, and Bressler 2006). The basic principle is very similar to the bivariate case, the third time series is simply incorporated explicitly into the equations. Now let there be three simultaneously recorded time series, $X(t)$, $Y(t)$, and $Z(t)$.

To test whether there is a direct interaction from $Y(t)$ to $X(t)$ (Figure 7a) or if there is an indirect interaction mediated by $Z(t)$ (Figure 7b), the unrestricted, joint autoregressive representations for all three time series are constructed:

$$X(t) = \sum_{k=1}^{p} a_3(k)X(t-k) + \sum_{k=1}^{p} b_3(k)Y(t-k) + \sum_{k=1}^{p} c_3(k)Z(t-k) + \varepsilon_3(t), \tag{4.29}$$

$$Y(t) = \sum_{k=1}^{p} d_3(k)X(t-k) + \sum_{k=1}^{p} e_3(k)Y(t-k) + \sum_{k=1}^{p} g_3(k)Z(t-k) + \eta_3(t), \tag{4.30}$$

$$Z(t) = \sum_{k=1}^{p} u_3(k)X(t-k) + \sum_{k=1}^{p} v_3(k)Y(t-k) + \sum_{k=1}^{p} w_3(k)Z(t-k) + \gamma_3(t), \tag{4.31}$$

where the contemporaneous covariance matrix of the error terms is given by:

$$\mathbf{\Sigma}_3 = \begin{pmatrix} \Sigma_{xx} & \Sigma_{xy} & \Sigma_{xz} \\ \Sigma_{yx} & \Sigma_{yy} & \Sigma_{yz} \\ \Sigma_{zx} & \Sigma_{zy} & \Sigma_{zz} \end{pmatrix}. \tag{4.32}$$

Then the restricted, joint autoregressive representations for $X(t)$ and $Z(t)$ are constructed:

$$X(t) = \sum_{k=1}^{p} a_4(k)X(t-k) + \sum_{k=1}^{p} b_4(k)Z(t-k) + \varepsilon_4(t), \tag{4.33}$$

$$Z(t) = \sum_{k=1}^{p} c_4(k)X(t-k) + \sum_{k=1}^{p} d_4(k)Z(t-k) + \gamma_4(t), \tag{4.34}$$

where the contemporaneous covariance matrix of the error terms is given by:

$$\mathbf{\Sigma}_4 = \begin{pmatrix} \Sigma_4 & \Upsilon_4 \\ \Upsilon_4 & \Gamma_4 \end{pmatrix}. \tag{4.35}$$

[13] The derivation of trivariate and conditional Granger causality follows the introductory article to Granger causality by Ding and colleagues (Ding, Chen, and Bressler 2006) who in turn based their work on (Geweke 1982, 1984).

Granger causality from Y_t to X_t conditional on Z_t is defined as:

$$F_{Y\to X|Z} = \ln\frac{\Sigma_4}{\Sigma_{xx}}. \tag{4.36}$$

By simply applying the method multiple times for different time series combinations, conditional Granger causality can also be used for systems with more than three time series.

4.5 Multivariate Granger causality[14]

The equations in section 4.3 can easily be rewritten in terms of MVAR models (cf. section 4.2). First, let $\boldsymbol{X}(t) = [X_1(t), \dots, X_n(t)]^T$ be a vector of n simultaneously recorded, weakly stationary time series, which can be written as an MVAR model:

$$\boldsymbol{X}(t) = \sum_{k=1}^{p} \mathbf{A}(k)\boldsymbol{X}(t-k) + \boldsymbol{E}(t). \tag{4.37}$$

After splitting $\boldsymbol{X}(t)$ into two subvectors, $\boldsymbol{V}(t)$ and $\boldsymbol{W}(t)$ of shapes $k \times N$ and $l \times N$, respectively, two unrestricted models can be constructed from the subvectors analogous to section 4.3:

$$\boldsymbol{V}(t) = \sum_{k=1}^{p} \mathbf{A}_1(k)\boldsymbol{V}(t-k) + \sum_{k=1}^{p} \mathbf{B}_2(k)\boldsymbol{W}(t-k) + \boldsymbol{\varepsilon}_1(t), \operatorname{var}\big(\boldsymbol{\varepsilon}_1(t)\big) = \boldsymbol{\Sigma}_1, \tag{4.38}$$

$$\boldsymbol{W}(t) = \sum_{k=1}^{p} \mathbf{C}_1(k)\boldsymbol{V}(t-k) + \sum_{k=1}^{p} \mathbf{D}_1(k)\boldsymbol{W}(t-k) + \boldsymbol{\eta}_1(t), \operatorname{var}\big(\boldsymbol{\eta}_1(t)\big) = \boldsymbol{\Gamma}_1, \tag{4.39}$$

with the contemporaneous covariance matrix of the error terms given by:

$$\boldsymbol{\Sigma} = \begin{pmatrix} \boldsymbol{\Sigma_1} & \boldsymbol{\Upsilon}_1 \\ \boldsymbol{\Upsilon}_1^T & \boldsymbol{\Gamma}_1 \end{pmatrix}. \tag{4.40}$$

The restricted MVAR models then read:

$$\boldsymbol{V}(t) = \sum_{k=1}^{p} \mathbf{A}_2(k)\boldsymbol{V}(t-k) + \boldsymbol{\varepsilon}_2(t), \;\; \operatorname{var}\big(\boldsymbol{\varepsilon}_2(t)\big) = \boldsymbol{\Sigma}_2, \tag{4.41}$$

$$\boldsymbol{W}(t) = \sum_{k=1}^{p} \mathbf{B}_2(k)\boldsymbol{W}(t-k) + \boldsymbol{\eta}_2(t), \;\; \operatorname{var}\big(\boldsymbol{\eta}_2(t)\big) = \boldsymbol{\Gamma}_2. \tag{4.42}$$

Similar to the bivariate case, the causal influences between $\boldsymbol{W}(t)$ and $\boldsymbol{V}(t)$ are given by:

[14] The derivation of multivariate Granger causality follows (Geweke 1982).

$$F_{W\to V} = \ln\frac{|\mathbf{\Sigma}_2|}{|\mathbf{\Sigma}_1|}, \tag{4.43}$$

$$F_{V\to W} = \ln\frac{|\mathbf{\Gamma}_2|}{|\mathbf{\Gamma}_1|}, \tag{4.44}$$

where $|\cdot|$ denotes the determinant of the enclosed matrix.

4.6 (GENERALIZED) PARTIAL DIRECTED COHERENCE

By combining the results of sections 4.4 and 4.5, it is possible to compute direct interactions between time series in multivariate systems (Ding, Chen, and Bressler 2006). However, this process is computationally demanding as it has to be repeated $M \times (M-1)$ times to compute all independent interactions, where M is the number of time series (Ding, Chen, and Bressler 2006). In contrast, (generalized) partial directed coherence ((G)PDC) is able to find correct connections in a multivariate system by considering all time series simultaneously (Baccalá and Sameshima 2001; Baccalá, Sameshima, and Takahashi 2007). Furthermore, the frequency-domain representation of Granger causality, which does not exist for most Granger causality tests if $M > 2$, is an inherent part of (G)PDC (Baccalá and Sameshima 2001).

To compute PDC for a given MVAR model, the Fourier-transformed autoregressive coefficient matrices, which are given by $\widetilde{\mathbf{A}}(f) = \sum_{k=1}^{p} \mathbf{A}(k)e^{-2\pi i f k}$ (Geweke 1982, 1984; Baccalá and Sameshima 2001), have to be determined first**.** Then, PDC from n to m can be calculated as (Baccalá and Sameshima 2001):

$$\mathrm{PDC}_{mn}(f) = \frac{\bar{A}_{mn}(f)}{\sqrt{\sum_{k=1}^{N} \bar{A}_{kn}(f)\bar{A}_{kn}^{*}(f)}}, \tag{4.45}$$

with $\bar{\mathbf{A}}(f) = \mathbf{I} - \widetilde{\mathbf{A}}(f)$. In 2007, a generalization of PDC was suggested (Baccalá, Sameshima, and Takahashi 2007):

$$\mathrm{GPDC}_{mn}(f) = \frac{\frac{1}{\sigma_m}\bar{A}_{mn}(f)}{\sqrt{\sum_{k=1}^{N} \frac{1}{\sigma_k^2}\bar{A}_{kn}(f)\bar{A}_{kn}^{*}(f)}}, \tag{4.46}$$

where σ_m^2 is the variance of the white-noise error terms $E_m(t)$. By introducing a weighting factor, $1/\sigma_m$, GPDC becomes scale invariant (Baccalá, Sameshima, and Takahashi 2007). Furthermore, variability in GPDC values for short time series is greatly reduced as compared to PDC resulting in increased power when testing for Granger causality (Baccalá, Sameshima, and Takahashi 2007).

To estimate (G)PDC for a stable, n-dimensional MVAR(p) process with standard white-noise error terms, one first has to determine the model order p using one of the selection criteria (section 4.2.2). Then, using the estimated model order, the autoregressive coefficient matrix can be estimated from the data using, for example, multivariate least squares estimation (see section 4.2.3) (Neumaier and Schneider

2001; Billinger, Brunner, and Müller-Putz 2014; Lütkepohl 2005). If the estimator of the autoregressive coefficient matrices converges in distribution, the estimate of the covariance matrix computed based on the residuals converges to the true covariance matrix as well (Lütkepohl 2005). As a result, **A** and σ can be substituted with their estimates in equations (4.45) and (4.46).

5 MACHINE LEARNING

5.1 MULTIVARIATE TIME SERIES CLASSIFICATION

Time series classification (TSC) is the process of assigning an unlabeled time series to one of multiple pre-defined classes (Keogh and Kasetty 2003). Due to its many applications in fields such as engineering, finance, biology, or medicine (Keogh and Kasetty 2003), TSC is one of the most intriguing aspects of data mining. But at the same time it is also one of the most challenging problems in machine learning (Yang and Wu 2006). A distinguishing characteristic of TSC is that the input values are ordered and, as a result, the ordering might provide information relevant to the classification (Bagnall et al. 2017).
With multivariate time series, one also has to consider the added complexity of discriminatory features potentially depending on the interactions of the individual time series (Ruiz et al. 2021). If an algorithm is inherently unable to process multivariate data, it can be adapted to the multivariate case by ensembling univariate classifiers over the multivariate dimensions (Ruiz et al. 2021). However, this approach comes at the disadvantage of ignoring inter-dimensional dependencies.

A recent study reviewed the performance of a variety of different approaches to multivariate TSC on a collection of 26 openly available TSC datasets (Ruiz et al. 2021). The methods included ensembles of univariate classifiers such as Hierarchical Vote Collective of Transformation-based Ensembles (HIVE-COTE) (Bagnall et al. 2020), dedicated multivariate TSC methods such as RandOm Convolutional KErnel Transformation (ROCKET) (Dempster, Petitjean, and Webb 2020), and deep-learning approaches such as InceptionTime (Ismail Fawaz et al. 2020). Due to state-of-the-art classification accuracy and exceptionally fast training times, the authors recommended the general use of ROCKET for multivariate TSC.

Therefore, ROCKET was used in chapter 9 for both multivariate TSC tasks. The fixation-related evoked activity from object fixations was classified based on whether the subjects were performing the memory task or freely viewing the images and single epochs from resting-state recordings were used for neural fingerprinting.

5.2 ROCKET: RANDOM CONVOLUTIONAL KERNEL TRANSFORMATION

ROCKET works by applying a large number of randomly generated convolutional kernels to the (multivariate) time series and training a linear classifier such as ridge regression or logistic regression on the transformed features (Dempster, Petitjean, and Webb 2020). Due to the training complexity being linear in the number of training samples and the length of the time series, ROCKET is a scalable algorithm suitable for large datasets (Dempster, Petitjean, and Webb 2020).

A kernel is defined through five basic parameters: its length l_k and dilation d, the individual weights w_j, a bias term b, and the use of padding (Ismail Fawaz et al. 2019; Dempster, Petitjean, and Webb 2020). Given a univariate time series X, the convolution C of the kernel with the segment of the time series starting at time t is computed by:

$$C_t = w * X_t + b = \sum_{j=0}^{l_k-1} w_j \times X_{t+(j\times d)} + b. \tag{5.1}$$

The convolution for the entire time series is then computed by performing a sliding dot product operation across the entire time series. Whenever there is a pattern in the time series congruent with the kernel, the convolution will result in large values (Ismail Fawaz et al. 2019; Dempster, Petitjean, and Webb 2020). In this way, convolutional kernels can detect basic patterns or shapes. Furthermore, kernels with different dilations but otherwise identical parameters are able to capture the same patterns at different scales (Yu and Koltun 2016). With greater dilations corresponding to lower frequencies and smaller dilations corresponding to higher frequencies, the dilation may also capture frequency information. In fact, it was found that kernels learned in convolutional neural networks may also represent filters for frequency (Krizhevsky, Sutskever, and Hinton 2012; Yosinski et al. 2014; Zeiler and Fergus 2014). Through the combination of different kernels, it is possible to capture complex patterns in the time series (Dempster, Petitjean, and Webb 2020).

Based on their success with regards to image classification and the fact that time series have basically the same topology as images minus one dimension, convolutional neural networks should also deliver good results on time series classification (Ismail Fawaz et al. 2019; Ruiz et al. 2021). However, applying convolutional neural networks to the time series data in the UCR archive (Dau et al. 2019) resulted in high variance in the classification accuracy (Ismail Fawaz et al. 2019). The authors of ROCKET attributed this to the difficulty of learning 'good' kernels with limited amounts of data (Dempster, Petitjean, and Webb 2020). However, it has been shown that it is not necessary to learn appropriate kernel weights (Dempster, Petitjean, and Webb 2020): The use of randomly generated kernels was effective for images (Saxe et al. 2011), DNA sequences (Morrow et al. 2017), and time series (Jimenez and Raj 2019).

ROCKET generates the kernel parameters randomly based on the following pre-defined rules, which yielded the best classification results on the author's development datasets (Dempster, Petitjean, and Webb 2020). The length of a kernel is selected from the set $\{7, 9, 11\}$ with equal probability and the weights are sampled from a normal distribution, $w_j \sim \mathcal{N}(0,1)$. After setting the weights, they are then mean centered, i.e., the mean weight is subtracted. The bias term is sampled from a uniform distribution, $b \sim \mathcal{U}(-1,1)$. An exponential scale is used to sample the dilation with $d = \lfloor 2^x \rfloor, x \sim \mathcal{U}(0, A)$ and $A = \log_2\left(\frac{l_{input}-1}{l_k-1}\right)$. Finally, at the creation of each kernel, a binary decision is made with equal probability whether to use padding, i.e., whether to add $(l_k - 1)/2$ zeros to the beginning and the end of the time series.

In the case of multivariate time series, there is also a sixth kernel parameter, the subset of dimensions that the kernel is applied to (Ruiz et al. 2021). The kernel weights are then generated independently for each dimension and the convolution becomes a sliding dot product between two matrices (Ruiz et al. 2021).

What sets ROCKET apart from previous methods for time series classification using (random) convolutional kernels is the very large number of kernels (the default is 10,000) and their massive variety (Dempster, Petitjean, and Webb 2020). Particularly, ROCKET's effective use of dilation is key for its ability to capture patterns at different scales and frequencies (Dempster, Petitjean, and Webb 2020). Together, the large number of kernels can capture features relevant for time series classification (Dempster, Petitjean, and Webb 2020). Lastly, and potentially most importantly, ROCKET returns for each kernel two features: the maximum value (similar to global max pooling) and the proportion of positive values, a novel feature which provides the classifier with information about how prevalent a pattern is in the time series (Dempster, Petitjean, and Webb 2020).

A linear classifier is then trained on the transformed features. For very large datasets where the number of training examples is significantly higher than the number of features, the authors recommended logistic regression with stochastic gradient descent (Dempster, Petitjean, and Webb 2020). However, a ridge regression classifier with cross validation for the regularization parameter was recommended for smaller datasets (Dempster, Petitjean, and Webb 2020).

6 EXPERIMENTAL SETUP

6.1 EXPERIMENTAL PARADIGM[15]

6.1.1 TASK PROTOCOL

Subjects performed voluntary visual exploration of naturalistic, still images. The images showed everyday-life scenes and in each image, five objects were embedded (see stimulus preparation and presentation). There were three different task conditions: visual searching (VS), memorizing (ME), and free viewing (FV) (Figure 8) and the subjects had to perform 30 trials for each condition resulting in a total of 90 trials per subject. The 90 trials were divided into blocks of three, each block containing one trial of each task in a pseudo-random order to ensure sufficient variability and that the same task cannot occur more than two times in a row. Between the trials, a fixation cross was presented for 3 to 4 s and at the beginning of every two blocks of trials, a recalibration of the eye tracker was scheduled. If there was an apparent drift in gaze location during the trials, a recalibration could also be initiated manually by the operator.
Furthermore, the experiment was divided into three recording runs of 30 trials each to limit the length of single recordings. At the beginning and at the end of each recording run, the head position inside the MEG scanner is recorded. In this way it is possible to estimate the amount of movement during the recording. However, only the head position at the beginning of the recording is used for source localization. Since subjects tend to gradually slouch during the measurement it is good practice to keep the runs relatively short.

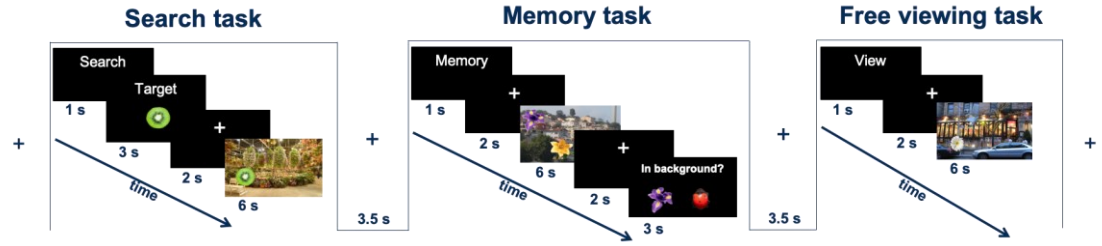

Figure 8: Experimental tasks: the search task the memory task and the free viewing task. In all tasks a natural scene image with five foreign objects was presented for six seconds. Figure reprinted from (Kiefer et al. 2022). Copyright 2022 by Kiefer et al.

At the beginning of each trial, the task was given in German: 'Suche' ('Search') for the search task, 'Merke' ('Memorize') for the memory task, and 'Schaue' ('Look') for the free viewing task.
For the search condition, a target object was displayed for 3 s after the task indicator followed by a fixation cross for 2 s. Then the natural scene image was presented for 6 s. During that time the subjects had to search the image for the target object. Once the object was found, the subjects had to respond by pressing a button with either their left index finger or their right index finger.

[15] The same task protocol and stimuli as described in (Jo, Ito, et al. 2019) were used in this dissertation.

For the memory condition, the instruction was followed by a 2 s display of the fixation cross. Afterwards, the natural scene image containing the 5 objects was presented for 6 s. During this time the subjects had to find and memorize all 5 objects. This was then followed by another 2 s display of the fixation cross. Then two objects, one on the left and one on the right, were presented together with the words 'Im Hintergrund?' ('In the background?'). The subjects had 3 s to decide which one of the two objects was present in the previous natural scene image and to press the button on their left or right with their index fingers accordingly. There was always a single correct answer.
For the free viewing condition, the natural scene image was presented for 6 s after the task indicator and the fixation cross. Here, the subjects were instructed to view the image freely without any task requirements.

6.1.2 STIMULUS PREPARATION

Since the same stimuli were used as in the study of Jo *et al*. (2019a), only a brief illustration of the stimulus creation will follow. Please refer to their paper for a more detailed description. The natural scene image stimuli were created by embedding five object images in background images of natural scenes. A selection of 39 object images consisting of flowers, animals, insects, fruits, furniture, tools, and vehicles, was taken from the Microsoft image gallery, and resized to an average of 143.56 × 141.10 pixels. The 15 background images of 1920 × 1200 pixels were either taken from the internet or they were taken by one of the co-authors of (Jo, Kellermann, et al. 2019). The images were photos of plants, flowers, fruits, gardens, boats, rooms, streets, and churches.
For each background image, two sets of five object images were selected. Three sets of object positions were generated for each combination of a background and an object set. The goal was to let the objects blend in naturally with the background. This resulted in a total of 90 stimulus images, composed of 15 background images × 2 sets of object images × 3 sets of object positions. The three position variants of an identical object-background pair were used for the three different task types (VS, ME, and FV).

6.1.3 STIMULUS PRESENTATION

The stimulus presentation was programmed using Python 2.7 and the Python package PsychoPy 2.0 in particular (Peirce et al. 2019). For the presentation a Barco (Kortrijk, Belgium) FL35 WUXGA projector was used with a resolution of 1920x1200 pixel and a refresh rate of 60 Hz. The projector was placed outside of the magnetically shielded room in front of a small hole to let the light pass through. Inside the magnetically shielded room, a transparent, grey screen was placed between the projector and the MEG chair. While the position of the projector was fixed, the position of the screen and the MEG chair could be adjusted for the images to cover an appropriate degree of visual angle.

6.2 DATA ACQUISITION

6.2.1 MEG SYSTEM

At the Institute for Neuroscience and Medicine – 4 at Forschungszentrum Jülich GmbH a Magnes 3600 WH MEG system is installed, a sixth-generation system developed by 4-D Neuroimaging (San Diego, United States of America). The Magnes 3600 WH scanner features a helmet-style sensor with 248 fully independent MEG detectors at an average inter-detector separation of 2.2 cm. The cross section of the MEG system is depicted in Figure 9. The detection coils are configured as magnetometers (cf. section 2.5), which, in contrast to using gradiometers, greatly increases the sensitivity of the instrument to sources located deep within the brain.

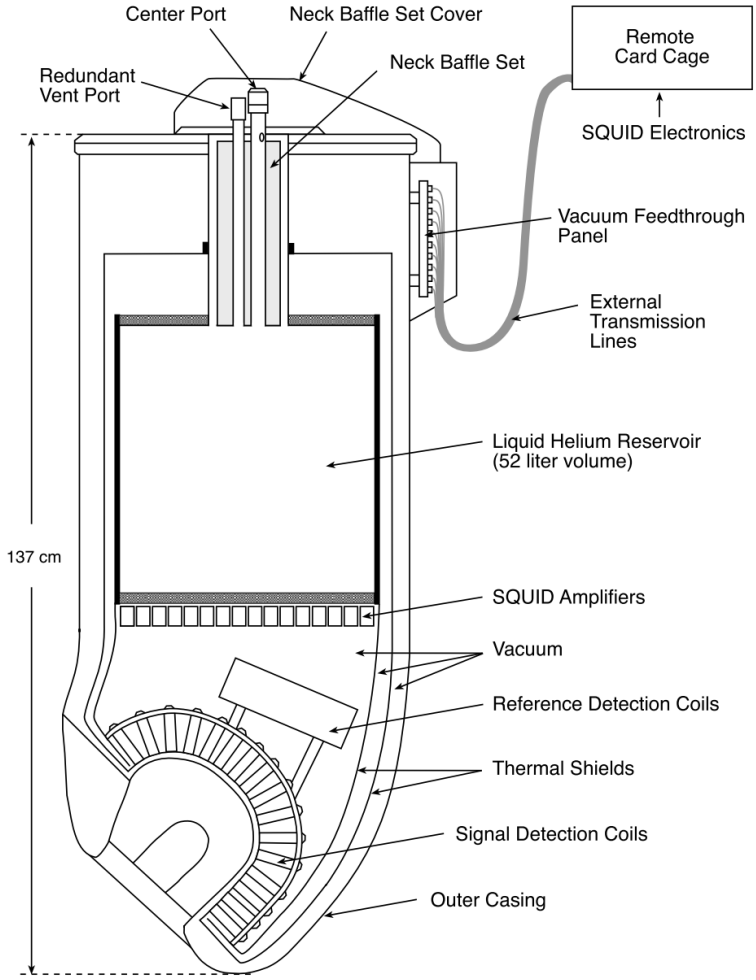

Figure 9: Cross section of the Magnes 3600 WH MEG system. Figure reprinted from (4-D Neuroimaging 2006). Copyright 2006 by CTF MEG Neuro Innovations Inc.

The magnetometers are cooled to superconducting temperatures by conductive heat exchange with a liquid helium reservoir contained within a super-insulated container (dewar). There is a concave, helmet-shaped recess in the dewar into which the subject's head can be inserted. The detection coils are distributed around the recess close to the surface to minimize the distance to the subject's brain (see figures 10 and 13 in (4-D Neuroimaging 2003)). In addition to the magnetometers, there is a sophisticated noise-cancellation package with 14 reference detection coils. Active noise reduction using the signals from the reference coils is applied

both on-line and off-line with the aim of removing magnetic and vibrational noise while preserving signals from the brain. After noise reduction, the typical system performance is a white noise frequency spectrum below 5 $fT/Hz^{1/2}$ (4-D Neuroimaging 2003). The system comes with a subject chair that can be configured for seated or supine recordings, depending on the study paradigm and stimulus presentation method.
Due to the high sensitivity to external noise, the subject, subject chair, dewar, ECG/EOG device, stimulus presentation screen, eye tracker and subject response device are isolated from the environment by a magnetically shielded room made of μ-metal.

6.2.2 ECG AND EOG

While the MEG system recorded the brain activity, the electric signals originating from cardiac and ocular activity were recorded at 5 kHz using Brain Products' (Gilching, Germany) BrainAmp ExG MR system.

6.2.3 EYE TRACKING

For recording the eye movements, the EyeLink 1000 Long-Range System made by SR Research (Ottawa, Ontario, Canada) was used. The movements of the right eye were recorded with a sampling rate of 1000 Hz. The eye tracker was mounted to a vertical bar fixed to the wall inside the magnetically shielded room underneath the projector hole and across from the MEG chair. The height of the eye tracker could be adjusted by sliding it up and down the bar to ensure a good view of the subject's eyes.

The following steps were taken to set up the experiment for each subject. First, the subject was placed in the MEG chair in an upright, seated position. A neck brace was put on the subject to reduce potential head movements during the measurement. The electrodes for the EOG and ECG recordings were then fixed to the subject. Afterwards, the subject's head shape was digitized, and the position of the fiducials was recorded. Using this data, it is later possible to align head-, MEG-, and MR-coordinate systems for source localization. Then the position of the MEG system and chair height were adjusted so that the subject's head was located inside the sensor helmet and the distance between the subject's eyes and the eye tracker was between 100 and 150 cm.
Finally, an appropriate distance between screen, subject, and projector had to be set. Here it was important to confirm that the screen did not cover the eye tracker and, if needed, the vertical position of the eye tracker could be adjusted. The position of the screen relative to the projector affects the size of the projection and the distance between the screen and the subject affects the visual angle. The eye tracking system has a maximum visual angle of 32 × 24° in which the system can reliably track eye movements. To ensure that the images covered this maximum visual angle for each subject, the size of the projected image and the distance from the eyes to the upper and lower edge of the image had to be measured. The size of the projected image allowed for calculating the size of a pixel in cm and with the distances to the edges it was possible to determine how many pixels were needed to cover the appropriate visual angle. With these values the presentation software

automatically adjusted the resolution of the image in pixels, e.g., the size of the image in pixels might now be 1536x1152 covering a visual angle of 32 × 24° in the subject's field of view. Furthermore, the image was centered with respect to the position of the eyes. In the end the image onset diode was placed at the location of the white square indicating image onset (cf. section 6.2.4).
Once the setup of screen, subject, eye tracker, and photodiode was completed, the camera and illuminator of the EyeLink 1000 system had to be focused on the eyes. An illumination level of greater than 75 in the EyeLink software was recommended (SR Research Ltd. 2009).

For the calibration, EyeLink's 13-point calibration method was used (SR Research Ltd. 2009). Thirteen points were distributed across the screen and the subjects had to fixate on these one by one for the eye tracker to learn which location on the screen corresponded to the eyes' positions. Then, the subjects had to fixate on the calibration points a second time to determine the quality of the calibration. If the average deviation was above 0.5° or the maximum deviation at one of the calibration points was higher than 2°, the calibration procedure was repeated.
It is important to note that differences in screen brightness during eye tracker calibration as compared to the measurement may introduce errors. This is because differences in pupil size can affect the gaze position as calculated by the eye tracker (Nyström, Hooge, and Andersson 2016). To achieve a roughly comparable brightness during calibration as compared to the image presentation, the eye tracker calibration was performed with a grey background that was the same size as the images.

6.2.4 Image onset device

An image onset device (IOD) was constructed to measure the exact time point when the image appeared on the screen since there was a delay of the order of 50 ms between the presentation program giving the command to present an image, the digital image information being sent to the projector, and the projector actually presenting the image. The IOD consisted of a small white square presented in the lower right-hand corner of the projection screen and a photodiode at the same location. Every time an image is presented, the diode sends a signal to the response channel of the MEG system and the response channel of the EyeLink system.

6.2.5 MR Scanner

A MAGNETOM Trio 3T MRI scanner made by Siemens (Munich, Germany) was employed to record a structural MR scan for each subject using the MPRAGE protocol (Mugler and Brookeman 1990). These scans were used to localize the sources of neuronal activity in the brain, which produced the signal recorded at the MEG sensors.

6.3 Participants

Thirty-eight healthy volunteers (employees of Forschungszentrum Jülich GmbH) between the ages of 18 and 40 took part in the study. After discarding seven subjects due to excessive head movements during the measurement (a deviation greater

than 2 cm between the head positions at the beginning and the end of a measurement), 31 subjects remained (17 male and 14 female).

All subjects were right-handed and hand preference was assessed with a German version of the handedness questionnaire (Oldfield 1971). All subjects had normal vision between –1 and +1 diopters or corrected-to-normal vision using Cambridge Research Systems' (Rochester, United Kingdom) MediGlasses for MRI with exchangeable lenses.

Furthermore, the subjects were screened for a history of neurological or psychiatric diseases using the German version of Beck's Depression Inventory (Beck, Steer, and Brown 1996). After fully explaining the experiment, written informed consent was obtained from the subjects.
The study was approved by the ethics committee of RWTH Aachen University Hospital, Germany (EK 225/17).

7 ANALYSIS OF BEHAVIORAL DATA

7.1 INTRODUCTION

Two aspects of the behavioral data are of interest: 1) the exploration behavior, i.e., how the subjects scanned the images during the three tasks and 2) the performance during the search task and the memory task.

Using their senses such as smell, touch, or sight, organisms have the ability to actively examine their environment. This behavior is called active sensing (Uchida and Mainen 2003; Kleinfeld, Ahissar, and Diamond 2006; Land 1999). For this dissertation, only visual exploration in humans is of interest. In a natural environment, humans gather information about their surroundings through a combination of fixations (i.e., focusing their gaze on a fixed location for typically 200 to 400 ms) and ballistic eye movements called saccades (Findlay and Gilchrist 2008). Since only a small part at the center of the visual field is projected onto the foveal region of the retina with highest visual acuity, saccades are necessary to direct the center of attention to different parts of the environment for the purpose of visual inspection.

The analysis of behavioral data might provide valuable evidence regarding the nature of neurological processes taking place during the task. Furthermore, it may provide valuable feedback regarding the validity of the experiment. Several studies have analyzed eye movement statistics (Tatler and Vincent 2008; Nikolaev, Meghanathan, and van Leeuwen 2016; Jo, Kellermann, et al. 2019) and deviations from previous reports may indicate potential problems with the experimental setup (e.g., flaws in the eye tracker calibration). The same is true for the task performance, which was analyzed on a per subject basis, i.e., the number of correctly answered trials was determined for each subject and each task separately. Problems with a task or a specific subject may be identified that way.

7.2 METHODS

7.2.1 EYE MOVEMENT STATISTICS

The EyeLink 1000 system records the eye position with a sampling frequency of 1000 Hz and determines fixation and saccade onsets automatically. The offset of a fixation coincides with the onset of the following saccade and vice versa. Events (fixation and saccade onsets) that happened during the image presentation for one of the three tasks and events that happened during the first fixation cross presentation of each trial were used for analysis. Fixations with a duration greater than one second and saccades with a duration greater than 100 ms were excluded from analysis. Fixation cross events, i.e., events in absence of visual stimuli, were used as a baseline for comparison with events during the image presentation where visual information was actively being gathered and processed. During the search task, the search target is presented before the fixation cross and as such behavior

might have been influenced. Therefore, fixation cross events during the search task were excluded from the analysis.

The distributions of saccade and fixation durations, i.e., the time interval between onset and offset, were computed separately for each task with fixations and saccades pooled across subjects. For FV, this resulted in 19,849 saccades and 19,383 fixations. For VS, this resulted in 10,905 saccades and 10,223 fixations. For ME, this resulted in 20,821 saccades and 20,289 fixations. For the fixation cross this resulted in 4,849 saccades and 4,253 fixations. Analogously, the distribution of saccade directions and how the average distance per saccade depended on the direction was computed for each task. Generally, similar analysis steps were undertaken here as described for the eye-movement analysis in (Jo, Kellermann, et al. 2019). It should be noted that the search task presents a special case since typical search behavior ends once the target object has been found. Due to this break in continuity, only those fixation and saccade events that were performed before the response via button press were included, which explains the lower number of events for VS. The three tasks were tested for differences in saccade and fixation durations using a two-tailed Welch's *t*-test (Welch 1947) with the Bonferroni-correction for multiple comparisons (Bonferroni 1936).

Differences in scanning behavior between the three tasks were analyzed by computing the likelihood of a fixation on an object being followed by another fixation on the same object, by a fixation on a different object, or by a fixation on the background. Naturally, only fixations that were performed during the image presentation were included in the analysis. However, the search task posed an exception once more. Similar to the other analyses, fixations after the response were excluded again for the search task but fixations on the search target were excluded as well, reason being that the subjects might investigate the target with more care compared to the simple scanning behavior. For FV this resulted in 5,528 object fixations, for VS this resulted in 2,313 object fixations and for ME this resulted in 5,820 object fixations. Again, significant differences between the tasks were determined using a two-tailed Welch's *t*-test and the Bonferroni correction for multiple comparisons. It was assumed that the data could be described by a binomial distribution, i.e., the next fixation is on the same object vs. the fixation is not on the same object.

Furthermore, the distribution of saccade directions was investigated and how this distribution changed based on the time elapsed since the image onset. For this purpose, the saccades were vectorized according to a standard cartesian coordinate system with the starting point of the saccades being set to the origin. For each saccade it was checked whether the end point was above or below the origin and it was checked whether the endpoint was to the left or to the right of the origin. For example, saccades with positive *x*- and *y*-components were directed to the right and upwards. The saccades were then grouped within each time bin of 250 ms length across the trial time and two independent fractions were computed for each time bin, the fraction of saccades with positive or negative *y*-component (up- versus downward saccades) and the fraction of saccades with positive or negative *x*-component (right- versus leftward saccades). Data from the three tasks was pooled.

The center of the pupil is one factor used by the EyeLink 1000 system in determining the gaze position. However, since the pupil does not contract or dilate perfectly symmetrically, changes in pupil size may affect the recorded gaze position. Therefore, it is important to contextualize how the saccade direction distribution changed in time with recordings of the pupil size (in arbitrary units). Finally, the Pearson's correlation coefficient (r) was computed between the average pupil size during a fixation and the fixation duration to investigate if there was a connection. For example, Meghanathan and colleagues (2015) found that both increases in pupil size and increases in fixation duration were connected to increased processing load.

7.2.2 TASK PERFORMANCE

Regarding the task performance, the fraction of correctly answered trials was analyzed on a per subject basis. For each memory task trial, the subjects had to localize and subsequently memorize a set of five objects which were embedded in the image. After the image presentation, two objects were presented, and the subjects had to select the one that was present in the previous image. A correct response was given if the button on the side corresponding to the correct target was pressed first (Figure 8). For each search task trial, the subjects had to press a button once they had found the search target. A response was only deemed to be correct if the subject's gaze was on the target object (i.e., within 1.7°of visual angle from the center of the target object) during the interval of ±500 ms around the time of the response.
The average task performances during search and memory were correlated on the subject level using Pearson's correlation coefficient. Furthermore, Pearson's correlation coefficient was used to investigate if subjects with shorter search times (time from image onset to response) were also performing better during the memory task.

7.3 RESULTS

7.3.1 EYE MOVEMENT STATISTICS

Figure 10 shows the probability distribution of fixation durations for the image presentation during the three tasks and the fixation cross presentation. The distributions were relatively similar with the maximum at around 150 ms after fixation onset. The average fixation duration was highest for FV with approximately 228 ± 110 ms followed by the ME with 218 ± 102 ms and the VS with 200 ± 86 ms. The mean values of the three distributions were significantly different ($p < 0.05$) from one another after Bonferroni-correction for multiple comparisons.

The fixations were generally longer for the fixation cross presentation as compared to the image presentation with a higher prevalence for extremely long fixations as shown by the fat tail. The average fixation duration during the fixation cross presentation was 306 ± 215 ms (not shown).

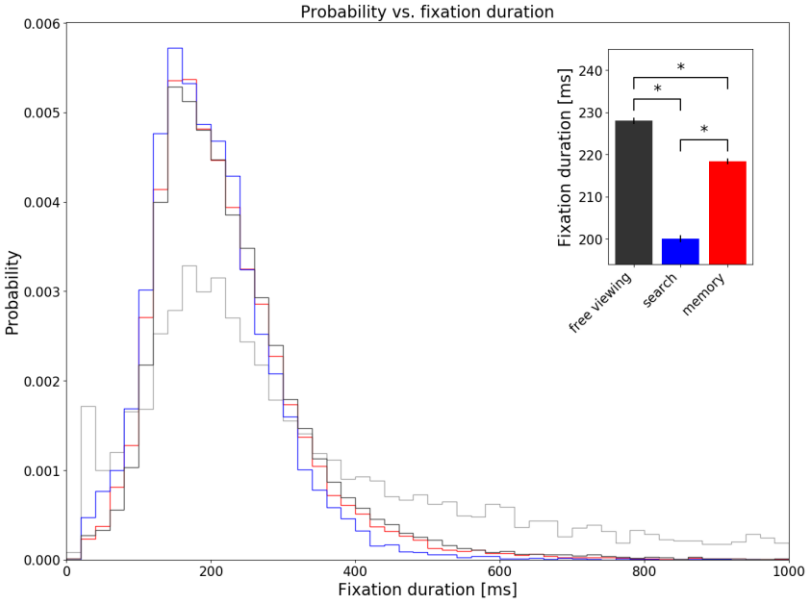

Figure 10: The probability distribution of fixation durations for the image presentation during the three tasks and the fixation cross presentation (light grey). Black, blue, and red lines indicate data from FV, VS, and ME, respectively. In the top right corner is the average fixation duration by task with the small black bars being the standard error of the mean. The asterisk '*' indicates significant differences ($p < 0.05$) in the mean after Bonferroni-correction.

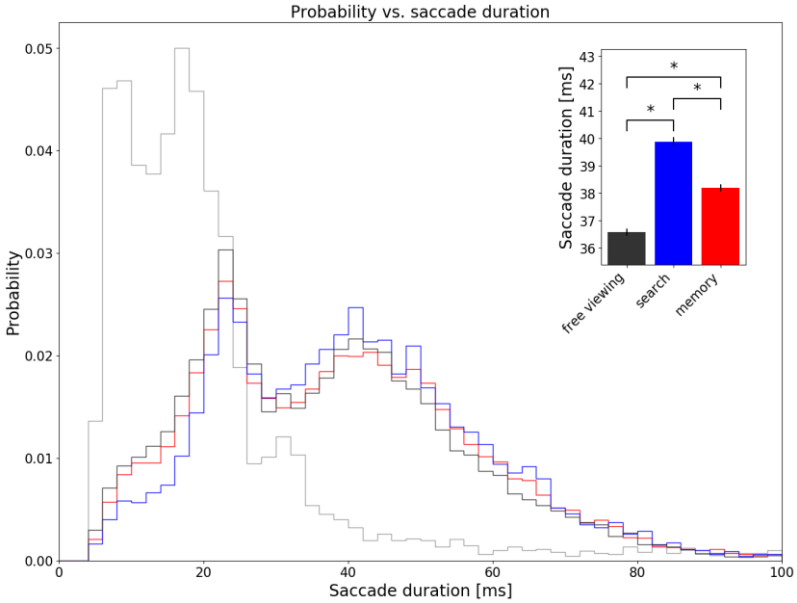

Figure 11: The probability distribution of saccade durations for the image presentation during the three tasks and the fixation cross presentation (light grey). Black, blue, and red lines indicate data from the FV, VS, and ME, respectively. In the top right corner is the average saccade duration by task with the small black bars being the standard error of the mean. The asterisk '*' indicates significant differences ($p < 0.05$) in the mean after Bonferroni-correction.

Figure 11 shows the probability distribution of saccade durations for the three tasks and the fixation cross. Similar to the fixation duration distribution, the shape of the three task-related saccade distributions was very similar. The distributions were bimodal with one peak at around 23 ms and the second peak at 41 ms. The highest average saccade duration was measured for VS with 39.9 ± 17.6 ms followed by ME with 38.2 ± 18.3 ms and FV with 36.6 ± 18.0 ms. The mean values of the three

distributions were significantly different (p < 0.05) from one another after Bonferroni-correction for multiple comparisons.
The saccade duration distribution for the fixation cross presentation also had two peaks, one at 7.5 ms and one at 17.5 ms. the average saccade duration of 19.8 ± 15.0 ms was higher than during the three tasks. Again, the distribution for the fixation cross had a fatter tail than the task-related distributions.

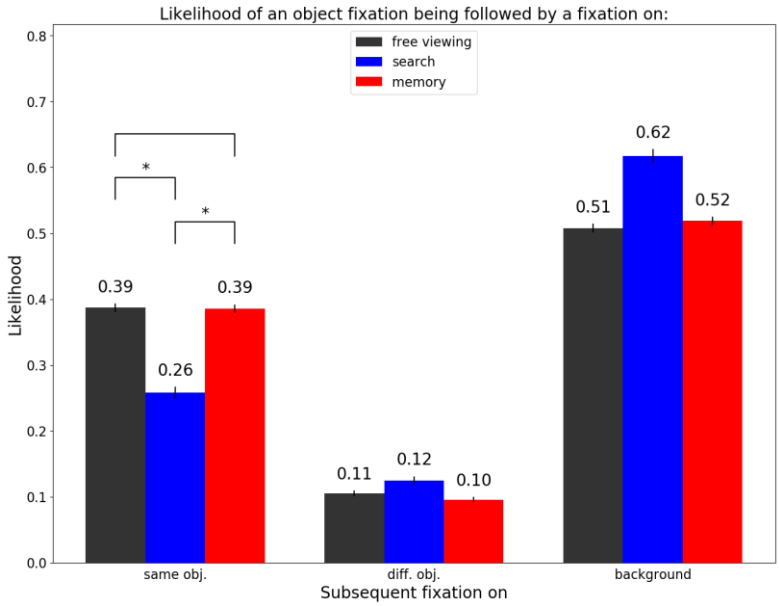

Figure 12: The likelihood of a fixation on an object being followed by a fixation on the same object, by a fixation on a different object, or by a fixation on the background. The error bars represent the standard error of the mean. The asterisk '*' indicates significant differences (p < 0.05) between the tasks after Bonferroni correction.

Figure 12 depicts the likelihood of an object fixation being followed by a fixation on the same object, by a fixation on a different object, or by a fixation on the background. While the likelihoods of fixating on the same object were comparable for FV (0.39 ± 0.49) and ME (0.39 ± 0.49), there was a significant difference (p < 0.05) between ME and VS. During VS, the likelihood of fixating on the same object was only 0.26 ± 0.44.

Figure 13 shows the probability distribution of saccades going in different directions. The distribution was quadrimodal with the peaks corresponding to the four cardinal directions (up, down, left, and right). Saccades in the horizontal directions generally occurred more often than saccades in the vertical directions. It is of note that there was a clear bias with leftward saccades being more common than rightward saccades and also upward saccades being slightly more common than downward saccades. The leftward bias was especially evident for the fixation cross presentation.

Saccade distances (start to end point) were, irrespective of the direction, greatest for VS followed by ME and then FV. Saccades in the horizontal plane travelled, generally, further than saccades in the vertical plane. Saccade distances during the fixation cross were distinctively shorter than the average distances during the tasks (see Appendix Figure 34).

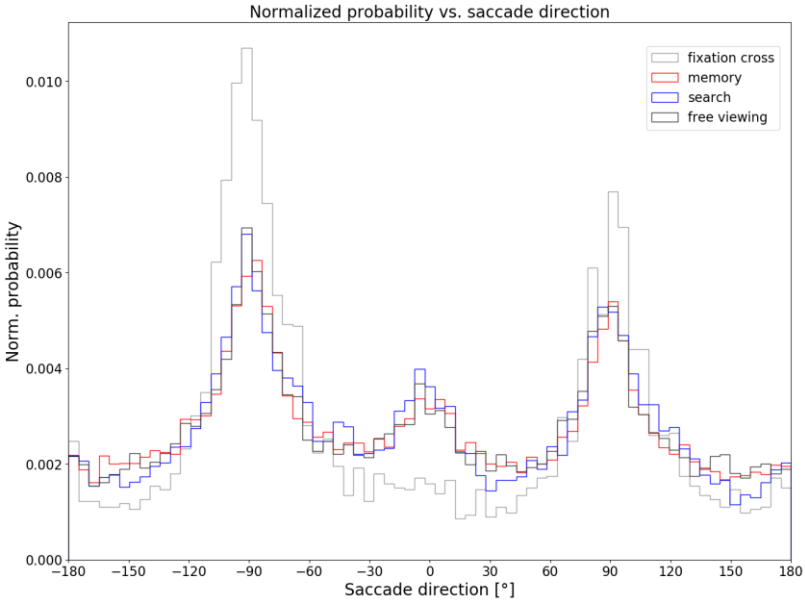

Figure 13: The probability distribution of a saccade going in a specific direction. 0° and ±180° correspond to upwards and downwards saccades, respectively, while -90° corresponds to left- and +90° corresponds to rightward saccades. Black, blue, and red lines indicate data from FV, VS, and ME, respectively. Data from the fixation cross is given in light grey.

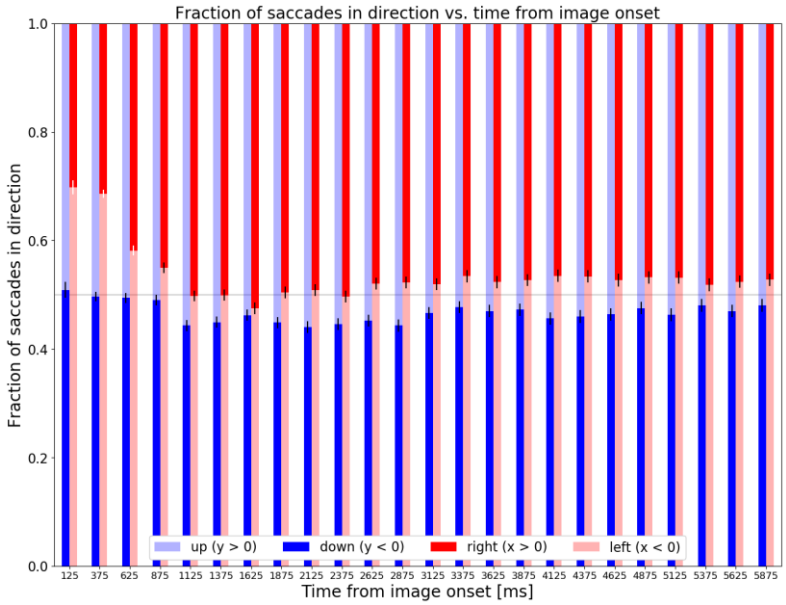

Figure 14: Fraction of saccades in a given direction (up vs. down and left vs. right) dependent on the time from image onset. The error bars represent the standard error of the mean. White error bars indicate a significant deviation ($p = 10^{-7}$) from a binomial distribution with probability $p = 0.5$ after using the Bonferroni-correction.

Figure 14 shows how the fraction of saccades going upwards versus downwards and the fraction of saccades going leftwards versus rightwards depended on the time from the image onset. While, over the course of the image presentation, the probability of an upward versus a downward saccade occurring remained close to 50:50 with odds slightly in favor of upward saccades, the probability of the subjects performing leftward versus rightward saccades was in the first three time bins close to 70:30 only becoming closer to 50:50 after the first 750 ms. The higher proportion of leftward saccades was significant ($p < 10^{-7}$) after correcting for multiple comparisons using the Bonferroni correction. A similar pattern was also found within the first 500 ms for saccade directions during the fixation cross presentation,

however, there was also an additional, significantly higher proportion of downward as compared to upward saccades. (Figure 15).

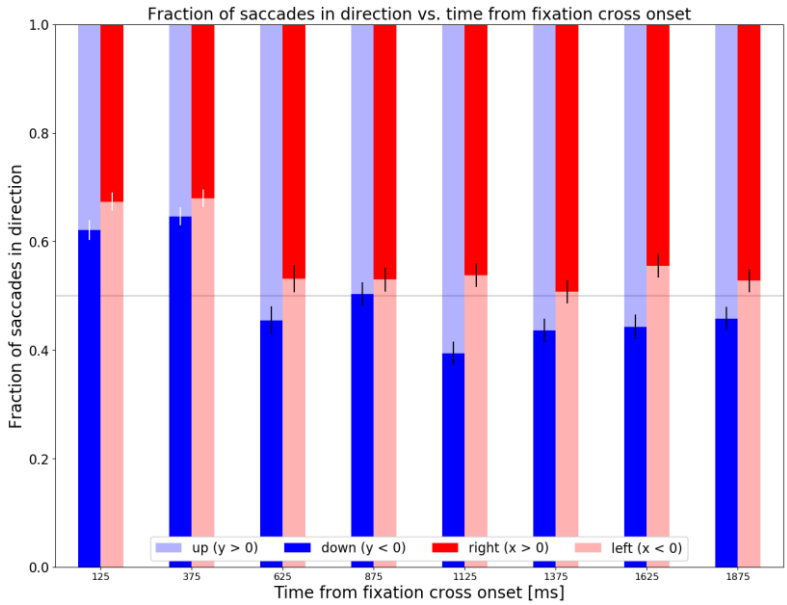

Figure 15: Fraction of saccades in a given direction (up vs. down and left vs. right) dependent on the time from fixation cross onset. The error bars represent the standard error of the mean. White error bars indicate a significant deviation ($p = 10^{-7}$) from a binomial distribution with probability $p = 0.5$ after using the Bonferroni-correction for multiple comparisons.

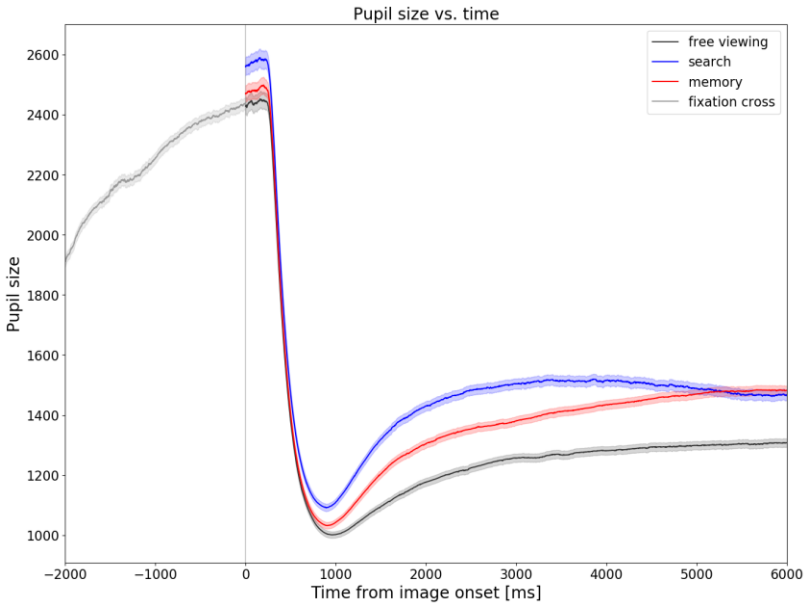

Figure 16: Grand average of pupil size across subjects and trials during the image/fixation cross presentation vs. time from image onset. The shaded area represents the standard error of the mean. Black, blue, and red lines indicate data from FV, VS, and ME, respectively. Data from the fixation cross is given in light grey.

The EyeLink 1000 system records the pupil size (in arbitrary units) during the experiment as it is used to determine the gaze position. Figure 16 shows the grand average across subjects and trials as a function of time elapsed since image onset. The time courses were very similar for the three tasks. The maxima of ~2500 were reached shortly after image onset (~200 ms) followed by a sharp drop-off. The minima were reached after ~900 ms from image onset. Afterwards, the pupil size increased again to a level at around 1300. The average pupil sizes were generally

highest for VS and lowest for FV. The average pupil size during the fixation cross presentation was an exception where the pupil size rose steadily from ~1900 to ~2400.

The fixation duration was correlated with the pupil size during the image presentation. To avoid the extreme changes in pupil size, only the interval from 1.5 to 6 s was considered. After Bonferroni correction, there were weak but significant ($p < 0.05$) negative correlations for all three tasks. For FV, Pearson's correlation coefficient was -0.021, for VS it was -0.062, and for ME it was -0.024.

7.3.2 TASK PERFORMANCE

Figure 17 shows the task performance per subject with the blue and red horizontal lines representing the average task performance across subjects for VS and ME, respectively. During VS, 75.9 ± 9.0% of targets were identified correctly, i.e., a response was given within ±500 ms of fixating within 1.7° visual angle from the center of the target object. Among subjects, the lowest rate of successful search trials was 56.7% while the highest rate of success was 93.3%.
During ME, 63.1 ± 10.4% of targets were identified correctly, i.e., during the 3 s target selection stage of the experiment, the button on the side corresponding to the object that was present in the previous image was pressed. Among subjects, the lowest rate of successful memory trials was 46.7% while the highest rate of success was 80.0%.

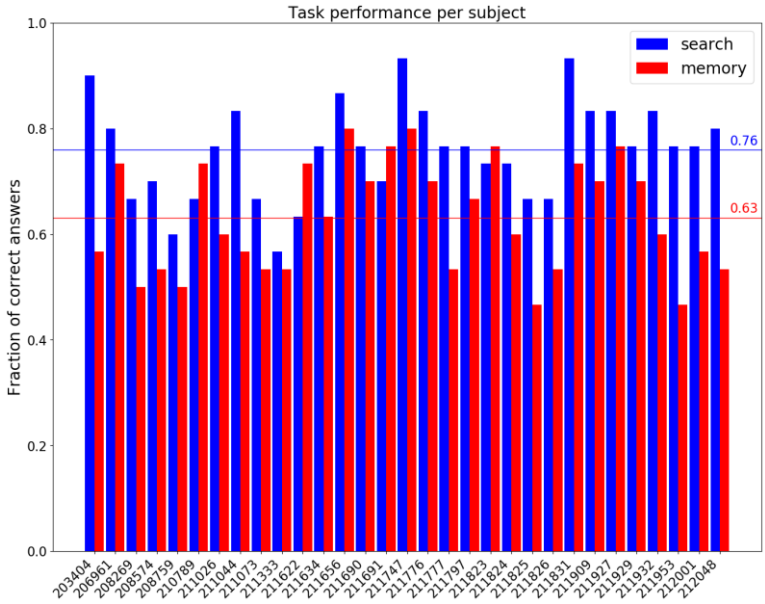

Figure 17: Task performance per subject. The red and blue horizontal lines represent the average task performance across subjects for ME and VS, respectively.

Pearson's correlation coefficient (r) was computed for the task performance during VS and ME. There was a significant relationship ($r = 0.36$, $p < 0.05$) of higher task performance during VS being associated with a higher task performance during ME. Likewise, the average response time (time from image onset to response) during VS was correlated with the average ME task performance. There was also a significant relationship ($r = -0.55$, $p < 0.05$) of shorter search times being associated with better ME task performance.

7.4 DISCUSSION

The behavioral data, i.e., eye movement statistics and task performance, were analyzed with two purposes: 1) behavioral data may reveal information about neurological processes and 2) it provides a sanity-check regarding the data quality. The fixation duration was lowest for VS followed by ME and FV. At the same time the saccade duration was highest for VS, again followed by ME and FV. Furthermore, the likelihood of fixation the same object multiple times in a row was significantly lower for VS as compared to ME and FV. At the beginning of a trial, there was a bias for subjects to perform leftward saccades which vanished over the course of the image presentation. During the same time period, there were drastic changes in pupil dilation. 76 % of VS trials were answered correctly while 63 % of ME trials were answered correctly.

7.4.1 FIXATION AND SACCADE DURATION

The results for saccade and fixation durations presented in Figure 10 and Figure 11 generally replicate previous results reported in (Nikolaev, Meghanathan, and van Leeuwen 2016; Jo, Kellermann, et al. 2019) as described below.

While the general shape of the saccade and fixation duration distributions were similar to what was reported in (Jo, Kellermann, et al. 2019), the reported, average saccade durations ranged from 26 ms for FV to 30 ms for VS, and as such they were considerably lower than the 36 to 40 ms presented here. The most likely explanation for this discrepancy is the difference in visual angle. While Jo *et al.* (2019) presented the stimuli with a visual angle of 25.4 × 16.0°, a visual angle of 32 × 24° was used here.

Fixation durations were shortest for VS. Compared to FV, there is time pressure to solve the task, potentially leading to shorter fixation times. Furthermore, there is a specific search target against which the visual input can be matched. Once it is determined that the search target has not been found, the visual inspection can be terminated, and the next saccade can be initiated immediately. Therefore, the fixation duration during VS should simply reflect the time needed for matching the visual input with the target features. In fact, as Figure 12 shows, the likelihood of fixating the same object twice in a row was significantly lower during VS as compared to ME (and FV), which may also indicate early stopping of visual inspection. It is likely that a combination of both time pressure and early stopping is responsible for the shorter fixation durations during the search task.

On the other hand, saccade durations were on average greatest for VS. An important factor is here that only events that happened prior to the response were included for the search task. It has been well-reported that humans and monkeys use a coarse-to-fine strategy for FV where the saccade duration decreases and the fixation duration increases with viewing time (Unema et al. 2005; Over et al. 2007; Pannasch et al. 2008; Ito et al. 2017). This may explain the greater proportion of long saccades and short fixations for VS as compared to the other tasks (Figure 10 and Figure 11) which has also been reported before (Nikolaev, Meghanathan, and van Leeuwen 2016; Jo, Kellermann, et al. 2019). Furthermore, as per Wolfe's Guided Search 6.0, the saccade destinations follow a priority map where the location with the highest priority for the following saccade can be in any part of the image (Wolfe 2021).

Without such a priority map, saccade destinations closer to the current fixation might be prioritized. Finally, the bimodal shape of the saccade durations (Figure 11) may reflect a switch from the ambient processing mode (coarse) with long saccades to the focal processing (fine) with short saccades over the course of the image presentation (Unema et al. 2005; Over et al. 2007; Pannasch et al. 2008; Ito et al. 2017).

Similar to VS, there is also time pressure during ME. While there is also a search aspect to the memory task (the subjects also have to locate five targets for memorization), there are no guiding features such as color or shape. Furthermore, because the objects were placed in locations where they tended to blend in with the background, it might have taken more time for the subjects to decide if they have actually found an object without the help of guiding features, resulting in longer fixation durations as compared to VS. Due to the process of memorization, longer fixations and/or multiple fixation-saccade-cycles might also be needed for each object. Indeed, the likelihood of fixating an object twice in a row was significantly higher for ME as compared to VS and the fixation duration on objects was also significantly higher during ME (Appendix Figure 33). However, when comparing FV and ME, there was no significant difference between the likelihood of fixating the same objects multiple times in a row, and the fixation duration on objects during FV was significantly higher as compared to ME. Generally, one would expect the amount of time taken to study an object to be highest during ME. Two explanations seem plausible: 1) due to the time pressure imposed by the need to identify all five targets during ME, the fixation durations are limited to the bare minimum necessary for memorization and 2) despite it not being required by the task, the subjects memorized features of the objects during FV as well leading to longer fixation durations.
Finally, another aspect leading to longer fixation durations and shorter saccade durations during ME as compared to VS could be that the priority map is potentially not as clear cut as in the case of the search task so that more time is required to decide the next saccade destination and closer destinations might become prioritized due to the lack of guiding features.

7.4.2 SACCADE DIRECTION AND AMPLITUDE

The prevalence of horizontal over vertical saccades reported in earlier studies (Tatler and Vincent 2008; Nikolaev, Meghanathan, and van Leeuwen 2016; Jo, Kellermann, et al. 2019) was confirmed by the results in this dissertation (Figure 13). Additionally, Figure 34 shows that saccades in the horizontal plane are not only more prevalent but they are also of larger amplitude. A likely explanation for this phenomenon is that the aspect ratio of the images was greater along the horizontal axis (Tatler and Vincent 2008).

A different pattern could be observed when comparing saccades along the same axis but in opposite directions. For example, upward saccades occurred more often than downward saccades, but their amplitude was on average also smaller than that of downward saccades. A similar effect could also be observed in previous studies (Tatler and Vincent 2008; Jo, Kellermann, et al. 2019). However, the same was also true for leftward saccades which occurred more often than rightward saccades with

on average smaller amplitudes. This leftward bias in saccade prevalence was particularly noticeable for the presentation of the fixation cross. A similar bias was not observed in the studies mentioned earlier.

Since the same experimental paradigm was used in this dissertation as in the studies by Jo and colleagues (2019a, 2019b), their results are the most likely ones to be directly comparable to what was presented here (Jo, Ito, et al. 2019; Jo, Kellermann, et al. 2019). Jo and colleagues (2019b) did not report a bias in either direction in the horizontal plane for the three tasks, however, there was a slight bias in favor of upward eye movements (see Fig. 1D in (Jo, Kellermann, et al. 2019)[16]). Only for the fixation cross, there seemed to be a slightly higher prevalence of leftward over rightward eye movements (Jo, Kellermann, et al. 2019). Because leftward eye movements were split into two halves right at the border of Fig. 1D in (Jo, Kellermann, et al. 2019), it is possible that this was not noticed, especially since there was no particular horizontal bias for data from the three task conditions.

This leftward bias could potentially be an artifact since it has not been observed before in the literature. That different properties in the stimuli (e.g., differences in salience or in object density) could result in such a bias is not likely since the same stimuli were used in (Jo, Kellermann, et al. 2019).

Figure 14 and Figure 15 indicate that this bias only manifested clearly in the early time interval up to 750 ms from image onset and up to 500 ms from fixation cross onset. For the major part of the image presentation period, the chance of a leftward vs. a rightward saccade was relatively even. Therefore, it is unlikely that there was a systematic bias in the setup of the eye tracking system. However, changes in pupil size are known to affect the accuracy of eye tracking recordings (Nyström, Hooge, and Andersson 2016) and Figure 16 confirms that it was right in that early time interval up to one second after image onset that the average pupil size decreased drastically due to the change from the preceding fixation cross with black background to the presentation of the much brighter image. Yet, Figure 16 also contradicts this hypothesis that the leftward bias is a result of a decreasing pupil size. Instead of decreasing, the average pupil size increased steadily with time from fixation cross onset and the strongest leftward bias could be observed for data during the fixation cross presentation.

Another explanation for the leftward bias might be trained reading behavior influencing how subjects scan images for information. In the western world, the reading direction is generally starting at the first line in the top left corner and then following the text from left to right, line by line. This might lead to the subjects being biased to start scanning the images for information from the left. For example, if there are two salient stimuli, one on the left and one on the right side of the image, the subjects might be biased to first look towards the left. At later points, saccades might depend more on the properties of the image and on the task goals when viewing the image. This hypothesis could be easily tested by presenting competing

[16] Be aware that the definition of the saccade angles that was used here in Figure 13 differs from that used in (Jo, Kellermann, et al. 2019).

stimuli in each hemifield and by recruiting subjects from different cultures where the reading direction differs.
But this behavior would not directly explain the bias observed during the fixation cross presentation. However, after reading the task instruction, which is presented just before the fixation cross, the gaze position might end up at the right from the center of the screen and thus, to fixate the fixation cross, a leftward saccade might be required.

When designing eye tracking studies in the future, one should ensure that the average luminance/ brightness remains constant over the course of the experiment. So instead of the commonly used black background, one should use a grey background whose illuminance matches that of the image stimuli. Only adjusting the brightness during calibration to match the brightness during the image presentation, as it was done here, does not suffice as there are obvious effects of pupil size adjustments during the first second of image presentation (Figure 16). Furthermore, a constant level of illumination might help with eye fatigue during the experiment since large adjustments in pupil size will be minimized.

In Figure 16, the time courses of the pupil size resembled that of an underdamped harmonic oscillator for the three tasks with a sharp decrease resulting in a minimum followed by a period of relaxation. The initial pupil size during VS started at a higher level than during the other two task conditions. One possible explanation is that during VS, there was the additional presentation of the search target for three seconds, giving the eye more time to adjust to the lower light conditions due to the black background.
Furthermore, a weak, negative correlation between the average pupil size during a fixation and the fixation duration was found for the time interval from 1.5–6 s from image onset. This is in line with the average fixation duration during the three tasks (Figure 10) and the average pupil size (Figure 16). A possible explanation could be that the pupils dilate to let more light reach the fovea to counteract the shorter fixation times during which information is gathered. This might also serve as an explanation why the average pupil size during VS fell below the average pupil size during the memory task over the course of the image presentation. Once the search target was found, the need for a short saccade-fixation cycle disappears. Meghanathan and colleagues (2015) found the fixation duration to be connected with both memory load and processing load while the pupil size was only connected with processing load in a multiple-targets visual search task (which was more akin to the memory task presented in this dissertation) (Meghanathan, van Leeuwen, and Nikolaev 2015). However, this common dependence of both pupil size and fixation duration on the processing load would lead to a positive correlation. Therefore, the negative correlation that was observed could potentially have been weakened, particularly during the memory task due to the increased processing load compared to the other tasks.

7.4.3 TASK PERFORMANCE

The lower number of correctly answered trials for ME as compared to VS reflects the higher difficulty of the memory task. The search is guided by the target object presented before the image and only this one target has to be located. Despite the

lack of feedback during the experiment, the subjects can be reasonably sure whether they have found the correct target during VS. Furthermore, even though there are other objects embedded in the image, they are not relevant for a successful trial and can be ignored. During ME, however, the subjects have to locate all five objects embedded in the image without *a priori* knowledge about them. Therefore, the likelihood of not locating the correct target is higher during ME. Moreover, even if the subjects locate a correct object, it is possible that they fail to memorize it for the subsequent prompt after the image presentation.
The fact that a better VS task performance was associated with a better ME task performance could reflect that the memory task also involved an aspect of searching. For example, if a subject's search strategy is more efficient, the likelihood of localizing all objects during the memory task increases, which is a vital factor in ME task performance. This would also be supported by the results of the correlation analysis where shorter response times during VS were associated with better ME task performance.
Finally, the good performance during VS was also an indicator of adequate eye tracking data quality since, for a correct response, it was required that the subjects looked at the target objects at the time of the response. Approximately 1 % of trials were considered a failure due to the subject not fixating on the target while giving the response.

7.5 Conclusion

Eye movement statistics reported in previous studies were generally replicated here. Therefore, it is reasonable to assume that there were no critical flaws inherent to the setup. However, the higher proportion of leftward saccades during the first 750 ms of the image presentation had not been reported in any other studies. One explanation could be trained reading behavior that led to the left hemifield being explored first. Another potential explanation is that the pupils contracted due to the increased illumination during the image presentation, which led to a bias in the tracking of the gaze position. For future studies, it is recommended to avoid abrupt changes in brightness during the presentation. Ideally, the brightness would always remain the same during the presentation, irrespective of whether the eye tracker is being calibrated, the fixation cross is being shown, or an image is being presented.
Differences in the saccade and fixation durations between the three tasks could potentially be explained by the time pressure and the difficulty of the task, i.e., it is easier to locate a known target object during VS as compared to an unknown target object during ME. Furthermore, the higher proportion of long saccades during VS could indicate that searching relies more strongly on an ambient focus strategy (coarse scanning of the image).
The task performance was on acceptable levels for all subjects and the data was consistent with itself, e.g., faster search speeds were correlated with a higher performance during ME where the subjects had to find and memorize five objects, all within the duration of the image presentation.
In summary, the quality of the recorded data was high, and it presents a good basis for more complex analyses (cf. sections 8.2.2.2 and 8.2.3.2).

8 THE WHOLE-BRAIN CAUSALITY NETWORK DURING GUIDED VISUAL SEARCHING AND FREE VIEWING[17]

8.1 INTRODUCTION

Attentional selection during visual processing is generally said to be governed by two types of competing mechanisms: bottom-up and top-down processing (Delorme et al. 2004; Sobel et al. 2007; Theeuwes 2010). Bottom-up processing refers to the case where salient properties of the stimuli automatically and involuntarily capture the attention while, during top-down processing, attentional selection is under control of the observer (Sobel et al. 2007). Top-down processes can draw on prior knowledge to guide attention to objects most likely to help accomplish the observer's goals (Sobel et al. 2007).

For this dissertation, the experimental paradigm from Jo *et al.* (2019a, 2019b) was adopted to examine how the goal-directed behavior (including top-down processing) during guided visual searching affects the whole-brain information flow as compared to the free viewing of natural scene images. For the memory task, it is more difficult to disentangle top-down and bottom-up components. While there is goal-directed behavior due to the task, the exploration itself is likely driven by bottom-up processing since there is no information available about the target. Therefore, data from the memory task was only used in chapter 9. The analysis was based on the fixation-related evoked field (FRF), which was recorded using MEG. Following MEG best practices, the FRF sensor data was projected onto the source space, yielding the fixation-related evoked activity (FRA). The analysis of FRA data consisted of three major steps. First, spatiotemporal cluster permutation testing (SCPT) was used to identify regions of interest (ROIs) with significant FRA. Second, the search response time was correlated with the activity in these ROIs. Finally, generalized partial directed coherence (GPDC) was used to estimate the whole-brain causal interaction networks between these ROIs based on single-epoch FRA data.
The hypothesis was that the specification of the search target during the guided visual search would lead to additional top-down processes, thus altering the structure of whole-brain connectivity networks. First and foremost, the key difference between freely viewing naturalistic images and searching them would be

[17] Partial results of the presented work have been published at Frontiers in Neuroscience (Kiefer et al. 2022) where I was responsible for the development and the design of the methodology. Furthermore, I performed the formal analysis, and I wrote the original draft of the manuscript. I was supported by Frank Boers in the setup of the experiment and in the development of the software for conducting the experiment. Junji Ito assisted in the formal analysis, and he reviewed and edited the manuscript. Ralph Weidner also reviewed and edited the manuscript. N. Jon Shah provided resources for conducting the experiment and he reviewed and edited the manuscript. Sonja Grün and Jürgen Dammers conceptualized the experiment, devised the methodology, acquired funding, and edited and reviewed the manuscript. Furthermore, Jürgen Dammers was responsible for the project administration and supervision.

that the visual input has to be matched with a mental representation of the search target to determine whether the target has been found (Wolfe 2021). Moreover, if the search target was not present at the searched location, attention has to be shifted to the next location (Theeuwes 2014; Wolfe 2021). In contrast to free viewing, where attention shifts are most likely driven by bottom-up salience (Berger et al. 2012; Wolfe 2014), attention shifts during the search task are guided by a priority map ranking potential search locations by the likelihood of containing the target (Theeuwes 2014; Wolfe 2021). This priority map is continuously updated with new information over the course of the search. The (right) temporoparietal junction—the border region between the supramarginal gyrus and the superior temporal gyrus—has been identified in the context of target detection (Linden et al. 1999; Shulman et al. 2010) and shifting attention to new, behaviorally relevant stimuli (Shulman et al. 2007; Corbetta, Patel, and Shulman 2008). Following a fixation, the visual input has to be examined for the presence of the search target and, in case it is not present, a saccade to a new potential target location has to be initialized. Therefore, the temporoparietal junction is expected to be a central node in the FRA causality network for VS.

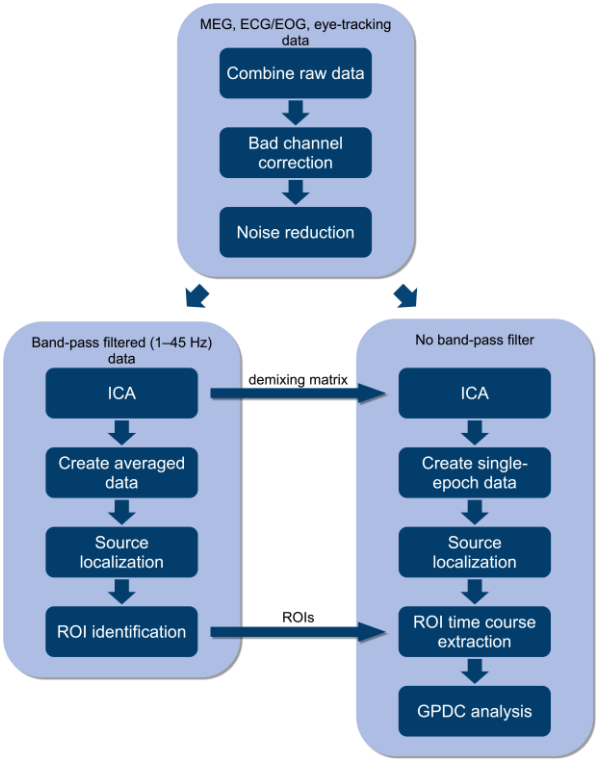

Figure 18: Analysis pipeline diverges into two separate branches—one based on band-pass filtered data (1–45 Hz) and one based on single-epoch data without band-pass filter.

Two sets of ROI clusters were identified per hemisphere—in each case one cluster in the temporoparietal cortex and one in the dorsal cortex. These clusters displayed significant activity during both guided visual searching and free viewing. The temporoparietal cluster comprised parts of the supramarginal gyrus, the superior temporal cortex, the transverse temporal gyri, and the posterior insula. According to the results of the Granger causality analysis, these four regions formed a highly inter-connected network. One part of the temporoparietal junction, the right supramarginal gyrus, stood out during visual searching due to a particularly high number of interactions with other ROIs. Moreover, during visual searching, stronger

activity in the right supramarginal gyrus was correlated with shorter response times. All in all, the results imply that, during guided visual searching, the right supramarginal gyrus functions as a hub for information exchange.

8.2 METHODS

Data analysis was performed using Python 3.6 with MNE python v0.19 being the main package (Gramfort et al. 2013).
Since several studies have reported that filtering can negatively affect the results of Granger causality analyses (Florin et al. 2010; Barnett and Seth 2011), whereas other processing steps such as computing the independent component analysis (ICA) demixing matrices are best performed with filtered data (Winkler et al. 2015), the analysis pipeline was split into two separate branches after the first couple of preprocessing steps (Figure 18). Band-pass filtered data from 1 to 45 Hz was used to train the ICA demixing matrices and to identify ROIs with significant FRA, while the GPDC analysis was performed on unfiltered[18] single-epoch data.

8.2.1 PREPROCESSING

8.2.1.1 COMBINING MEG DATA, ECG/EOG DATA AND EYE TRACKING DATA

Data from three different sources, MEG, ECG/EOG, and the eye tracker, was recorded simultaneously at different sampling rates. After the recording session, these three datasets had to be time-aligned and combined into a single dataset.
First, the MEG data was combined with the ECG/EOG data. Since the ECG/EOG data was recorded at a sampling frequency of 5000 Hz, the data had to be resampled to the sampling frequency of the MEG system (1017.25 Hz) first. The second step was to combine the MEG data with the eye-tracking data. Common event codes, e.g., image onset as given by the image onset device or pressed buttons, recorded in the response channel of the MEG system and in the output of the EyeLink 1000 system were used to determine corresponding time points. The alignment was done for each trial separately. Due to the higher sampling rate of the MEG system (1017.25 Hz) compared to the eye-tracking system (1000 Hz), the eye-tracking data was interpolated linearly to achieve the same virtual sampling rate as the MEG system. In Appendix section 11.3.1, the alignment of the recordings was tested.

8.2.1.2 BAD CHANNEL IDENTIFICATION AND INTERPOLATION

The next preprocessing step was the identification and subsequent interpolation of channels showing unexpected, strong noise or artifacts such as jumps in the signals. An in-house machine learning algorithm based on density-based spatial clustering of applications with noise (DBSCAN) was used to identify such bad channels (Ester et al. 1996). After manual inspection, the suggested channels were replaced by virtual channels using interpolated data from their neighbors (Perrin et al. 1989; Gramfort et al. 2013, 2014).

[18] Unfiltered apart from the 50 and 60 Hz notch filters described in section 8.2.1.3.

8.2.1.3 NOISE REDUCTION

The strength of the magnetic dipole field decreases rapidly with $1/r^3$ (Fagaly 2006). Since the reference detection coils are far away from the signal sources in the brain relative to the signal detection coils, the amount of brain signal is negligible in the reference channels. However, distances to environmental and external noise sources tend to be of the same order of magnitude for both signal and reference detection coils. Hence, substantial amounts of environmental and external noise can be removed from the signal channels by subtracting the reference channels from the signal data (Robinson 1989).
Apart from external noise, the biggest noise contributor is power line noise at 50 Hz and its harmonics in Germany. The noise components are usually clearly visible in the power spectral densities (Appendix Figure 39, left). Projector noise (60 Hz and its harmonics) may also play a role to a lesser degree. Using a notch filter for 50 Hz plus harmonics and 60 Hz plus harmonics, the majority of power line noise and projector noise can be removed. However, this can have quite drastic effects on the data. Instead, an anti-notch filter was applied to the reference channels of the MEG system so that only the power line contribution remained in the reference signal. By subtracting the filtered and weighted reference signal from the signal channels, noise was be reduced (Appendix Figure 39, right).

8.2.2 IDENTIFICATION OF REGIONS OF INTEREST

This section describes the analysis steps depicted in the lower left-hand corner of Figure 18, which were based on band-pass filtered data (1–45 Hz).

8.2.2.1 INDEPENDENT COMPONENT ANALYSIS

Components containing significant contributions of ocular or cardiac activity were removed using independent component analysis (ICA) (Hyvärinen and Oja 2000). The reliability of signal separation with respect to ocular and cardiac artifacts can be increased by training the ICA demixing matrix on filtered data. Therefore, the full recordings were band-pass filtered between 1 and 45 Hz. To improve the stationarity of the data, which could be impacted, e.g., by drift or movements of the subject, ICA was performed on smaller data segments of approximately 100 s length (~100,000 samples). An ideal time point to cut the data into segments was the middle of the eye tracker calibration since these data segments were not relevant for analysis. In this way any discontinuities during relevant times could be avoided. To identify ICA components with strong contributions of ocular or cardiac activity, Pearson's correlation coefficient with the ECG and EOG reference channels was computed. If Pearson's r was greater than 0.3 the component was removed. Additionally, cross-trial phase statistics (CTPS) was employed to identify components with cardiac activity (Dammers et al. 2008).

Channel 7 of Forschungszentrum Jülich's MEG system was found to introduce a noise artifact in surrounding channels. This artifact was highly correlated in time across different channels and as such may impact connectivity analyses negatively. Therefore, a second ICA demixing matrix was trained on the channels surrounding channel 7 up to its third nearest neighbors. The ICA components were inspected manually for components with strong artifact contributions which were then removed.

8.2.2.2 CREATING AVERAGED DATA

The EyeLink 1000 system automatically detects fixation (and saccade) onsets. With this information, fixation onsets during the image presentation were identified for each recording run. These time points were then used to create FRF epochs for the two conditions (VS and FV) where time 0 corresponded to the fixation onset. However, for VS all events after having given response were ignored. For a given combination of recording run and condition, the epochs were averaged around fixation onset and the time interval between –200 and 0 ms from fixation onset was used as a baseline. The mean of the sensor time courses was calculated for that interval and subtracted from the entire epoch on a per sensor basis. Then, the standard deviation across all channels was computed for the baseline interval and the sensor time courses from the entire epoch were divided by this standard deviation. In this way, the data is z-scored with respect to the baseline interval, but the relative amplitudes of the channels are conserved.
Averaged fixation onset data for fixations during the presentation of the fixation cross were extracted in a similar fashion.

8.2.2.3 SOURCE LOCALIZATION

FreeSurfer was used to obtain surface source spaces from the individual anatomical brain scans (Dale, Fischl, and Sereno 1999; Fischl et al. 1999). Source time courses were computed by projecting the averaged FRF data onto the source space using dSPM and taking the norm of the source orientations (Gramfort et al. 2013). These source time courses represent the absolute FRA for each vertex.
Since no two brains are identical, the grid points, based on which the time courses are computed, vary from subject to subject and as such the data objects with the source time courses are not directly comparable. Hence, the source time courses were all morphed to FreeSurfer's 'FsAverage' template brain as a common source space. The 'FsAverage' source space consisted of 5124 vertices with an average vertex-to-vertex distance of 6.2 mm.

8.2.2.4 IDENTIFICATION OF REGIONS OF INTEREST

To identify regions of interest (ROIs) with significant activity across all subjects, SCPT with a pairwise independent *t*-test was performed on the first 200 ms after fixation onset (Maris and Oostenveld 2007).

For each task condition a separate set of ROIs was computed based on a contrast between the FRA during the task and the FRA during the presentation of the fixation cross. The goal was to isolate activity related to processing the actual visual information by reducing activity related to the physical eye movements. For the same reason, only one-tailed tests were performed.

Setting an appropriate threshold can be an important step in the application of SCPT. Generally, the threshold can be set to any value without affecting the validity of the cluster test statistics (chapter 3), but, the shape of the clusters may vary drastically (Maris and Oostenveld 2007). If the threshold is too small, one might simply end up with two big clusters, one for the entire left and one for the entire right hemisphere. On the other hand, if the threshold is set too high, no clusters might survive at all.

A common approach to deal with this problem is to make the assumption that the two conditions have similar time courses and that distribution of the difference of these time courses should approach a normal distribution. Then one could simply use, for example, the *t*-value corresponding to the 95th percentile as the threshold value.
This was not feasible here because the amplitude of the data for fixation onsets during the image presentation was of a higher magnitude than that of the data for fixation onsets during the fixation cross presentation (see Appendix Figure 40 and Figure 41). Thus, it could not be assumed that the distribution of the differences approached a normal distribution.

To estimate a sensible threshold, the contrasts of the averaged time courses were z-scored with respect to the baseline interval on a per subject and recording run basis. For 31 subjects and three runs each, this resulted in 93 z-scored contrasts. For each of these contrasts the value corresponding to the 97.5th percentile was determined and then the average was taken to obtain the threshold for this pair of events. The goal of using a very high threshold like the 97.5th percentile was to focus on the strongest activity only.

The SCPTs were performed with 30,000 permutations for each task condition. Only significant clusters ($p < 0.05$) with a minimum size of 5 vertices (about 1.95 cm^2) and a temporal extent of ≥20 ms were included for further analysis. Afterwards, all vertices belonging to at least one significant cluster were collected and partitioned into ROIs based on the anatomical labels as defined by the Desikan-Killiany atlas (Desikan et al. 2006). If the number of vertices in a given ROI (i.e., in an anatomical label after parcellation) was less than 15% of the total number of vertices in the anatomical label, then the ROI was excluded from analysis.

8.2.3 Generalized partial directed coherence on single-epoch data

This section describes the analysis steps depicted in the lower right-hand corner of Figure 18, which were based on—apart from the notch filters—unfiltered data.

8.2.3.1 Independent component analysis

The same steps as in section 8.2.2.1 were performed on the unfiltered data to remove ocular and cardiac artifacts as well as the artifact introduced by MEG channel 7. However, instead of training separate ICA demixing matrices on the unfiltered data, the same demixing matrices that were trained previously on the filtered data were used on the unfiltered data. Thereby, the quality of artifact removal could be improved without having to filter the data itself (Winkler et al. 2015).

8.2.3.2 Creation of single-trial data

Similar to section 8.2.2.2, the eye tracking data was used to create epochs for fixation onset during the three task conditions while the image was being presented with time 0 corresponding to the onset. Events that happened after the response was given were again excluded for the search task. For the single-epoch data, however, the time interval between -400 and 0 ms before fixation onset was used as a baseline for z-scoring.

8.2.3.3 SOURCE LOCALIZATION

In general, the same steps as in section 8.2.2.3 were performed for the unfiltered single-epoch data used in the GPDC analysis. However, instead of taking the norm of the dSPM activity, the source activity was projected onto the vector normal to the cortical surface (Gramfort et al. 2013).

8.2.3.4 EXTRACTION OF ROI TIME COURSES

Given an epoch, for each ROI identified in section 8.2.2 a representative time course is computed by averaging the time courses of all vertices within a distance of 12.4 mm (twice the average vertex-to-vertex distance) of the maximum activity in the ROI. These time courses were then called the ROI time courses.

The vertex with maximum activity was determined by averaging all source time courses across epochs for each participant. After taking the absolute value, the vertex with the on average largest amplitude during the main activity (50 to 180 ms from fixation onset) across participants was identified.

Before computing the ROI time courses by averaging the vertex time courses it is required to flip the sign of some of these time courses to avoid signal cancellation. This is due projecting the source activity onto the vector normal to the cortical surface. If the direction of the underlying current is the same for two vertices at opposing sides of a sulcus, the sign of the time courses is likely to be the opposite and the time courses would cancel each other out when averaging. The vertices whose time courses had to be flipped were determined using the Pearson correlation coefficient. After averaging the vertex time courses across epochs, the time course of the vertex with maximum activity was correlated with those of the other surrounding vertices. For all vertices with a negative correlation coefficient, the sign of the time courses was flipped.

8.2.3.5 ANALYSIS OF GENERALIZED PARTIAL DIRECTED COHERENCE

The Source Connectivity Toolbox (SCoT) was used to perform the MVAR analysis and the subsequent GPDC causality analysis (Billinger, Brunner, and Müller-Putz 2014). The MVAR models were estimated separately for each subject and condition based on the first 300 ms from fixation onset of the single-epoch ROI time courses. SCoT estimates the MVAR model parameters by casting the models in the form of ordinary regression models and determining the regression model parameters with least squares estimation (see section 4.2.3) (Neumaier and Schneider 2001; Billinger, Brunner, and Müller-Putz 2014).
Since only events that occurred prior to the subject's response were included in the analysis of the search task, the number of fixations was lower during VS than during FV. Therefore, a threshold was set for the maximum number of epochs to be used to ensure comparable SNRs during all conditions. The threshold was the minimum number of epochs found across subjects and conditions plus 10%. Then, if the number of epochs for one subject and condition exceeded the threshold by, for example, 100%, every second epoch was excluded from analysis.

8.2.3.5.1 Considerations for the estimation of multivariate autoregressive models

As mentioned earlier in section 4.2.1, stationarity of the time series is an important prerequisite for the validity of the fitted autoregressive models. The single-epoch ROI time courses were tested for stationarity using the ADF and the KPSS tests (W. H. Greene 2003; Kwiatkowski et al. 1992; Seabold and Perktold 2010). According to these two tests, the data could not be considered stationary. Since the Engle-Granger two step method with critical values provided by James MacKinnon (2010) did not provide evidence for the presence of cointegration ($p < 0.05$) (Engle and Granger 1987; MacKinnon 2010), the time courses were first-differenced which resulted in weakly stationary time series ($p < 0.05$).

Using the HQIC, the optimal MVAR model orders for the differenced time courses were estimated to be 42 for all combinations of subjects and tasks. The resulting MVAR models represented stable (i.e., stationary) processes according to SCoT, and using the LMLP test it was confirmed that the residuals could be considered white. The fitted MVAR models captured approximately 76% of the correlation structure in the data according to the consistency test.

8.2.3.5.2 Computing generalized partial directed coherence

Based on the MVAR models, causal interactions were estimated on the subject level using GPDC. The GPDC value for a given frequency band was computed by averaging the GPDC results across the frequency bins within that specific band, e.g., $\mathrm{GPDC}_{\delta,mn} = \frac{1}{4}\sum_{f=1}^{4} \mathrm{GPDC}_{mn}(f)$. The frequency bands were defined as delta (1–4 Hz), theta (4–8 Hz), alpha (8–13 Hz), beta1 (13–20 Hz), beta2 (20–30 Hz), and gamma (30–40 Hz).

8.2.3.5.3 Statistical analysis

To identify which of the causal interactions were significant on the subject level, surrogate data was computed for each subject where the phase information of the ROI time courses had been destroyed by shuffling the data along the time axis. As a result, any causal interactions between the ROIs should have been destroyed as well. An MVAR model was computed for each surrogate using the same model order as for the recorded data and GPDC was estimated. This procedure was repeated 1,000 times per subject and in each frequency bin, the maximum GPDC value was determined. Similar to section 8.2.3.5.2, the significance threshold for a frequency band was computed by averaging the maximum GPDC values across the respective frequency bins. All interactions where the connection strength was below the threshold were set to zero.

Significant causal interactions were assumed to be present on the group level if a specific connection appeared with significant strength in at least 24 out of 31 subjects, which corresponds to the upper critical alpha level of 0.1% for a binomial distribution with $N = 31$ and probability $p = 0.5$. The final group-level result for a task was computed as the average value of the connection strengths across all subjects.

The causality matrices were not directly comparable between tasks since each task had their own separate set of ROIs. Therefore, the causality matrices were expanded

to include all ROIs that were significant during any of the two tasks with newly created entries being set to zero. Results could then be compared by simply subtracting the expanded causality matrices from one another.

8.2.4 Correlation analysis between ROI FRA amplitude and search response time

In order to identify ROIs where activity was associated with processing visual information related to the search target, the first fixation on the search target was identified for each trial. Then the FRA amplitudes for these fixations were correlated trial by trial with the search response times using Pearson's correlation coefficient (r). The analysis was based on band-pass filtered (1–45 Hz) single-trial FRA time courses.

The correlation coefficients were computed as follows. First, trials with incorrect responses were discarded from the analysis. For a response to be considered correct, the subjects had to fixate within 1.7° of visual angle from the center of the target objects when giving the response (with a margin of error of ±500 ms). Furthermore, trials where the response time exceeded one second were discarded as well. Then, based on the grand average of the FRA time courses over trials and subjects, the full-width-at-half-maximum (FWHM) intervals were determined for each ROI. For a given trial, the FRA amplitudes were computed as the average, absolute activity during the FWHM intervals and the search response times were computed as the time from the onset of the first fixation on the search target until the response via button press. Finally, Person's correlation coefficient was computed between the FRA amplitude of each ROI and the response time. Multiple comparisons were accounted for using the false discovery rate (FDR) correction (Benjamini and Hochberg 1995).

8.3 Results

8.3.1 Identification of regions of interest

Contrasts of FRA activity (image presentation vs. fixation cross presentation) were used with SCPT to identify ROIs with significant activity attributable to visual processing (see section 8.2.2.4 for details). Subsequent Granger causality and correlation analyses were based on data extracted from these ROIs.

The results were generally very similar across cognitive tasks, and the spatiotemporal clusters were strongly symmetric across hemispheres. Regions with significant FRA are listed in Table 1 together with the Montreal Neurological Institute (MNI) coordinates of the vertices with maximum activity.

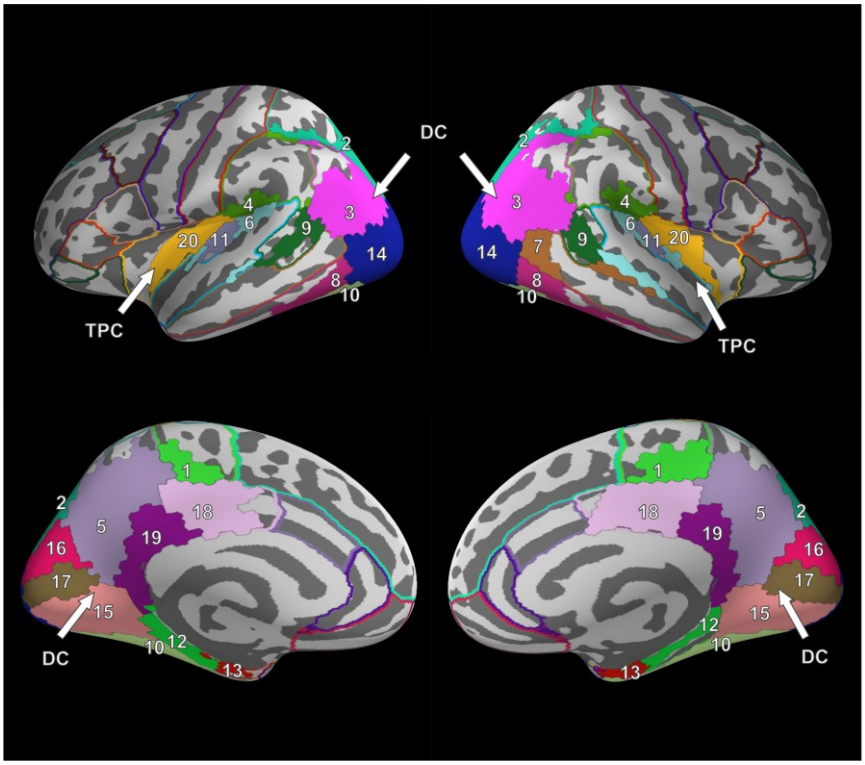

Figure 19: FV cluster results for the contrast of FRA during the image presentation versus FRA during the fixation cross presentation (DC: dorsal cluster, TPC: temporoparietal cluster). Separate ROIs are highlighted in different colors according to the Desikan-Killiany atlas (Desikan et al. 2006). Table 1 lists the ROIs corresponding to the numbers. Figure reprinted from (Kiefer et al. 2022). Copyright 2022 by Kiefer et al.

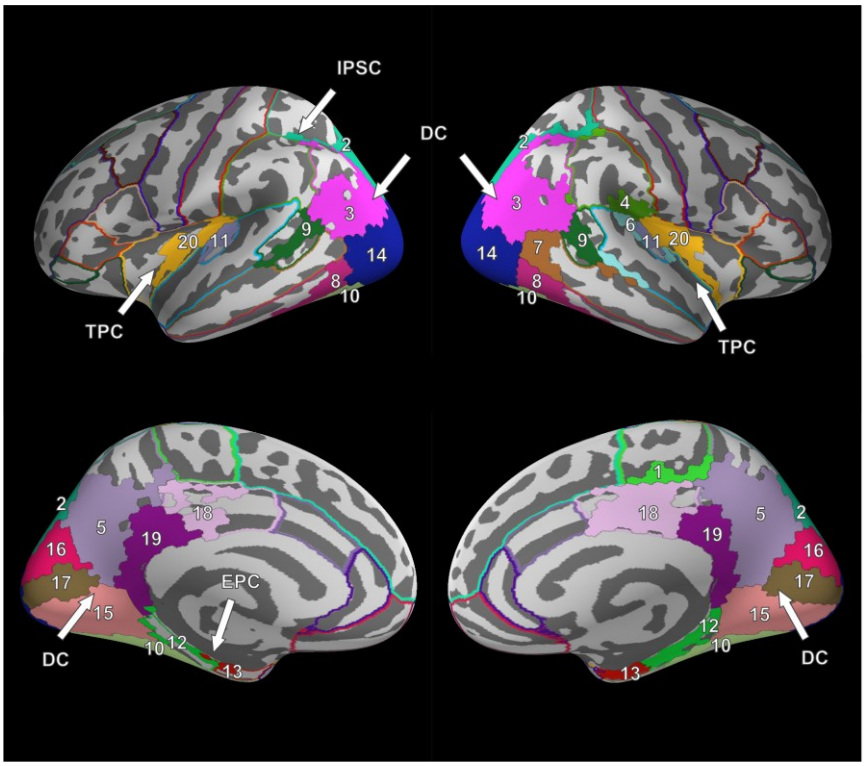

Figure 20: VS cluster results for the contrast of FRA during the image presentation versus FRA during the fixation cross presentation (DC: dorsal cluster, TPC: temporoparietal cluster, IPSC: intraparietal sulcus cluster, EPC: entorhinal-parahippocampal cluster). Separate ROIs are highlighted in different colors according to the Desikan-Killiany atlas (Desikan et al. 2006). Table 1 lists the ROIs corresponding to the numbers. Figure reprinted from (Kiefer et al. 2022). Copyright 2022 by Kiefer et al.

For FV, four clusters were found—two in the left and two in the right hemisphere. When compared across hemispheres, the two sets of clusters were nearly identical: one cluster covered the posterior parts of the brain while the other cluster covered parts of the insula and the temporoparietal region (Figure 19). The first cluster is referred to as the dorsal cluster. It covered the entirety of the occipital lobe, parts of the parietal lobe, the temporal lobe and some regions of the cingulate cortex. The second cluster is referred to as the temporoparietal cluster. It encompassed parts of the supramarginal gyrus (#4), the superior temporal gyrus (#6), the transverse temporal gyri (#11) and the posterior parts of the insula (#20). All regions exhibited bihemispheric activity except for the middle temporal gyrus (#7), which was only active in the right hemisphere.

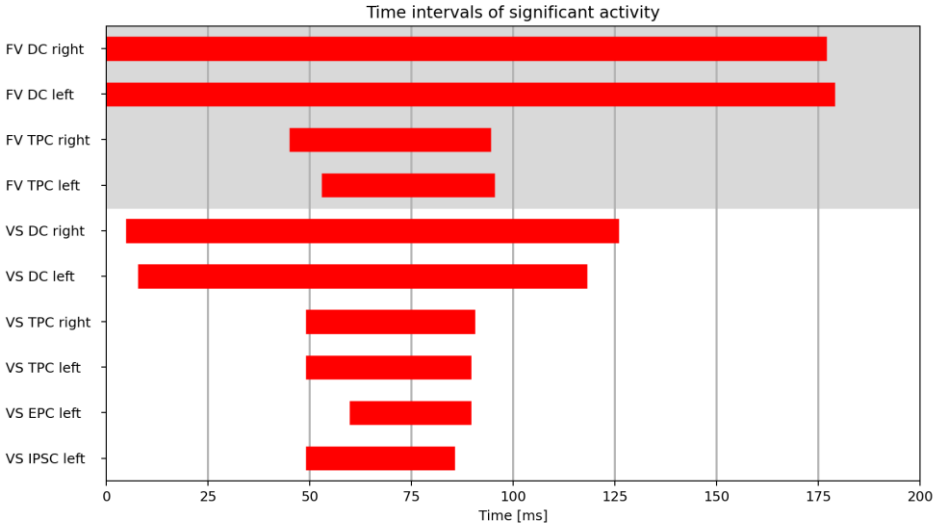

Figure 21: Time intervals with significant activity during FV and VS based on the SCPT clusters (DC: dorsal cluster, TPC: temporoparietal cluster, IPSC: intraparietal sulcus cluster, EPC: entorhinal-parahippocampal cluster) with fixation onset at t = 0 ms during FV and VS. Figure reprinted from (Kiefer et al. 2022). Copyright 2022 by Kiefer et al.

Six clusters were found for VS, which covered roughly the same areas as compared to FV, however during VS, the left dorsal cluster was broken up into three separate parts. Two small clusters, referred to as the entorhinal-parahippocampal cluster and the intraparietal sulcus cluster, were split off from the main dorsal cluster. The entorhinal-parahippocampal cluster covered the entorhinal cortex (#12) and the parahippocampal cortex (#13) (bottom left of Figure 20) while the intraparietal sulcus cluster covered a small part of the superior parietal cortex (#2) at the intraparietal sulcus (top left of Figure 20). Compared to FV, multiple regions, namely the paracentral lobule (#1), supramarginal gyrus (#4), and superior temporal gyrus (#6), displayed significant FRF activity in only the right but not in the left hemisphere during searching.

Notwithstanding the paracentral lobule, no significant activity was found in the frontal areas during any of the tasks. The Gantt chart in Figure 21 illustrates the temporal extent of the clusters.

Table 1: Regions of interest (ROIs) exhibiting significant FRA differences for the image-fixation and fixation-cross-fixation contrasts. For each ROI, the clusters (DC: dorsal cluster, TPC: temporoparietal cluster, IPSC: intraparietal sulcus cluster, EPC: entorhinal-parahippocampal cluster) and the MNI coordinates from the vertices with maximum activity are presented. The dash '-' indicates that no significant FRA differences were found. TPC regions are marked in bold. Table taken from (Kiefer et al. 2022). Copyright 2022 by Kiefer et al.

ROI	#	Anatomical label	Cluster location			
			Free Viewing (FV)		Visual Search (VS)	
			left hemi.	right hemi.	left hemi.	right hemi.
Frontal lobe						
ParaCeL	1	Paracentral lobule	DC -17, -31, 43	DC 18, -42, 43	-	DC 18, -42, 43
Parietal lobe						
SPC	2	Superior parietal cortex	DC -8, -90, 25	DC 14, -81, 32	DC and IPSC -8, -90, 25	DC and IPSC 14, -81, 32
IPC	3	Inferior parietal cortex (angular gyrus)	DC -29, -81, 13	DC 33, -75, 18	DC and IPSC -29, -81, 13	DC and IPSC 40, -67, 13
SMG	4	Supramarginal gyrus	**TPC** **-36, -36, 18**	**TPC** **40, -36, 18**	-	**TPC** **40, -36, 18**
PreC	5	Precuneus	DC -21, -61, 9	DC 20, -56, 9	DC -21, -61, 9	DC 17, -55, 14
Temporal lobe						
STG	6	Superior temporal gyrus	**TPC** **-38, -37, 11**	**TPC** **40, -35, 13**	-	**TPC** **1, -16, 23**
MTG	7	Middle temporal gyrus	-	DC 49, -59, 6	-	DC 49, -59, 6
ITG	8	Inferior temporal gyrus	DC -43, -53, -10	DC 45, -63, -9	DC -43, -53, -10	DC 45, -63, -9
BSTS	9	Banks superior temporal sulcus	DC -44, -54, 9	DC 46, -46, 10	DC -48, -53, 6	DC 46, -46, 10
FG	10	Fusiform gyrus	DC -29, -74, -7	DC 27, -74, -7	DC -29, -74, -13	DC 27, -74, 7
TTG	11	Transverse temporal gyrus	**TPC** **-38, -27, 5**	**TPC** **44, -21, 5**	**TPC** **-41, -26, 2**	**TPC** **44, -21, 5**
EC	12	Entorhinal cortex	DC -20, -10, -30	DC 21, -11, -29	EPC -22, -22, -23	EPC 21, -11, -29
PHG	13	Parahippocampal gyrus	DC -20, -18, -26	DC 23, -17, -28	EPC -20, -18, -26	EPC 23, -17, -28
Occipital lobe						
LOC	14	Lateral occipital cortex	DC -16, -97, -2	DC 30, -86, 1	DC -16, -97, -2	DC 30, -86, 1
LG	15	Lingual gyrus	DC -11, -85, -13	DC 30, -86, 1	DC -11, -85, -13	DC 17, -62, 1
C	16	Cuneus	DC -10, -73, 19	DC 10, -79, 28	DC -10, -73, 19	DC 10, -79, 28
PeriCC	17	Pericalcarine cortex	DC -15, -94, 1	DC 18, -94, 0	DC -15, -94, 1	DC 18, -94, 0
Cingulate cortex						
PCC	18	Posterior cingulate cortex	DC -16, -37, 39	DC 11, -38, 41	DC -2, -23, 27	DC 5, -28, 27
ICC	19	Isthmus cingulate cortex	DC -14, -51, 4	DC 17, -50, 4	DC -14, -51, 4	DC 17, -50, 4
Insula						
PI	20	Posterior insula	**TPC** **-35, -20, 1**	**TPC** **35, -19, 11**	**TPC** **-35, -20, 1**	**TPC** **34, -19, 7**

8.3.2 GENERALIZED PARTIAL DIRECTED COHERENCE ON SINGLE-EPOCH DATA

The effects on the network topology of top-down guidance during VS as compared to simply freely viewing images (FV) were analyzed using GPDC. Based on the respective first-differenced ROI time courses, the effective connectivity networks were computed for FV and VS (see section 8.2.3 for details).

The GPDC group-level results for FV, VS, and the contrast between FV and VS are presented in Figure 22. The ROIs were arranged by cluster and colored according to which sections of the brain they belong (frontal lobe: magenta, insula: blue, cingulate cortex: yellow, temporal lobe: turquoise, parietal lobe: red, and occipital lobe: green). As the results for the delta, theta, and alpha bands were highly similar, only the alpha, beta1, beta2, and gamma band are shown in Figure 22. The delta and theta band can be found in the Appendix in Figure 45.

In response to fixations during FV, interactions emerged mainly within the parietal, temporal, and occipital regions (Figure 22, left). Specifically, visual areas in the occipital lobe and in the (inferior) temporal gyrus such as the fusiform gyrus were involved. This was observed across all frequency bands.
Neighboring regions in the temporoparietal cluster (cf. TPC in Figure 19 consisting of the PI, SMG, STG, and TTG) displayed particularly high local connectivity in both hemispheres but they were also well-connected with other ROIs in the parietal lobe (PCC and PreC), the temporal lobe (BSTS, EC, FG, ITG, and PHG), and the cingulate cortex (ICC). As a result, these four regions exhibited a high node degree (Figure 23). The node degree generally tended to increase with the frequency. Furthermore, many connections involved ROIs in the occipital lobe. A total of five inter-hemispheric causal interactions were identified: from the left ICC to the right LG, from the left PreC to the right PreC, from the right ICC to the left PCC and to the left SMG and from the right PeriCC to the left LG.

The GPDC group-level results for fixations during VS are depicted in Figure 22 (middle). Similar to FV, interactions emerged mainly within the parietal, temporal, and occipital regions and the node degree tended to increase with the frequency.
The temporoparietal cluster regions were again well-connected in the right hemisphere, namely with regions in the temporal lobe (BSTS, ITG, MTG, PHG) and the frontal lobe (ParaCeL). The right SMG displayed the highest number of interactions as it was connected to all of the ROIs mentioned above in addition to the other ROIs in the temporoparietal cluster. In comparison to the right hemisphere, the high local degree of connectedness was diminished in the left hemisphere. A total of eight inter-hemispheric causal interactions were identified: from the left C to the right C and vice versa, from the left ICC to the right ICC and vice versa, from the left ICC to the right LG, from the left LG to the right PreC, from the right EC to the left PHG, and from the right LG to the left PeriCC.
During both tasks, most of the interactions were short-range connections, i.e., they were found to be between neighboring ROIs. This was not only true for most of the intra-sectional connections, but it was also true for many of the inter-sectional connections. Only a few ROIs interacted across hemispheres.

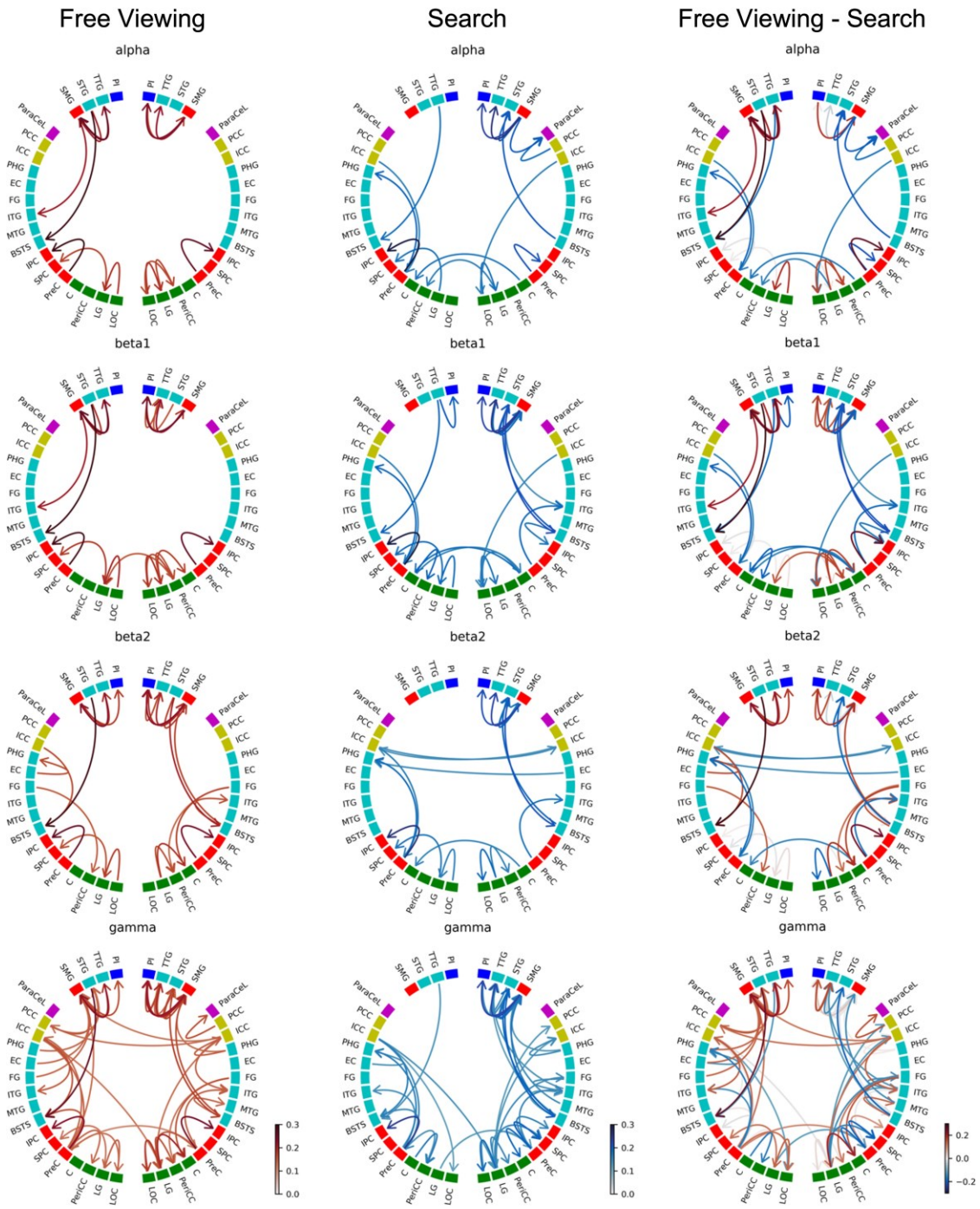

Figure 22: GPDC group-level results for fixation onset during FV (left), VS (middle), and FV minus VS (right). Stronger connections during FV are indicated by red arrows and stronger connections during VS are indicated by blue arrows. If the connections were of similar strength during FV and VS, the arrows are grey. The ROIs are grouped by clusters and colored according to the anatomical higher-level regions (frontal lobe: magenta, insula: blue, cingulate cortex: yellow, temporal lobe: turquoise, parietal lobe: red, occipital lobe: green). See Appendix Figure 45 for the results of the delta and theta bands. Figure reprinted from (Kiefer et al. 2022). Copyright 2022 by Kiefer et al.

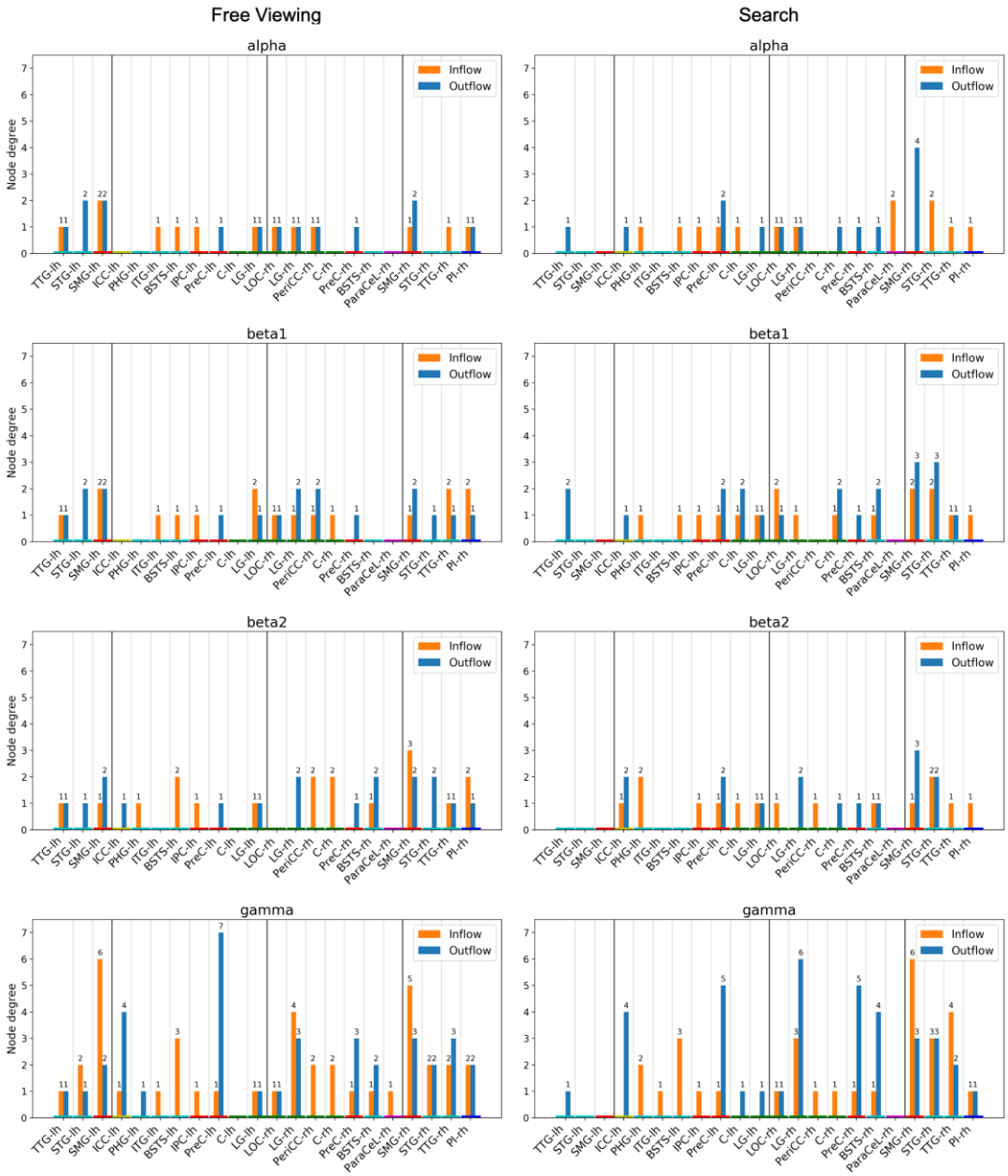

Figure 23: Node degree (the number of in- and outflowing connections) for each ROI. ROIs were only included if the node degree was equal to or above the 95th percentile according to the random permutation analysis in at least one frequency band. The ROIs are grouped by clusters and colored according to the anatomical higher-level regions (frontal lobe: magenta, insula: blue, cingulate cortex: yellow, temporal lobe: turquoise, parietal lobe: red, occipital lobe: green). See Appendix Figure 46 for the results of the delta and theta bands. Figure reprinted from (Kiefer et al. 2022). Copyright 2022 by Kiefer et al.

Figure 22 (right) is a direct comparison of the GPDC group-level results where the VS causality matrix was subtracted from the FV causality matrix. The circular plots show that most of the interactions were limited to one of the two conditions. The few interactions, which did display consistent strengths during both conditions, were marked with gray arrows. These included, for example, the right PI to the right STG, the right SMG to the right PI, and the right SMG to the right TTG. Local interactions in the temporoparietal cluster were strongly enhanced during VS as compared to FV.

Random permutation analysis was used to identify ROIs with particularly high node degrees in at least one of the frequency bands (Figure 23). During FV, twelve ROIs exhibited a significantly high node degree with the SMG, TTG, and LG having a significantly high node degree in both hemispheres. Moreover, a significant number of connections was found for the ITG, PreC, and STG in the left hemisphere and for the BSTS, the PI, and the PeriCC in the right hemisphere. During VS, 16 ROIs exhibited a significantly high node degree with the BSTS, C, and PreC having a significantly high node degree in both hemispheres. The temporoparietal cluster regions were only well-connected in the right hemisphere while none of their counterparts in the left hemisphere displayed a particularly high node degree. Additionally, the node degree was significantly high in the LOC, LG, and ParaCeL in the right hemisphere and the ICC, IPC and PHG in the left hemisphere.

During VS, the high local connectivity observed in the temporoparietal cluster regions was diminished in the left hemisphere as compared to FV, however, the number of connections for the right SMG was generally greater (Figure 23, Search). In fact, the highest overall node degree was observed during VS for the right SMG in the gamma band with six in- and three outflowing connections matched only by the right LG with three in- and six outflowing connections in the gamma band. The next highest node degree during VS was six, which was observed for four ROIs—the PreC in both hemispheres, the right STG, and the right TTG. During VS, the node degree was generally lower in the left hemisphere where the highest number of connections was six. During VS, the right SMG always exhibited the highest node degree, irrespective of the frequency band.

For FV, the greatest node degree was eight, which was found in three ROIs, the left PreC and the SMG in both hemispheres (Figure 23, Free Viewing). The right SMG had five in- and three outflowing connections while the left SMG had six in- and two outflowing connections. For the left PreC, there was only one inflowing versus seven outflowing connections. The next highest node degree was seven, which was observed in only a single ROI—the right LG in the gamma band. In most frequency bands, the greatest node degree was found in left SMG.

8.3.3 Correlation analysis between ROI FRA amplitude and search response time

In order to identify the ROIs where activity was related to the process of target recognition in the VS task, it was investigated on a trial-by-trial basis how the brain activity during the first fixation on the search target was related to the response time. This was done by computing Pearson's correlation coefficient between the single-trial FRA amplitudes and single-trial response times (see section 8.2.4 for details).

Figure 24 depicts the grand average of ROI FRA time courses over subjects and trials for the first fixation on the search target. For each ROI, the FWHM interval around the maximum activity was determined (Figure 25). Given that the activity started to increase at around 30 ms from fixation onset and that the average fixation duration during VS trials was approximately 200 ms long (Figure 10), the FWHM intervals were restricted to the interval from 30 to 200 ms from fixation onset.

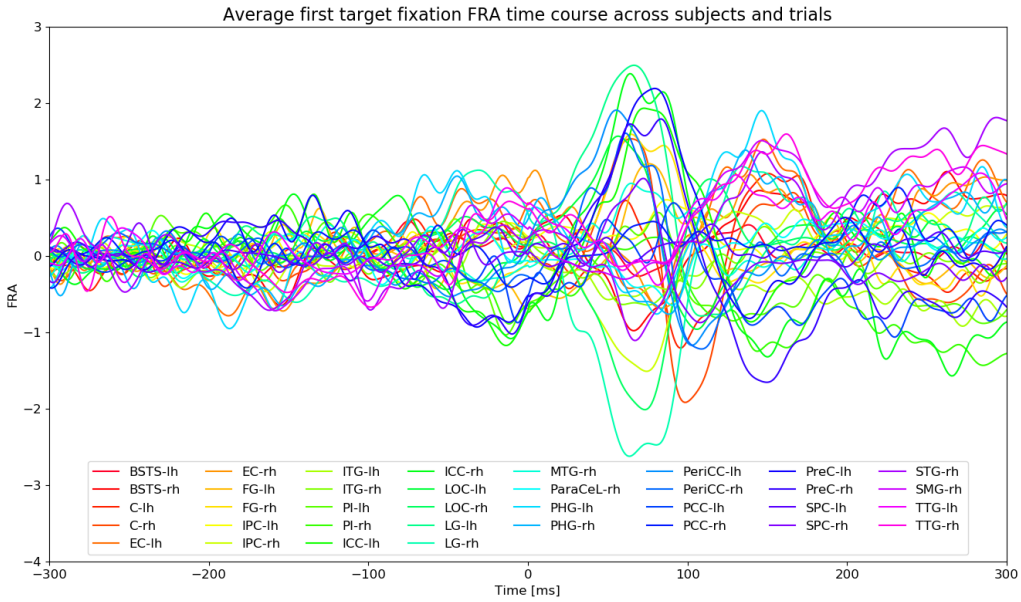

Figure 24: Grand average of ROI FRA time courses over subjects and trials for the first fixation on the target object during a search trial. Time zero corresponds to the fixation onset. Figure reprinted from (Kiefer et al. 2022). Copyright 2022 by Kiefer et al.

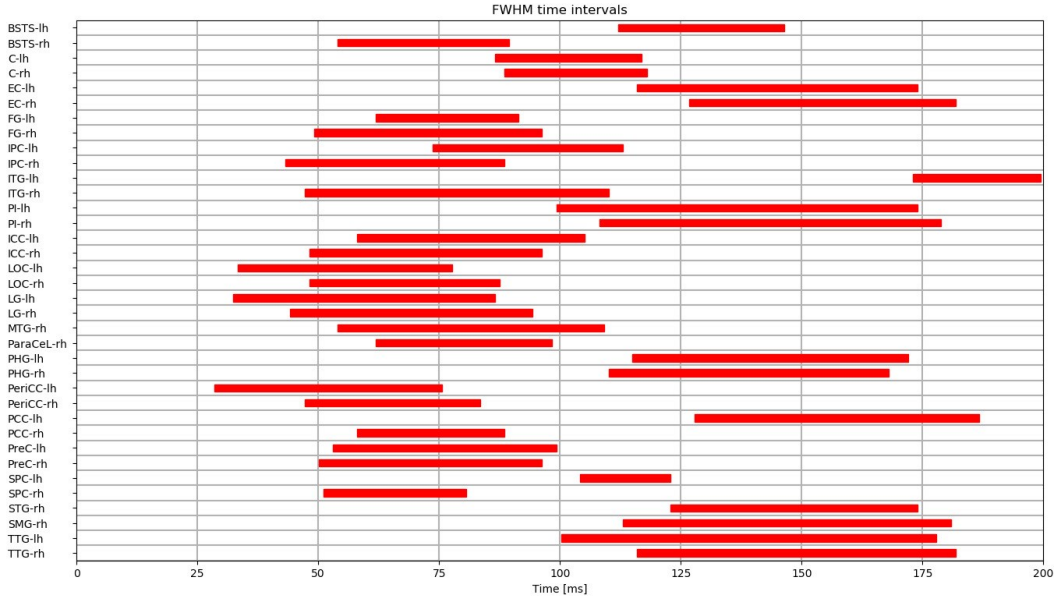

Figure 25: The full-width-at-half-maximum (FWHM) time intervals for the grand average ROI FRA time courses. Time zero corresponds to the onset of the first fixation on the search target. 'lh' and 'rh' are abbreviations for the left and right hemisphere, respectively. Figure reprinted from (Kiefer et al. 2022). Copyright 2022 by Kiefer et al.

After FDR-correction, there was a significant, negative correlation (r = -0.141, p < 0.05) between the response time and the FRA amplitude in the right SMG in the FWHM interval from 113 to 181 ms from fixation (Figure 26). This means that in trials with higher activity in the right SMG, the subjects tended to respond faster. For none of the other ROIs significant correlations could be identified.

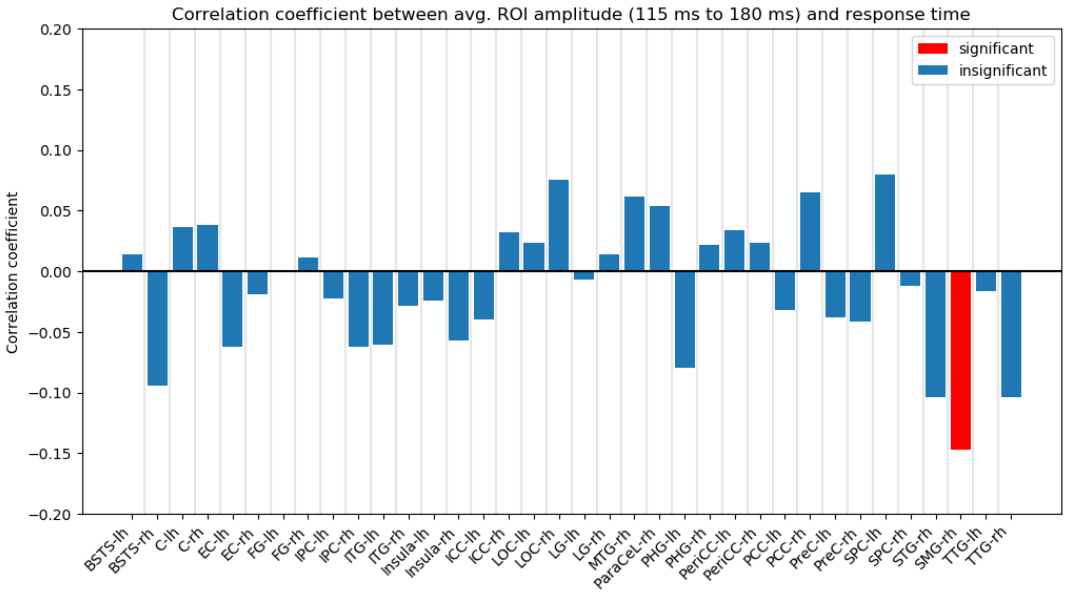

Figure 26: Pearson's correlation coefficient between the search response time and the FRA amplitude of the fixation on the search target averaged across time in the time interval of 115 to 180 ms from fixation onset. A significant ($p < 0.05$) correlation coefficient after FDR-correction is indicated by a red bar. 'lh' and 'rh' are abbreviations for the left and right hemisphere, respectively. Figure reprinted from (Kiefer et al. 2022). Copyright 2022 by Kiefer et al.

8.4 Discussion

SCPT was used to identify ROIs whose activity was related to the processing of visual information obtained through self-paced eye movements. Based on these ROIs causal interaction networks were computed to investigate how goal-directed behavior affects the communication in the brain.
For both tasks, bilateral temporoparietal and dorsal clusters were found with a high degree of symmetry across hemispheres. Granger causality analysis using GPDC revealed that, during FV, the regions belonging to temporoparietal cluster were well-connected, both with regions of the same cluster and with outside ROIs. During VS, the right SMG stood out with the most connections of any ROI. Moreover, the right SMG was also the only ROI where a significant correlation between the activity and shorter search response times could be identified. These results corroborate the hypothesis that goal-directed behavior affects the whole-brain connectivity and the additional processes required for a guided visual search are reflected by the changes in the networks.

8.4.1 Identification of Regions of Interest

SCPT revealed 39 ROIs (20 in the right and 19 in the left hemisphere) for FV and 36 (20 in the right and 16 in the left hemisphere) for VS (Table 1). The ROIs were highly symmetric across hemispheres and the same 20 ROIs were identified in the right hemisphere for FV and VS. However, a major difference was that three ROIs in the left hemisphere—the ParaCeL, SMG, and STG—only displayed significant activity during FV and not during VS.

The transitory region between the STG and the SMG is known as the temporoparietal junction. Lesions in the right temporoparietal junction have been

associated with visual processing defects such as left spatial neglect or hemiextinction (Karnath et al. 2004; Meister et al. 2006; Corbetta, Patel, and Shulman 2008; Ticini 2013). Shulman, Corbetta and colleagues (2007, 2008) proposed that a ventral attention network (VAN) consisting of the right temporoparietal junction and the right ventral frontal cortex (i.e., parts of middle frontal gyrus (MFG), inferior frontal gyrus (IFG), frontal operculum, and anterior insula) plays a role in redirecting attention to new, behaviorally relevant objects (Shulman et al. 2007; Corbetta, Patel, and Shulman 2008). The right temporoparietal junction displaying significant activity during both FV and VS might imply that similar mechanisms are generally engaged when attention is shifted based on top-down guidance or bottom-up salience.

Unlike during FV, where the temporoparietal junction was significantly active in both hemispheres, there was only significant activity in the right hemisphere during VS. This discrepancy can potentially be explained by differences in the response to target and non-target (distractor) stimuli. It has been reported that the left and right temporoparietal junction both respond to targets irrespective of the hemifield they appear in (Dragone et al. 2015; Silvetti et al. 2016). Similarly, the right temporoparietal junction also responds to distractors in both hemifields, however, the left temporoparietal junction is only engaged by distractors in the right hemifield (Dragone et al. 2015; Silvetti et al. 2016). This could explain why the left temporoparietal junction was not significantly active during VS. Distractors were placed with equal probability in the left and right halves of the images meaning that the left temporoparietal junction might only have been engaged in half of the fixations. After averaging across all fixations, the activity might have been considerably lower in the left hemisphere as compared to the right hemisphere. Since there is as per definition no distinction between target and distractor stimuli for FV, this would not apply to fixations during FV. Further analysis of the FRA would be required to elucidate the influence of target and non-target locations (relative to the fixation position) on the activity in the left and right temporoparietal junction.

The third ROI which was absent in the left hemisphere during VS was the ParaCeL. Within the ParaCeL lies the supplementary eye field (SEF), which is, together with the frontal and parietal eye fields, one of the three key areas in primates responsible for the performance and control of saccades (Grosbras et al. 1999). For example, in macaques, eye movements could be elicited through electrical stimulation of the SEF (Schlag and Schlag-Rey 1987, 1992; Tanji 1994; Tehovnik 1995; Grosbras et al. 1999), and, in humans, activations in the SEF were observed during voluntary, self-paced eye movements (Petit et al. 1993). A left hemispheric dominance of the SEF was reported in several studies, particularly during endogenous eye movements (Petit et al. 1993; Grosbras et al. 1999), while visually guided saccadic eye movements were seen to engage the right SEF (Luna et al. 1998). Differences in activity during FV and VS could be explained by these previous reports. During FV eye movements are likely to be generated endogenously based on bottom-up salience, which could rely more strongly on a left-hemispheric network as compared to the eye movements generated during VS as a result of top-down guidance.

Two major clusters—the temporoparietal cluster and the dorsal cluster—were found in each hemisphere. Since the temporoparietal cluster comprises the PI and TTG along with the SMG and the STG it is likely that functional relationships exist between these areas. Even though activity in the PI is often considered to be related to empathy, pain, and somatosensory stimuli (Kurth et al. 2010), there is also evidence that the PI is involved in visual processing. Specifically, cortical damage in the PI was reported in patients with hemispatial neglect (Golay, Schnider, and Ptak 2008). Moreover, using diffusion-weighted imaging, direct, anatomical connections between the PI and the posterior temporal, parietal, and sensorimotor areas have been uncovered and these regions are mostly in line with the other members of the temporoparietal cluster (SMG, STG, and TTG) (Cloutman et al. 2012; Ghaziri et al. 2017; Uddin et al. 2017). While the TTG, or Heschl's gyri, are thought to comprise the primary auditory cortex (Morosan et al. 2001; da Costa et al. 2011), there is still some evidence that they might be required for visual processing. For example, intraoperative electrical stimulation (Gharabaghi et al. 2006) and transcranial magnetic stimulation (Ellison et al. 2004) led to disturbed visual search behavior. Moreover, spatial neglect manifested in patients with lesions in Brodmann areas 22 and 42 in the right temporal lobe (Karnath, Ferber, and Himmelbach 2001) with Brodmann area 42 being part of the TTG (Campain and Minckler 1976). Based on the fact that the PI, SMG, STG, and TTG formed the temporoparietal cluster and that, based on the literature, damage to any of these areas may lead to visual processing defects, it is likely that these ROIs form a functional network. This claim is further supported by the GPDC results (section 8.3.2), where these ROIs were strongly inter-connected.

Besides temporoparietal cluster, the dorsal cluster was the other major cluster revealed by SCPT to be significantly active during both FV and VS. A comparison with the probabilistic maps of visual areas created by Wang et al. (2015) shows that the dorsal cluster comprises the primary and many of the higher visual areas (Wang et al. 2015). For example, the primary visual areas are found in the C, PeriCC and LG. Moreover, the dorsal stream flows from C through the LOC to the IPC from whereon it flows towards the MTG and the ITG while the ventral stream goes from the LG to the FG (Wang et al. 2015; Goodale and Milner 1992; Milner and Goodale 2006). Since there was strong FRA in the dorsal cluster during both FV and VS there are potentially common underlying visual processing mechanisms. Such processes could include the processing of basic features such as contrast or orientation, color, and boundary detection (Zeki et al. 1991; Tootell et al. 1998; Lee et al. 1998).

Despite FV and VS having clearly different requirements for cognitive processing, the clusters covered almost identical areas in both tasks. In fact, no significant clusters could be identified when performing SCPT with contrasts of averaged FRAs during FV and VS (results not shown). Accordingly, there are at most small differences between the averaged time courses. However, important information at the single-epoch level could have been lost in the averaging process, and as a matter of fact, differences in causality networks, which were estimated based on single epochs, were observed (section 8.3.1). Since the same ROIs are generally being activated, this implies that the interplay and interactions between these ROIs are what is pivotal for understanding the differences between guided visual searching and freely viewing naturalistic images.

In summary, the literature points towards the temporoparietal cluster as a whole instead of just the temporoparietal junction being involved in visual processing and that it is also partly involved in attention shifting. Inactivation, e.g., through TMS, or damage to these areas can lead to visual processing defects such as spatial neglect or hemiextinction. Based on the presence of significant FRA in the temporoparietal cluster during both tasks, it appears that the cluster is potentially relevant for both visual search and visual exploration. More generally, the areas with significant FRA were overall largely the same for both tasks, which implies that the processes for searching and freely viewing an image rely on the same areas. This leads to the hypothesis that the deciding factor is the interplay of these areas during the different tasks.

8.4.2 GENERALIZED PARTIAL DIRECTED COHERENCE ON SINGLE-EPOCH DATA

The initial hypothesis stated that changes in the topography of the whole-brain causality network would be affected by the additional processes required for a guided visual search as compared to freely viewing the images. To test this, causal interactions were computed between ROIs based on the single-epoch ROI time courses in the time interval between 0 and 300 ms from fixation onset and random permutation analysis was used to identify ROIs with significant node degrees. Depending on the task, distinct causality networks and node degrees were obtained as discussed in more detail below.

For FV, many local causal interactions were identified between the ROIs in the temporoparietal cluster (PI, SMG, STG, and TTG). Except for the left PI, all of these ROIs exhibited a significantly high node degree in both hemispheres. These findings are in agreement with recent reports that attention shifting relies on the temporoparietal areas in both hemispheres (Dragone et al. 2015; Silvetti et al. 2016) instead of there being a right hemispheric dominance as believed in earlier reports (Corbetta, Patel, and Shulman 2008; Shulman et al. 2010). Furthermore, the results presented here establish that the (right) PI and the TTG might also participate in attention shifting along with the temporoparietal junction as identified originally by Corbetta *et al.* (2008).

For VS, the right SMG always featured the highest total node degree irrespective of the frequency band with many connections being unique to VS (Figure 22, right). Additionally, the right SMG might act as a central node for the temporoparietal cluster as it was the only ROI with bidirectional connections with the other three ROIs. Besides the right SMG, the node degrees were largely comparable across tasks. The enhanced connectivity of the right SMG as compared to FV suggests an active contribution to processes specific to VS.

The amplified connectivity in the right SMG during VS could be explained by two mechanisms in accordance with the initial hypothesis: target template matching and attention shifting. The obvious difference between searching an image for an object and freely viewing an image is that, during the search, the visual input has to be compared to a mental representation of the search target in order to confirm the presence or absence of the target at the fixation point—a process sometimes

referred to as target template matching (Wolfe 2021). Additionally, for an efficient search, attention has to be shifted to the location most likely to lead to a successful conclusion. In other words, after processing the visual input from the current fixation, the following saccade has to be directed to the location with the highest probability of containing the target object. This process is governed by a priority map, which is, according to Guided Search 6.0, a combination of bottom-up (salience) and top-down (search template driven) guidance together with other aspects such as the structure and meaning of scenes or the history of prior attention (Wolfe 2021). Target template matching and attention shifting do in fact not have to be mutually exclusive processes and there is evidence for both that the right SMG is involved (Shulman et al. 2007; Corbetta, Patel, and Shulman 2008; Shulman et al. 2010).

One causal interaction, from the right SMG to the right ParaCeL, was particularly intriguing when considering the process of attention shifting. This connection was found only during VS. As discussed in section 8.4.1, the ParaCeL comprises the SEF, which is crucially involved in controlling the saccade direction given multiple competing options (Parton et al. 2007). Additionally, the SEF was reported to help determine the optimal course of action in goal-directed behavior by computing and evaluating the expected outcome of all possible saccade options (Stuphorn 2015). Based on these studies it is probable that the SEF is responsible for generating and evaluating the priority map for saccade guidance. Connections between the right SMG, the right frontal eye field (FEF), and the left SEF have been observed in a functional connectivity study with the right SMG as seed during the execution of saccades during planned grasping motions (Baltaretu et al. 2020). The authors of the study concluded that saccade-related information for the trans-saccadic updating of grasp orientation was passed from the FEF and SEF to the right SMG. Yet the results presented here show a connection in the opposite direction. Based on the previous reports that the SEF is responsible for the generation and evaluation of the priority map and that the SMG participates in the high-level integration of visual input, it is reasonable to assume that, after a fixation, the right SMG supplies the right SEF with the information required for updating the search priority map and determining the best position for the following fixation. This is further supported by the fact that the connection was only found in the delta, theta, and alpha bands, which roughly coincide with the frequency of the saccade-fixation cycle of on average four saccades and fixations per second.

Unfortunately, there were only small differences between the frequency bands making it difficult to discern whether there are some cognitive functions that are restricted to certain frequency bands. In fact, many of the discussed interactions were found in all six frequency bands. One interpretation could be that, instead of some sub-networks specific to certain functions, the overall communication in the temporoparietal cluster is increased during VS. Alternatively, it is possible that the functions require communication pathways in multiple frequency bands due to the higher complexity of processing naturalistic stimuli.

In summary, the hypothesis that the temporoparietal junction (the SMG and STG) contribute to the detection of the search target and to the guidance of the eye movements during a visual search is upheld by the results presented here.

Furthermore, a novel observation is presented where the PI and TTG appear to be of relevance as well and it is hypothesized that, together, these four ROIs form a functional unit for these two processes with the right SMG as central node. One connection, from the right SMG to the right ParaCeL, is particularly emphasized with respect to guiding eye movements based on the search priority map.

8.4.3 Correlation analysis between ROI FRA amplitude and search response time

To investigate the relation between neuronal activity and behavioral performance during VS, the single-trial search response times were correlated with the FRA amplitudes of the first fixation on the search target for each trial. A relatively weak but significant negative correlation was found between the response time and the FRA amplitude in the right SMG, which indicates that shorter response times coincided with stronger activity in the right SMG. Other ROIs did not display significant correlations.

The FWHM interval for the FRA in the right SMG was found between 113 and 181 ms from fixation onset. A significant negative correlation of the FRA amplitude in this time interval and the response time could be observed. By this time, the visual system would already have formed mental representations of complex visual objects. For example, macaque monkeys were able to discriminate faces after, on average, 108 ms from stimulus onset and it is to be expected that the same would be true for humans since they demonstrated similar performances in a rapid categorization task as compared to macaques (Keysers et al. 2001). In conclusion, the observed correlation is most likely related to higher-level visual processes since lower-level visual features (e.g., orientation and color) would already have been extracted before the onset of the FWHM interval.

Three interpretations for the negative correlation between the response time and the FRA amplitude in the right SMG would be possible. First, in feature integration theory, visual features of objects such as color and shape etc. are extracted independently from one another and then have to be bound into single mental representation of the objects via an attention-related process (Treisman and Gelade 1980; Roskies 1999; Treisman 1996; Cave and Wolfe 1999). As activity in the right SMG has generally been linked to attention-related processes (Shulman et al. 2007; Corbetta, Patel, and Shulman 2008; Shulman et al. 2010), this could be a plausible explanation for the observed negative correlation. Greater attention as shown by greater amplitudes in the right SMG could facilitate faster integration of visual features and thus lead to faster target recognition. Second, there is evidence that the right SMG assists in trans-saccadic integration, which is another process modulated by attention (Stewart and Schütz 2018) where object locations and features are bound and updated across saccades (Dunkley, Baltaretu, and Crawford 2016). Again, greater attention and enhanced activations in the right SMG could enable faster trans-saccadic integration, which would in turn lead to faster target recognition. Finally, visual input has to be matched against a mental representation of the target object, the target template, in order to determine whether the target has been detected (Wolfe 2021). This is a process called template matching in Wolfe's Guided Search 6.0 framework (Wolfe 2021). Since faster template matching

would directly translate to faster target recognition and hence to shorter response times, the observed negative correlation might point towards the right SMG being involved in this process. All three interpretations are related to object recognition and would therefore be in accordance with previous reports that the right SMG participates in target detection (Linden et al. 1999; Shulman et al. 2010).

Of the three possible explanations for the negative correlation between the search response time and the FRA amplitude in the right SMG in response to the first fixation on the search target (template matching, trans-saccadic integration, and binding), both trans-saccadic integration and binding are processes modulated by attention. Given that the SMG has previously been reported in the context of attention-related processes, these two processes are potentially the more likely explanations for the observed effect than template matching. In any case, the results presented here corroborate earlier reports that the right SMG is involved in target.

8.5 Conclusion

Whole-brain causal interactions during active vision were investigated with MEG in combination with SCTP and Granger-based GPDC. Two clusters with significant fixation-related evoked activity were identified, a temporoparietal cluster comprising parts of the SMG, STG, TTG, and PI as well as a dorsal cluster consisting of the occipital cortex including the primary visual areas and areas associated with the higher visual areas of the dorsal and ventral visual streams. Based on the findings revealed by GPDC, the areas in the temporoparietal cluster were not only strongly inter-connected with one another but also with areas in the dorsal cluster. This was the case for both FV and VS. The results suggest that eye movements during active vision are at least in part guided by the four temporoparietal cluster regions. Particularly for guided visual searching, the right SMG appeared to take a central role as it featured the overall highest number of causal interactions and it was the only area bidirectionally connected to all other areas in the temporoparietal cluster. The connection from the right SMG to the right SEF was highlighted with the interpretation of the right SMG providing the SEF with information for the purpose of updating the priority map guiding the saccades towards the search target. The right SMG appearing to facilitate the integration of visual input for object recognition (based on the correlation between shorter search response times and stronger activity in the right SMG following fixations on the search target) would also support this interpretation. Together, these findings show the importance of the temporoparietal junction for the guidance of eye movements and object recognition during guided visual searching. Furthermore, mechanisms are pointed out for how the supramarginal gyrus in particular might help facilitate eye movement guidance and object recognition within the theoretical framework of Guided Search 6.0.

9 TIME SERIES CLASSIFICATION: TASK IDENTIFICATION AND NEURAL FINGERPRINTING

9.1 INTRODUCTION

The electrophysiological response to a fixation, called the fixation-related evoked activity (FRA), was found to be a neural marker of natural visual processing (Nikolaev, Meghanathan, and van Leeuwen 2016; Ossandón et al. 2010). Thereby, it enabled the study of neural activity during visual exploration using unconstrained eye movements. For example, it was possible to distinguish between fixations on targets and non-targets using the fixation-related evoked potential (FRP) (Finke et al. 2016).

During both the free viewing (FV) and the memory task (ME), the subjects perform fixations on the objects embedded in the images with the difference that, as the name of the task suggests, these objects have to be memorized during ME. Since the FRA has been associated with object recognition (Kamienkowski et al. 2012; Kaunitz et al. 2014) it is very likely that differences in cognitive processing during ME and FV are also reflected in the FRA when the subjects are fixating on objects.

In this chapter, single object-fixation recordings from FV and ME trials were used to identify the experimental task that was performed during the trial. For this purpose, the multivariate time series classifier Random Convolutional KErnel Transformation (ROCKET) was employed on the ROI time courses (Dempster, Petitjean, and Webb 2020). Due to its black box nature, it is difficult to gain insights about which ROIs (and which features) drive the classification accuracy of the multivariate ROCKET classifier. Therefore, its performance was compared to an ensemble of univariate ROCKET classifiers trained on individual ROIs. Furthermore, temporal cluster permutation testing was used to identify ROIs with significant differences in the representative source time courses during FV and ME.

In the past, neuroimaging research has often focused on understanding the brain at the population level—researchers sought knowledge by isolating common features across individuals (van Horn, Grafton, and Miller 2008). However, in recent years, it became increasingly clear that disregarding the individual characteristics as noise limits our understanding of the brain. Specifically, it is now believed that these individual variations convey important information (see (van Horn, Grafton, and Miller 2008) for a review). In the wake of this growing interest in the individual, the topic of neural fingerprinting emerged. Various studies have demonstrated that individuals can be identified in a cohort using different modalities such as MRI (Valizadeh et al. 2018; Wachinger et al. 2015), fMRI (Amico and Goñi 2018; Bari et al. 2019; Finn et al. 2015; Kaufmann et al. 2017; Miranda-Dominguez et al. 2014), functional near-infrared spectroscopy (de Souza Rodrigues et al. 2019), EEG (Fraschini et al. 2015; Kong et al. 2019; Rocca et al. 2014), and MEG (Sareen et al. 2021; da Silva Castanheira et al. 2021a, 2021b). However, neural fingerprinting is often based on second-order statistical summaries of brain activity such as functional connectomes (Sareen et al. 2021). Therefore, it was tested whether this

approach can be simplified by directly applying ROCKET to resting-state recordings for the purpose of neural fingerprinting.
Empty-room data was used to test whether information specific to the subjects but unrelated to the brain activity itself, such as an individual's brain anatomy or the head position in the MEG system, possesses information relevant to the classification (da Silva Castanheira et al. 2021a). Similarly, it is unclear whether day-to-day variations in the MEG background noise may affect fingerprinting accuracies.

Using ROCKET, it was possible to determine whether object fixations were performed during FV or ME with an accuracy of approximately 93%. Only 160 ms of post-fixation single-epoch recordings were required for the classification. The only ROI with significant differences in temporal dynamics between FV and ME was the right SPC. It was also one of the two main drivers for the classification accuracy along with the left PCC. Similarly, it was possible to differentiate between subjects based on resting-state data with ~93% accuracy.

9.2 METHODS

9.2.1 PRE-PROCESSING AND GENERATION OF EPOCHS

The same general data processing steps as outlined in section 0 (bad channel correction, noise reduction, and artifact removal) were followed here for all datasets (task data, resting state, and empty room). The analysis in this chapter was entirely performed on data band-pass-filtered between 1 and 45 Hz.

For the task classification, only object fixations were considered to isolate potential memorization processes during ME with the FV trials acting as a baseline for comparison. For object fixations during FV, 5751 epochs were collected across all subjects. The minimum and maximum number of epochs among subjects was equal to 129 and 236, respectively. For object fixations during ME, 6006 epochs were collected across all subjects. The minimum and maximum number of epochs among subjects was equal to 144 and 186, respectively.

For FV, the same set of ROIs as identified in section 8.3.1 were used and for ME the same steps as outlined in section 8.2.2 were followed to compute the ROIs (see Appendix Figure 44 and Table 2). Based on these ROIs, the ROI time courses were extracted (see section 8.2.3.4). Both classification and temporal clustering were restricted to the time interval between 20 and 180 ms from fixation onset. In this way, the influence from the preceding and potential subsequent saccades (see section behavioral analysis) is mostly eliminated.

For the neural fingerprinting, resting-state data from a subset of 20 subjects was used. For each of these subjects, two resting-state recordings of a length of six minutes were performed—one prior to the active vision task recordings and one after the task recordings. For 11 subjects (out of 31), the data had to be excluded from the fingerprinting analysis, as at least one of the two resting-state recordings was not available. The first 60 s of each resting-state recording were discarded to

ensure that the subjects could reach a state of resting, while the rest of the data was divided into epochs of 1.2 s length.
For the first resting-state measurement, this resulted in 3,639 epochs collected across all 20 subjects. The minimum and maximum number of epochs among subjects was equal to 148 and 188, respectively. For the second resting-state measurement, this resulted in 3,613 epochs collected across all 20 subjects. Here, the minimum and maximum number of epochs among subjects was equal to 163 and 187, respectively. In total, 7,252 epochs of resting-state data were used.

Directly after the second resting-state measurement, an empty-room measurement of approximately 10 minutes was recorded which was divided into epochs of 1.2 s length like the resting-state data. In total, 14,963 epochs were collected across all 31 empty-room measurements. The minimum and maximum number of epochs among measurements was equal to 439 and 709, respectively. The number of epochs per measurement were restricted to 439 to avoid strong imbalances between classes resulting in a total number of 13,609 epochs used in the analysis.

Finally, for the combined resting-state measurements (see section 9.2.3.3), 7,252 epochs were collected across all 20 subjects. The minimum and maximum number of epochs among subjects was equal to 334 and 374, respectively. Given that the minimum number of epochs among subjects for the empty-room data was 439, the number of epochs per subject used for the cross-over classification analysis was set to 334. A total of 6,680 epochs were used for each condition (empty-room vs. combined resting-state measurements).

9.2.2 Identification of ROIs with differing temporal dynamics during FV and ME

The goal was to find ROIs whose representative ROI time courses exhibited significant differences in FRA for object fixations during FV and ME.

9.2.2.1 Creating averaged data

The EyeLink 1000 system automatically detects fixation onsets and provides the coordinates of the gaze position at a given time point. Using this data, fixations on objects were identified for each recording run for FV and ME. A fixation was considered to be on an object if the gaze position during a fixation was within 1.7° of visual angle from the center of an object. Similar to section 8.2.2.2, these time points were used to create FRF epochs, which were then averaged around fixation onset and z-scored with respect to the baseline interval (–200 to 0 ms from fixation onset) for all combinations of recording runs and conditions.

9.2.2.2 Source localization and extraction of ROI time courses

Similar to section 8.2.2.3, dSPM was used to project the averaged FRF data from the sensor space onto the individuals' source spaces with source orientations normal to the surface. The resulting FRA data was subsequently morphed to FreeSurfer's 'FsAverage' common template source space. Finally, the same procedure as described in sections 8.2.2.4 and 8.2.3.4 was followed for the extraction of the ROI time courses. The ROIs, which were the same for FV and ME, and the vertices with maximum activity for ME can be found in the Appendix (Figure 44 and Table 2).

9.2.2.3 TEMPORAL CLUSTERING

Significant differences between the averaged ROI time courses of object fixations during FV and ME were identified using temporal cluster permutation testing (TCPT) with a pairwise independent *t*-test (Maris and Oostenveld 2007). TCPT is very similar to SCPT described in section 3 except, when testing single time series for differences, only data points adjacent in time are used to form the clusters (see step 3 of section 3.3). 30,000 permutations were performed for each cluster test. Since a separate cluster test was performed for each of the 39 ROIs, the critical alpha level of 0.05 was adjusted for multiple comparisons using the Bonferroni correction.

9.2.3 CLASSIFICATION

The classification was mainly performed using the Python packages scikit-learn and sktime (Pedregosa et al. 2011; Löning et al. 2019). For all ROCKET classifiers the default of 10,000 kernels was used with cross-validated ridge regression as the linear classifier.

9.2.3.1 SOURCE LOCALIZATION AND EXTRACTION OF ROI TIME COURSES

The source localization of the object fixations and the resting-state data was performed using dSPM as described in section 8.2.3.3. The empty-room data was also projected onto the source space using dSPM. To investigate the influence of factors pertaining to the individual (brain anatomy and position in the MEG system) each individual's empty-room data was projected onto the individual's source space with the corresponding head position. Further, to investigate whether there are day-to-day differences in the background noise, which a classifier could use to base its fingerprinting decisions on, all empty-room recordings were also projected onto the same source space from a single, randomly chosen individual. Moreover, an identical head position was used for all subjects. Thus, the only differentiating factor between recordings would be the background noise itself. All source time courses were morphed to the template source space 'FsAverage'.

The ROI time courses for the object fixations were extracted based on the ROIs in the same way as outlined in section 8.2.3.4. However, unlike the task data, there was no evoked response for the resting-state data and especially not for the empty-room data. Therefore, there was no time point around which to sensibly average the data to determine the vertices with maximum activity in each ROI (cf. section 8.2.3.4). Instead, the same vertices as identified for fixations during FV were used for the resting-state data and the empty-room data.

9.2.3.2 TASK IDENTIFICATION ON SINGLE EPOCH TIME SERIES

The ROCKET classifier was used to identify the task during which the single-epoch object fixations were performed. Leave-one-out cross validation (LOOCV) was used on the subject-level to determine the classification accuracy. The data from 30 subjects was selected for training and the data from the remaining subject was used to test the classifier's accuracy. This process was repeated until each subject was left out once. This led to a total of 31 accuracy scores for which the mean and the standard deviation was computed.

Like the multivariate case, a univariate ROCKET classifier was trained independently on the time courses for a given ROI and LOOCV was used on the subject-level for each of these univariate ROCKET classifiers. ROIs where the classification accuracy was significantly higher than the chance level were identified using a one-sample *t*-test corrected for multiple comparisons with the Bonferroni correction (39 ROIs).

9.2.3.3 RESTING-STATE FINGERPRINTING

The ROCKET classifier was used to identify the subjects from which the resting-state epochs originated. Due to the nature of fingerprinting—the fact that the subject is the class to be identified, it is not possible to divide the data into training and test sets by subject for the usual LOOCV described in section 9.2.3.2. Instead, a variation of a subject-level leave-one-out method (LOOM) was used (Schlögl and Supp 2006). Specifically, each of the 20 subjects was selected to be left out once and the ROCKET classifier was then trained on the first resting-state measurement of the remaining 19 subjects. Afterwards, the trained classifier was tested on measurement two of the same subjects. This procedure was repeated with measurement two being the training set and measurement one being the testing set. This led to a total of 40 accuracy scores for which the mean and standard deviation was computed.

Since there was only a single empty-room recording per subject, neither LOOCV nor LOOM as described above could be used to estimate ROCKET's fingerprinting accuracy on empty-room data. Therefore, stratified 10-fold cross validation (CV) was used, which divides the epochs into 10 subsets while preserving the percentage of each class (subject) in the entire dataset. Then, the classifier was trained on nine of these subsets with testing being performed on the remaining one. Again, this procedure was repeated until each subset was left out once and the mean and standard deviation of the 10 fingerprinting accuracies was computed. Empty-room data was recorded for the 31 subjects and the analysis was performed for both types of source-localized empty-room data, the data projected onto the individual source spaces with individual head positions and the data projected onto the same source space with identical head positions. To avoid imbalances between classes (empty-room measurements), the number of epochs used per measurement was set to the minimum number of epochs among measurements.

Finally, similar to training on the first resting-state measurement and testing on the second resting-state measurement, the ROCKET classifier was trained on the empty-room data and tested on the joint data of both resting-state recordings and vice versa. The same 20 subjects were used as before in the resting-state analysis. Since the number of epochs for the empty-room measurement usually exceeded that of the combined resting sate measurements for a given subject, only a subset of the data was used such that the number of epochs was the same for all subjects in the training and test sets.

9.3 Results

9.3.1 Temporal clustering of object fixations

TCPT was applied to contrasts of averaged FRA ROI time courses between object fixations during FV and ME in order to identify ROIs with significant differences in temporal dynamics for these two tasks. In only a single ROI, the right SPC, such differences could be identified (Figure 27). In the right SPC, FRA during ME predominated that of FV in two time intervals: from approximately 30 to 90 ms and from approximately 110 to 140 ms from fixation onset.

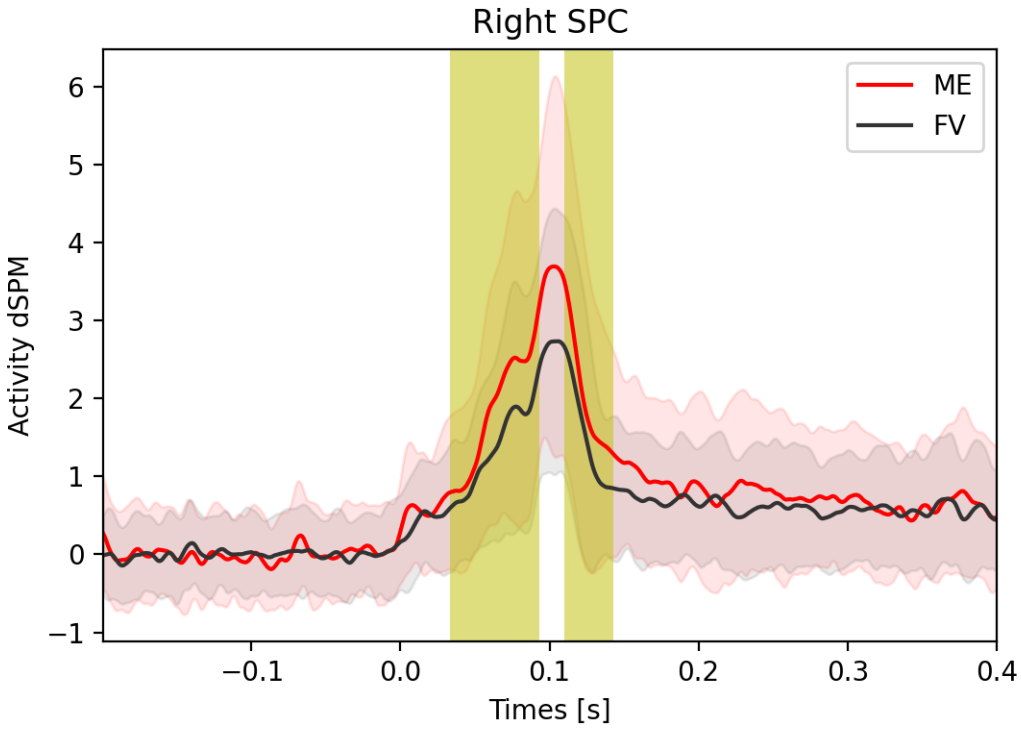

Figure 27: Group averaged FRA time courses from object fixations during FV and ME in the right SPC with significant differences identified through TCPT highlighted in yellow. The shaded areas in red and grey indicate the standard deviation across subjects for ME and FV, respectively.

9.3.2 Task identification on single-epoch time series

Figure 28 shows the ROCKET classification accuracy scores for the task identification based on ROI time courses of object fixations. The accuracy scores were obtained through LOOCV. With 52.5%, the lowest accuracy was barely above chance level of 50% while for one subject all classifications were correct and an accuracy of 100% was reached. On average, the accuracy for the task identification was 93.1% ± 11.5%.

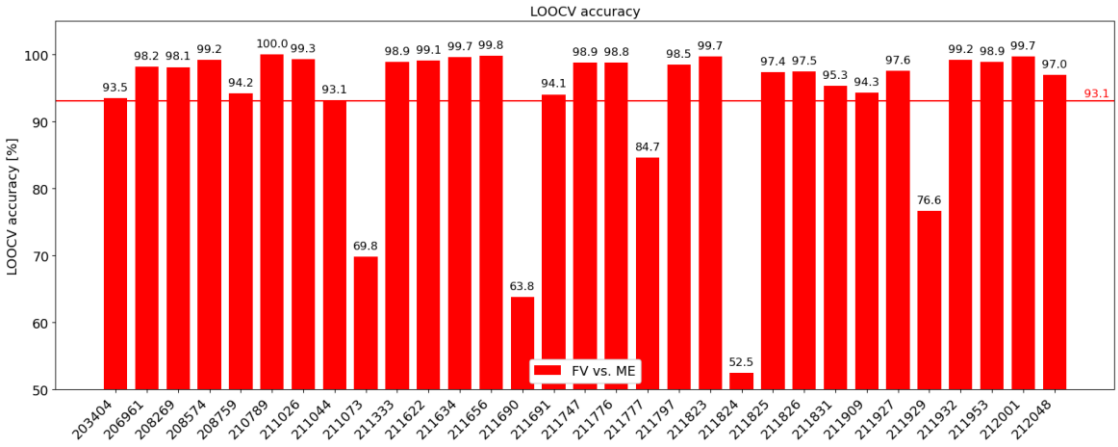

Figure 28: LOOCV accuracy scores of the ROCKET classifier for the identification of the task based on object fixations. The labels on the x-axis indicate whose data was used as the test dataset. The horizontal line indicates the average accuracy value.

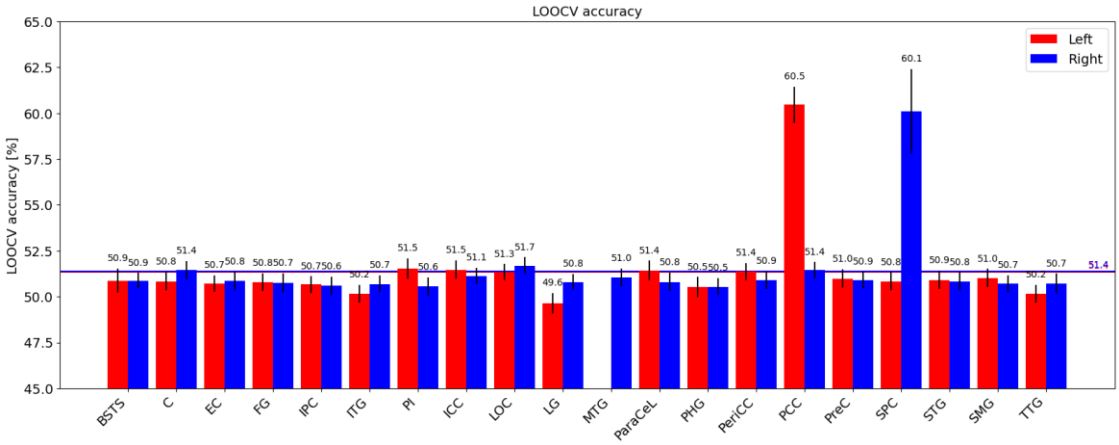

Figure 29: LOOCV accuracy scores from univariate ROCKET classifiers for the identification of the task based on object fixations. The univariate ROCKET classifiers were trained separately for each individual ROIs. Red bars indicate results for ROIs in the left hemisphere while blue bars indicate results for ROIs in the right hemisphere. The error bars represent the standard error of the mean. The (overlapping) horizontal lines indicate the average accuracy values.

Figure 29 shows the mean classification accuracy scores of univariate ROCKET classifiers for the task identification. The accuracy scores were obtained through LOOCV. Each individual univariate classifier was trained and tested on the ROI time courses of a single ROI. While for most ROIs the average accuracy was below 52%, two ROIs stood out with an average accuracy of approximately 60%, the left PCC and the right SPC.

9.3.3 Resting-state fingerprinting

Figure 30 shows the ROCKET classification accuracy scores for the resting-state data that were achieved by leaving out a specific subject from the training and testing datasets. The accuracy scores for the case of training on the first measurement and testing on the second measurement were always lower than for the opposite case where the ROCKET classifier was trained on the second measurement and tested on the first measurement. For the first case, the lowest and highest accuracy scores achieved were 91.3% and 94.5%, respectively. On average the accuracy score was 92.2% ± 0.8%. For the second case, the lowest and highest accuracy scores achieved were 94.2% and 96.6%, respectively, with an average of

94.8% ± 0.6% across all subjects. When taking all accuracies together, the mean was 93.5% ± 1.6%. Given that the chance level was equal to $1/19 = 5.3\%$, the classification accuracy far exceeded the chance level for all combinations.

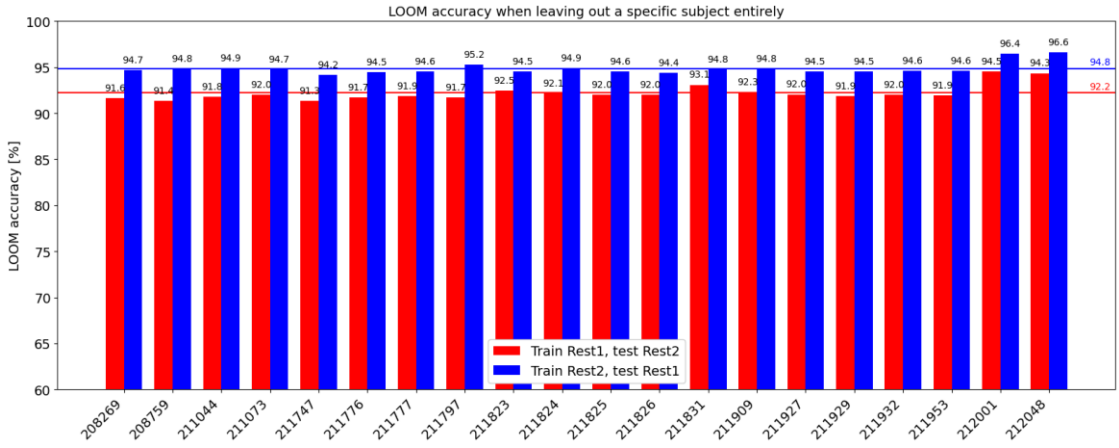

Figure 30: LOOM accuracy scores of the ROCKET classifier for the identification of the subject on resting-state data. The labels on the x-axis indicate which subject was left out from the training and test datasets. Red bars indicate results for training on the first resting-state measurement and testing on the second measurement while blue bars indicate results for training on the second resting-state measurement and testing on the first measurement. The horizontal lines indicate the average accuracy values.

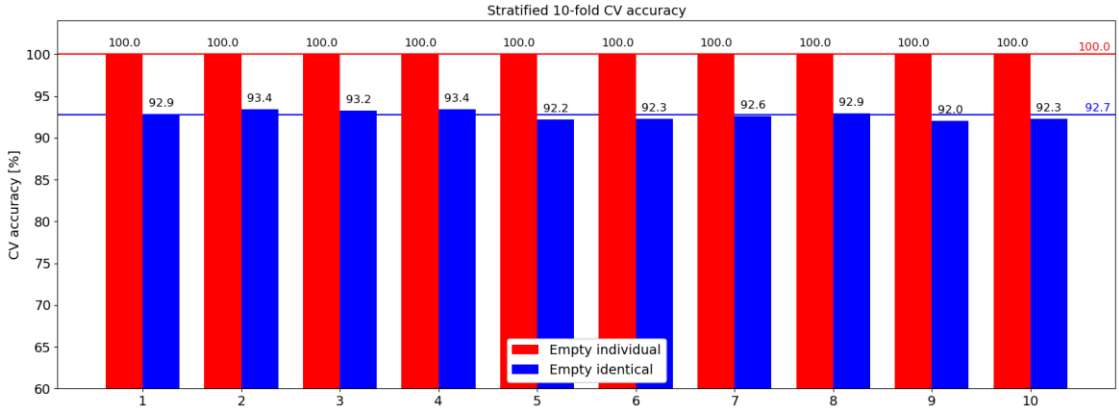

Figure 31: Stratified 10-fold CV accuracy scores of the ROCKET classifier for the identification of the empty-room measurement. Red bars indicate results for the empty-room data projected onto the individual subject source spaces while blue bars indicate results for the empty-room data projected onto an identical source space and with the same head position for all subjects.

Figure 31 shows the stratified 10-fold CV accuracy scores of the ROCKET classifier on the empty-room data. For the empty-room data projected onto the same source space and with identical head positions (blue bars), the lowest and highest accuracy scores achieved were 92.0% and 93.4%, respectively. On average the accuracy score was 92.7% ± 0.5%. When the empty-room data was projected onto the individual source spaces with individual head positions, the ROCKET classifier achieved perfect classification accuracies of 100% on all 10 test sets (red bars).

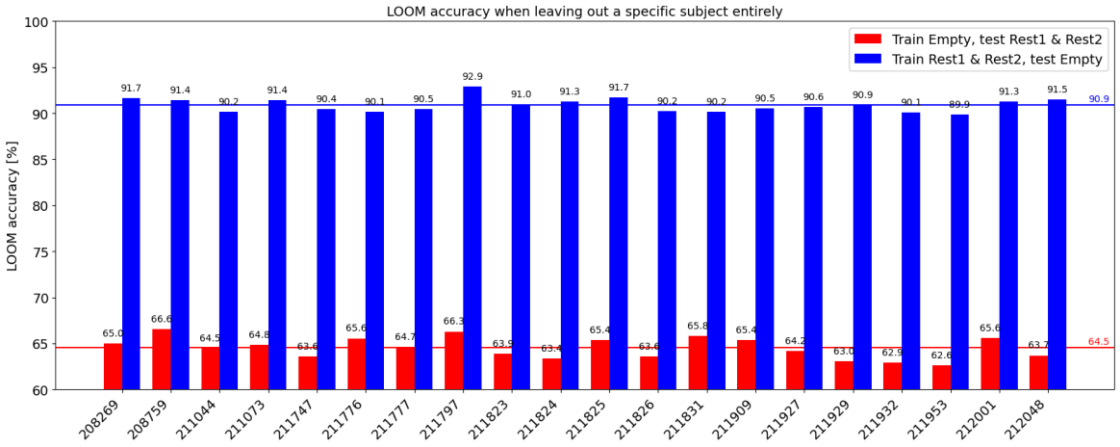

Figure 32: LOOM accuracy scores of the ROCKET classifier for the identification of the subject on resting-state data vs. empty-room data. The labels on the x-axis indicate which subject was left out from the training and test datasets. Red bars indicate results for training on the empty-room data and testing both measurements of the resting-state data while blue bars indicate results for training on the resting-state measurements and testing on the empty-room data. The horizontal lines indicate the average accuracy values.

Figure 32 shows the LOOM accuracy scores of the ROCKET classifier on the cross-over of resting-state and empty-room data. The accuracy scores for the case of training on the empty-room data and testing on the resting-state measurement were always lower than for the opposite case where the ROCKET classifier was trained on the resting-state data and tested on the empty-room data. For the first case, the lowest and highest accuracy scores achieved were 62.6% and 66.6%, respectively. On average the accuracy score was 64.5% ± 1.1%. For the second case, the lowest and highest accuracy scores achieved were 89.9% and 92.9%, respectively, with an average of 90.9% ± 0.7% across all subjects.

9.4 Discussion

(Multivariate) time series classification has many exciting applications in neuroscience and medicine which range from brain-computer interfaces (BCIs) to the diagnosis of medical conditions. Two such applications were tested in this chapter using ROCKET: the discrimination of the behavioral task based on recordings of the FRA and neural fingerprinting, i.e., the discrimination between subjects based on resting-state recordings. The behavioral task could be identified with 93.1 % accuracy while the correct subject could be determined with 93.5 % accuracy. However, just using empty-room recordings of the background noise, similar fingerprinting accuracies could be achieved.

9.4.1 Task identification

The ROCKET classifier was trained on multivariate FRA ROI time courses of object fixations during FV and ME with the purpose of identifying the experimental task during which the fixations were performed. Similarly, a univariate ROCKET classifier was trained separately for each ROI and TCPT was applied to contrasts of the averaged FRA ROI time courses to highlight ROIs with significant differences in temporal dynamics.

Using the multivariate ROCKET classifier, the overall accuracy of 93.1% of identifying the correct task far exceeded chance level. However, Figure 28 also implies that there can be significant inter-subject variability. While the classification accuracy was considerably higher than 90% for most subjects in the LOOCV, there were five subjects where the accuracies ranged from only 52.5% to 84.7%. This shows that for one subject in particular, the patterns learned from its peers were not sufficiently predictive of the task. More data will be necessary to address the questions of 1) how prevalent these outliers are in the general population and 2) if a greater variation of subjects in the training datasets can improve the classification accuracies for these outliers.

Nonetheless, it is remarkable that ROCKET was able find differentiating patterns in single epochs of only 160 ms length. Furthermore, instead of the more complicated setup of MEG with source localization, one could also train the classifier on signals obtained through EEG, which could make ROCKET a viable component for BCIs (Abiri et al. 2019). Important requirements for BCIs are that they work in real time and that the delay between brain signal and execution of the action function can be minimized, which are easily fulfilled with ROCKET since 1) the time series required for classification are extremely short and 2) once the classifier has been trained, the brain signals can be decoded quickly. It takes approximately 240 ms to compute the transformed features for a single epoch and to identify the task.

Training individual ROCKET classifiers for each ROI showed that taking the multivariate nature of the brain recordings into account is an important factor for high classification accuracies. For two regions, the left PCC and the right SPC, the univariate classification accuracy significantly exceeded the chance level ($p < 0.01$) but on their own none of these classifiers could reach accuracies higher than 60.5%. Furthermore, the right SPC was the only ROI where significant differences between ROI time courses during FV and ME could be found (cf. section 9.3.1). These results suggest that not all information critical to the task differentiation is reflected by the averaged ROI time courses since the univariate classification accuracy for the left PCC was slightly higher than that of the left SPC. While significant differences in the time courses themselves could not be identified, the average activity in the left PCC was lower for ME as compared to FV (result not shown).

Similar to the SMG, the SPC (in vicinity to the intra-parietal sulcus) has also been associated with the detection of behaviorally relevant stimuli and top-down control (Corbetta and Shulman 2002; Vilberg and Rugg 2008), which could explain stronger activity during ME object fixations. Furthermore, while not directly involved in the retention of information in working memory, the SPC was found to be critical for its manipulation (Koenigs et al. 2009). These processes could explain the enhanced discriminability between the tasks based on the right SPC. The enhanced discriminability based on the left PCC is less clear. The PCC is said to be a central node in the default mode network (Leech and Sharp 2014), which could be suppressed more strongly during ME due to the need for attention when memorizing the objects.

In summary, it is possible to differentiate the brain activity between subjects freely viewing and memorizing objects. The high accuracy and the fact that only 160 ms of

single-epoch data were necessary make ROCKET a promising candidate for further research with respect to BCIs.

9.4.2 RESTING-STATE FINGERPRINTING

The ROCKET classifier was trained independently on multivariate FRA ROI time courses from two measurements of resting-state data recorded from the same set of subjects. One resting-state measurement was used as the training dataset while the other measurement was used as the test dataset. The goal was to identify the subject for each epoch in the respective test dataset. This is a task also known as neural fingerprinting.

The overall classification accuracy estimated using LOOM for all combinations of subjects and training measurements was far exceeding the chance level. An interesting aspect is that training on the second resting-state measurement and applying the classifier to the first measurement always led to higher classification accuracies than the other way round. First of all, this shows that the two measurements are not equivalent. Performing the active vision tasks is quite exhausting and may affect the subsequent resting-state recording. Switching from performing the tasks to resting may not be possible in such a short time span even if the first minute of each resting-state recording was discarded. Second, there might have been additional differentiating factors in the data from the second measurement that could not be learned from the first measurement. Nonetheless, the results show that patterns learned on data from one measurement can generally be transferred to data from a different measurement that was recorded within a relatively short span of time (~one hour). However, it is important to note that the position of the MEG scanner was usually not changed between these measurements. In isolation, Figure 30 gives the appearance of the ROCKET classifier being a feasible option for performing fingerprinting on single-epoch time series.

Unfortunately, the fingerprinting results for the empty-room data put this into question. When using the individual source spaces and head positions for the projection onto the source space, ROCKET reached perfect classification accuracies of 100% on all 10 folds. Furthermore, even when projecting the empty-room data onto an identical source space with the same head position, the ROCKET classifier was able to identify for single epochs the empty-room measurement with 92.7% accuracy. In fact, similar accuracies could also be reached in the sensor space when skipping the source localization (data not shown). This difference in classification accuracies between the two source localization methods suggests that the individual brain anatomy or the head position in the MEG system indeed may have an impact on the classification as suggested by da Silva and colleagues (da Silva Castanheira et al. 2021a).
Moreover, it was possible to transfer patterns learned on empty-room data and achieve a fingerprinting accuracy of almost 65% on resting-state data. Similarly, patterns learned on resting-state data could be transferred to empty-room data to achieve an even higher accuracy of closer to 91%. Consequently, the background noise, which was recorded in isolation in the empty-room measurements, is a relevant factor in identifying the subject of a given recording. This could potentially be an effect of individual anatomical features or the head position. Nonetheless, it is

also clear that patterns learned from the background noise on their own do not suffice to explain the significantly higher ($p << 0.001$) fingerprinting accuracy when training and testing on the two resting-state measurements.

In summary, these results give a first indication that subject differentiation can, in principle, be achieved directly on brain recordings as short as 1.2 s using ROCKET. This would greatly simplify current procedures where second-order statistical measures such as functional connectomes are used (Sareen et al. 2021). However, more data is needed to reach a final conclusion. First, more subjects have to be acquired as it is common to use much larger cohorts in fingerprinting studies (Sareen et al. 2021; da Silva Castanheira et al. 2021a) and, perhaps much more importantly, multiple measurements over a long span of time are needed for each subject as the ROCKET classifier would then be forced to learn patterns that are independent of the day-to-day variations in the background noise. This would help to quantify how much of the fingerprinting accuracy achieved here can be attributed to discriminating features in the brain signals and in the background noise.

9.5 Conclusion

To my knowledge, this is the first time that ROCKET has been applied to MEG signals. Using ROCKET, it could be identified whether object fixations were performed during the FV task or during the ME task. In other words, ROCKET was able to find differentiating patterns in the time series that were specific to the two tasks. Astoundingly, only 160 ms of single-epoch MEG recordings were required to achieve a classification accuracy of over 93%. The high classification accuracy and the need for relatively short segments of single-epoch data make ROCKET a promising candidate for BCI research. However, in the current state more data will be needed to investigate the influence of limiting factors such as inter-subject differences on the classification accuracy. Furthermore, using ROCKET it was possible to differentiate between subjects based on short segments of single-epoch resting-state data with accuracies over 93%. However, these results are potentially confounded by day-to-day variations in the background noise as 1) it was possible to distinguish between empty-room recordings with the same methodology, and 2) it was possible to transfer patterns learned on empty-room data to resting-state recordings and vice versa. Multiple recordings from different days will be necessary to investigate the influence of the background noise. Nevertheless, the results are promising and motivate further research into the application of ROCKET to MEG recordings.

10 GENERAL DISCUSSION AND OUTLOOK

In this dissertation, MEG and eye tracking were combined to form a comprehensive record of the visual system with the purpose of studying the visual processing during several naturalistic tasks.

Several studies have shown that the brain behaves differently under naturalistic conditions as compared to artificial scenarios (Kamienkowski et al. 2012; Kaunitz et al. 2014; F. F. Li et al. 2003; Ossandón et al. 2010; Snow et al. 2011; Snow and Culham 2021; Sonkusare, Breakspear, and Guo 2019; Vinje and Gallant 2000; Wolfe 1994b), and, as a result, the study of naturalistic images is the logical progression from the simplified artificial stimuli for furthering our understanding of the visual system and the brain as a whole. However, the analysis of such naturalistic experiments comes with an additional layer of complexity. For example, when subjects are exploring photographs using sequences of eye movements and fixations, as was required for the experiments performed in this dissertation, it is unlikely that any two sequences would ever be the same. Therefore, trials are generally not directly comparable.

This is where the aforementioned combination of eye-tracking data and neuroimaging proved to be an effective tool for studying such unrestricted behavior. The eye-tracking system allowed for the inference of what was being processed at exactly which points in time while the MEG recordings captured the associated activity in the brain. The analysis of the behavioral data (chapter 7) showed that the general setup of the experiment was adequate. Previously published results regarding eye movement statistics for active vision were replicated (Nikolaev, Meghanathan, and van Leeuwen 2016; Jo, Kellermann, et al. 2019). Similarly, the task performance was satisfactory. Since the performance during the search task depends on the eye-tracking accuracy (section 7.4.3), this may also serve as an indicator for an acceptable level of quality of the eye-tracking data for the individual subject recordings. However, the bias in the first second of the image presentation, most likely because of illumination changes, could potentially be eliminated (section 7.3.1). For future eye-tracking studies it is strongly recommended that the illumination level remains constant over the course of the entire presentation. Specifically, all images and objects should be adjusted to have the same average brightness and grey backgrounds with the same level of brightness should then be used for the eye tracker calibration and the presentation of fixation crosses, search targets, etc.

The goal of the whole-brain causality analysis was to discern differences in visual processing during the free viewing and the guided visual searching of naturalistic images (photographs). Specifically, earlier reports pointed towards a potential central role of the temporoparietal junction (consisting of the SMG and the STG) during the shifting of attention to behaviorally relevant stimuli (Shulman et al. 2007; Corbetta, Patel, and Shulman 2008) and target detection (Linden et al. 1999; Shulman et al. 2010). Both aspects were substantiated and extended by the analysis of the fixation-related evoked activity.

The temporoparietal junction formed a cluster of significant activity together with the TTG and the PI and causal interactions were enhanced for the entire cluster during guided visual searching as compared to the free viewing. This led to the conclusion that not just the temporoparietal junction but all four regions (SMG, STG, TTG, and PI) are involved in shifting attention to behaviorally relevant locations.
Of particular importance was a connection from the right SMG to the right SEF, which was interpreted as providing information for updating the search priority map guiding the eye movements to the locations most likely to contain the search target. Furthermore, a significant, negative correlation between the search response time and the activity of the right SMG during the first target fixation in a trial suggested that the right SMG facilitates the integration of visual input for target recognition. These novel results provided new insights on the mechanisms of how the SMG interacts with other regions for attention shifting and target recognition.
There has been evidence that there is a differential response of some brain regions to stimuli appearing in different hemifields (cf. section 8.4.1). In this dissertation, potential effects of such differential processing were not discussed in depth. However, in the future, these differential responses could also be studied in the context of active vision by separating fixations based on whether they were to the left or the right of the preceding fixation. New insights into the spatial selectivity of the brain could be gained.

Finally, it was shown that ROCKET, a method for the classification of multivariate time series, can be applied to the fixation-related evoked activity to differentiate between object fixations performed during the free viewing and the memory task. Furthermore, it was generally possible to distinguish between subjects based on ROCKET applied to resting-state data even though open questions regarding the effects of background noise on the classification accuracy remain. However, longitudinal data, i.e., multiple recordings of the same subjects over a longer time span, would be required to answer these questions. Nonetheless, this was, to my knowledge, the first time that neural fingerprinting was achieved based on single-epoch time series recordings instead of second order statistics such as correlation matrices or connectivity measures. Previous MEG publications reached resting state classification accuracies of 94.9–96.2% at epoch lengths of 30 s (da Silva Castanheira et al. 2021a), 93.0–95.3% for healthy controls at epoch lengths of 30s (da Silva Castanheira et al. 2021b), and 94.5–98.1% at epoch lengths of 8 s (Sareen et al. 2021). ROCKET is able to achieve more or less comparable accuracies, albeit at the lower end of the spectrum. However, the amount of data needed for the classification of a single epoch is considerably lower with 1.2 s.
Without a doubt, multivariate time series classification holds exciting prospects for future neuroscience research. Since the task classification using ROCKET only required short segments of 160 ms length, it is conceivable that ROCKET could be used in conjunction with EEG for brain-computer-interfaces controlling prosthetics or even vehicles. But there could also be clinical applications: for example, one could train ROCKET-based tools for distinguishing patients from healthy subjects to aid in the diagnosis of autism spectrum disorder or depression.

In summary, this dissertation furthered the understanding of the neurological process of active vision and the role of the temporoparietal brain region during active vision. Furthermore, the particular importance of the right SMG during

guided visual searching was emphasized. ROCKET proved to be an exciting prospect for many applications including brain-computer-interfaces, neural fingerprinting, and medical diagnosis.

11 APPENDIX

11.1 MATHEMATICAL OPERATORS

11.1.1 THE KRONECKER PRODUCT[19]

Let $\mathbf{A} = (a_{ij})$ and $\mathbf{B} = (b_{ij})$ be two matrices of dimensions $(m \times n)$ and $(m \times n)$, respectively.
Then the Kronecker product or direct product of **A** and **B** is defined as:

$$\mathbf{A} \otimes \mathbf{B} := \begin{pmatrix} a_{11}\mathbf{B} & \cdots & a_{1n}\mathbf{B} \\ \vdots & & \vdots \\ a_{m1}\mathbf{B} & \cdots & a_{mn}\mathbf{B} \end{pmatrix}, \tag{11.1}$$

where $\mathbf{A} \otimes \mathbf{B}$ is an $(mp \times nq)$ matrix. The following, non-exhaustive list of properties is useful for the computation of the least squares estimate in section 4.2.3:

- $\mathbf{A} \otimes \mathbf{B} \neq \mathbf{B} \otimes \mathbf{A}$ for
- $(\mathbf{A} \otimes \mathbf{B})^T = \mathbf{A}^T \otimes \mathbf{B}^T$
- $(\mathbf{A} \otimes \mathbf{B})^{-1} = \mathbf{B}^{-1} \otimes \mathbf{A}^{-1}$ if **A** and **B** are invertible
- $(\mathbf{A} \otimes \mathbf{B})(\mathbf{C} \otimes \mathbf{D}) = \mathbf{AC} \otimes \mathbf{BD}$

11.1.2 THE COLUMN STACKING OPERATOR[20]

Let $\mathbf{A} = (\boldsymbol{a}_1, \ldots, \boldsymbol{a}_n)$ be an $(m \times n)$ matrix consisting of n column vectors $\boldsymbol{a}_i$ of length of dimensions $(m \times 1)$. The vec operator stacks the columns of **A**, transforming it into an $(mn \times 1)$ matrix:

$$\mathrm{vec}(\mathbf{A}) := \begin{bmatrix} \boldsymbol{a}_1 \\ \vdots \\ \boldsymbol{a}_n \end{bmatrix}. \tag{11.2}$$

The following, non-exhaustive list of properties is useful for the computation of the least squares estimate in section 4.2.3:

- $\mathrm{vec}(\mathbf{A} + \mathbf{B}) = \mathrm{vec}(\mathbf{A}) + \mathrm{vec}(\mathbf{B})$
- $\mathrm{vec}(\mathbf{AB}) = (\mathbf{I} \otimes \mathbf{A})\mathrm{vec}(\mathbf{B}) = (\mathbf{B}^{\boldsymbol{T}} \otimes \mathbf{I})\mathrm{vec}(\mathbf{A})$

11.2 BEHAVIORAL ANALYSIS

Figure 33 depicts the probability distribution of fixation durations for fixations on objects during the image presentation. The average fixation duration was highest for free viewing with approximately 261.99 ± 136.82 ms followed by the memory task with 247.08 ± 129.32 ms and the search task with 215.79 ± 101.50 ms. The

[19] The information in this section was taken from the appendix A.11 in (Lütkepohl 2005).
[20] The information in this section was taken from the appendix A.12 in (Lütkepohl 2005).

mean values of the three distributions were significantly different ($p < 0.05$) from one another after Bonferroni-correction for multiple comparisons.

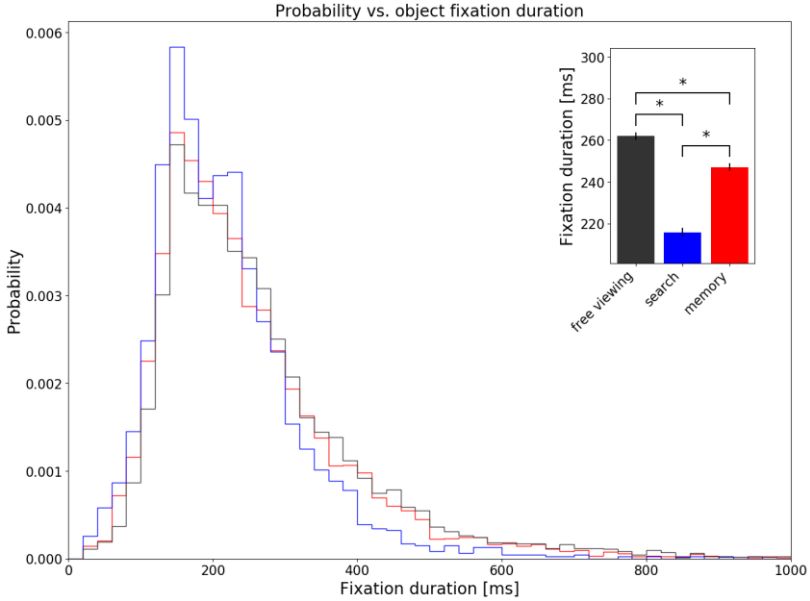

Figure 33: The probability distribution of fixation durations for fixations on objects during the image presentation (free viewing: black, search: blue, memory: red). In the top right corner is the average fixation duration by task with the small black bars being the standard error of the mean. The asterisk '*' indicates significant differences ($p < 0.05$) in the mean after Bonferroni-correction.

There are two ways to compute the distance that a saccade travelled. First, one can simply calculate the linear distance between the starting point and the end point of the saccade. However, saccades are often not simply straight lines, but they can be curved. It is for example possible for a saccade to suddenly change direction without having performed a fixation first. Therefore, one can also define saccade distance as the length of the path the saccade travelled along. This distinction can be particularly important when looking at saccade distance in conjunction with saccade duration.

Figure 34 depicts the average start-to-end distance of saccades in each of the four major directional quadrants, i.e., if 0° corresponds to upwards directed saccades, then saccades between ±45° were pooled together and their average was taken. The error bars represent the standard error of the mean. In all four directions, saccade distances were greatest for the search task, followed by the memory task and then by the free viewing task. Saccades in the horizontal quadrants travelled, generally, further than saccades in the vertical quadrants. Saccade distances during the fixation cross were on average below 2° of visual angle and as such a lot shorter compared to the task-related saccades.

Instead of using the onset time of the saccades, a related analysis is to use the order in which the saccades occurred during the image presentation. Figure 35 shows the probability distribution of saccade direction for the first 20 saccades following image onset. The results were very similar to the ones in Figure 14. For the first three saccades, there was a bias towards the left, which disappeared for the later saccades. However, when looking at saccades during the fixation cross presentation it becomes clear that there was only a distinct bias towards the left for the first

saccade. For later saccades the chance of a leftward vs. a rightward saccade was closer to 50:50 (Figure 36).

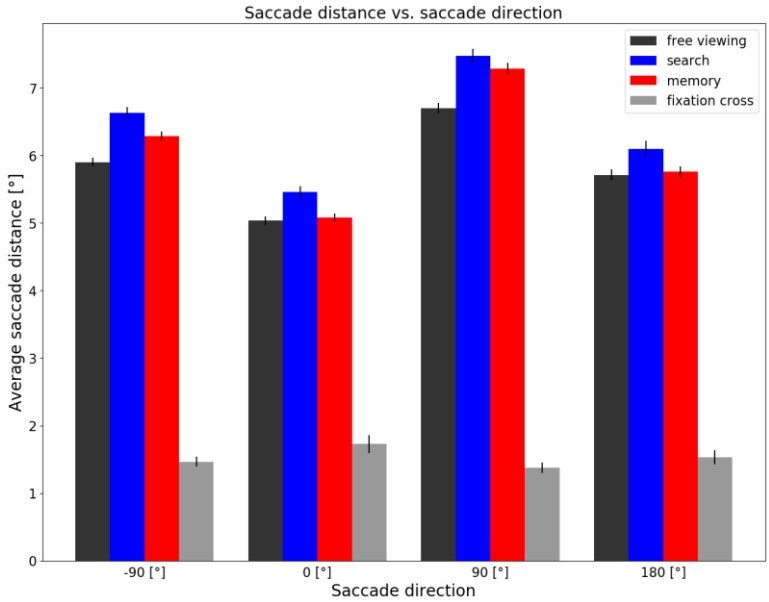

Figure 34: Saccade distance (starting point to end point) in degree of visual angle in dependance on the saccade direction. Saccades in the four major quadrants were pooled together and the distance between onset and offset was averaged. The error bars represent the standard error of the mean.

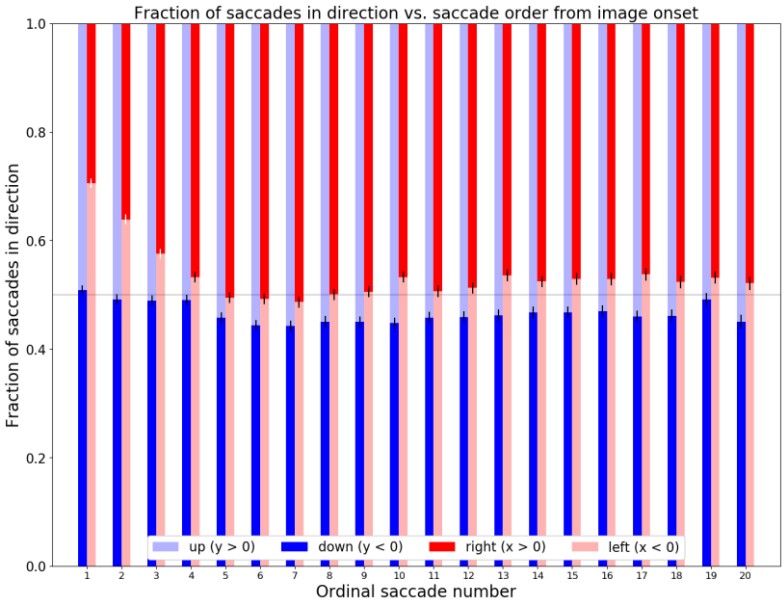

Figure 35: Fraction of saccades in a given direction (up vs. down and left vs. right) dependent on the order in which the saccades were performed during the image presentation. The error bars represent the standard error of the mean. White error bars indicate a significant deviation ($p = 10^{-7}$) from a binomial distribution with probability $p = 0.5$ after using the Bonferroni-correction.

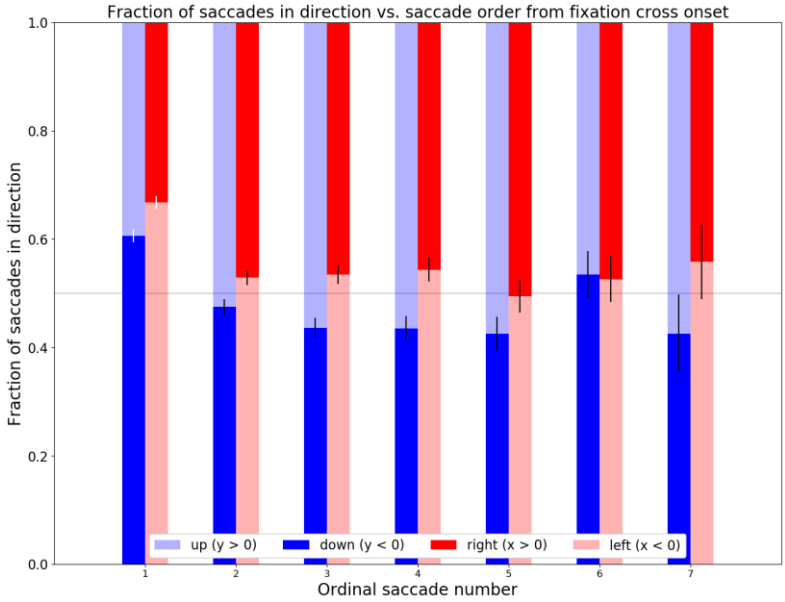

Figure 36: Fraction of saccades in a given direction (up vs. down and left vs. right) dependent on the order in which the saccades were performed during the fixation cross presentation. The error bars represent the standard error of the mean. White error bars indicate a significant deviation ($p = 10^{-7}$) from a binomial distribution with probability $p = 0.5$ after using the Bonferroni-correction.

11.3 MEG PREPROCESSING

11.3.1 ALIGNMENT OF MEG AND EYE TRACKING DATA

A good alignment of two simultaneously recorded time series can be achieved if the sampling frequencies are stable in both systems and if there is no delay between registering common events, which were used to align time recordings. These two aspects were investigated here.

To check whether the sampling rates for both recordings were stable and did not fluctuate, common events in the eye-tracking and MEG data were extracted on a per-trial basis. The number of samples was adjusted for the events so that the first common event was assigned the number zero for the sample number both in the eye-tracking data and in the MEG data. Then, a linear regression was computed for the number of MEG/ECG/EOG samples vs. the number of eye-tracking samples (Figure 37).

Then the recordings were checked for a constant delay between the two systems. While the eye tracker recorded the eye position directly, the horizontal and vertical EOG channels measured the activity of the muscles moving the eyes. For each trial, the cross correlation between the *x*- and *y*-position given by the eye tracker and the horizontal and vertical EOG channels, respectively, was computed. The cross correlations were averaged across trials and then the offset between the EOG recording and the eye tracker recording was computed for each recording run. The offset was defined as the displacement between the two time series, which maximizes the average cross correlation, i.e., the offset is the delay which produces the best alignment between the two time series. In the absence of a constant delay

between the two recordings, the maximum of the cross correlation should be at an offset of zero (Figure 38).

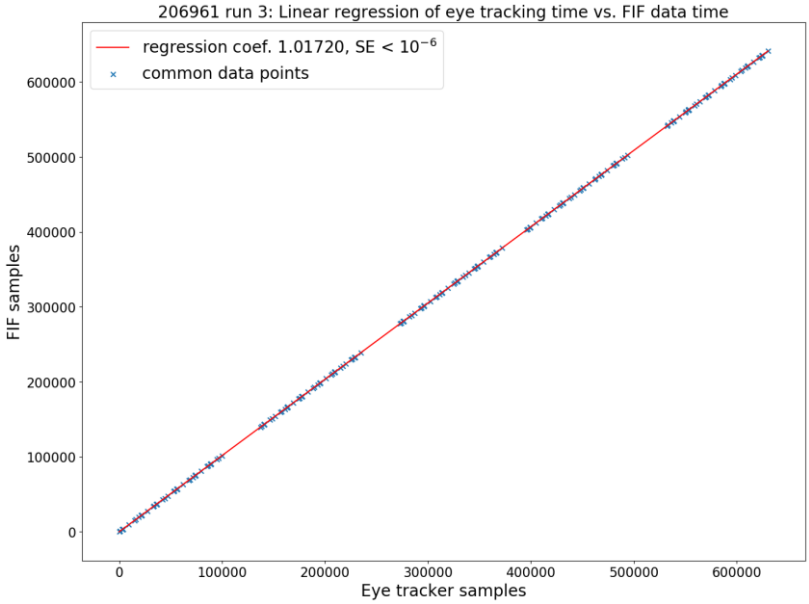

Figure 37: Alignment of sample numbers of common events found in the MEG/ECG/EOG recording (FIF-file) and in the eye-tracking recording for the third recording run of subject 206961. The slope of the linear regression was 1.01720 and the standard error of the regression (SE) was less than 10^{-6}.

The alignment of sample numbers for common events in both recordings, revealed a linear trend in the data with a slope of 1.01720 (see Figure 37 as an example). This was true for all subjects and recordings. During the experiment, the 30 trials were split into five blocks of six trials each. Each block of trials was followed by the calibration procedure of the eye tracker. This pattern of five blocks interrupted by the calibration can be seen in Figure 37.

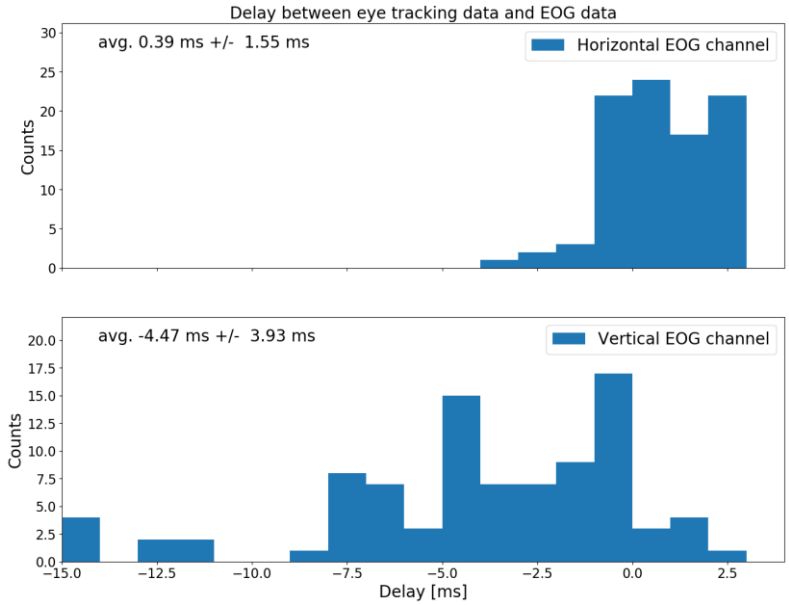

Figure 38: Histograms of the delay between the horizontal EOG channel and the x-coordinate of the gaze position (top) and of the delay between the vertical EOG channel and the y-coordinate of the gaze position (bottom). The offset (delay) was computed separately for each subject and run based on the cross correlation averaged across trials.

The offsets (delays) maximizing the alignment of EOG channels and eye-tracking data are depicted in Figure 38. For the horizontal EOG channel and the x-coordinate of the gaze position, the delays are strongly concentrated around zero. The average offset between the two time series was 0.39 ± 1.55 ms. However, there was a bias towards offsets for the vertical EOG channel and the y-coordinate of the gaze position. A broader distribution with an average offset of −4.47 ± 3.93 ms could be observed. Negative offsets indicate that the eye-tracking data preceded the EOG recording.

11.3.2 DENOISING

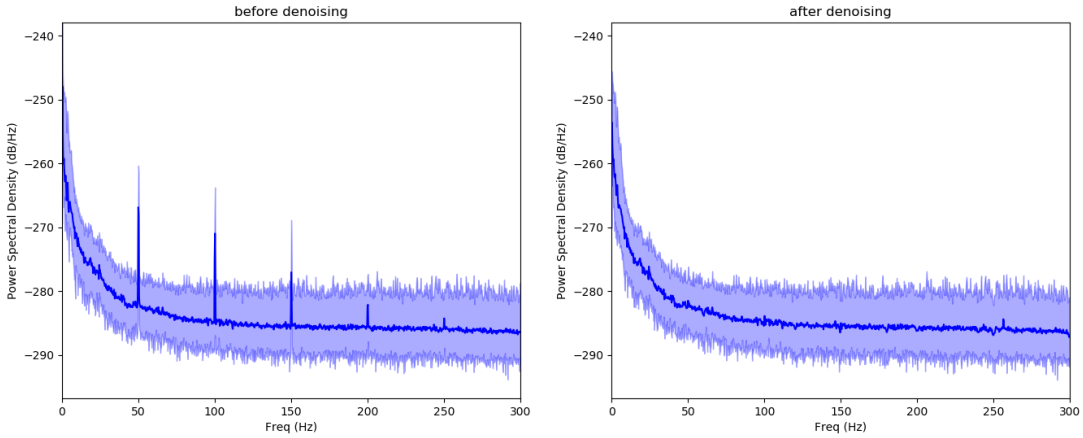

Figure 39: Power spectral density before and after denoising (example from subject 211909, run 1). Power line noise at 50 Hz plus harmonics was removed by applying anti-notch filters to the reference channels and by subtracting the filtered reference signal from the signal channels.

11.4 ROI IDENTIFICATION

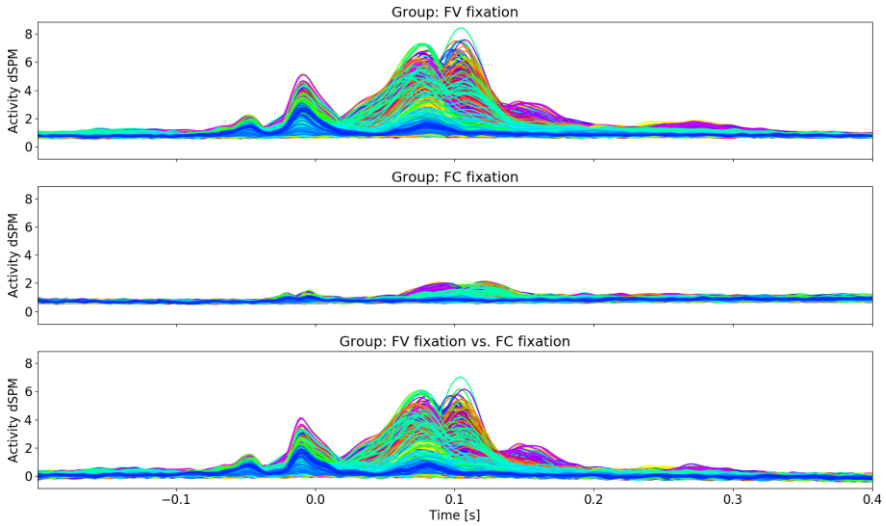

Figure 40: Grand average of FRA across subjects and epochs for fixations during free viewing task (top), fixations during the fixation cross presentation (middle) and the contrast (bottom).

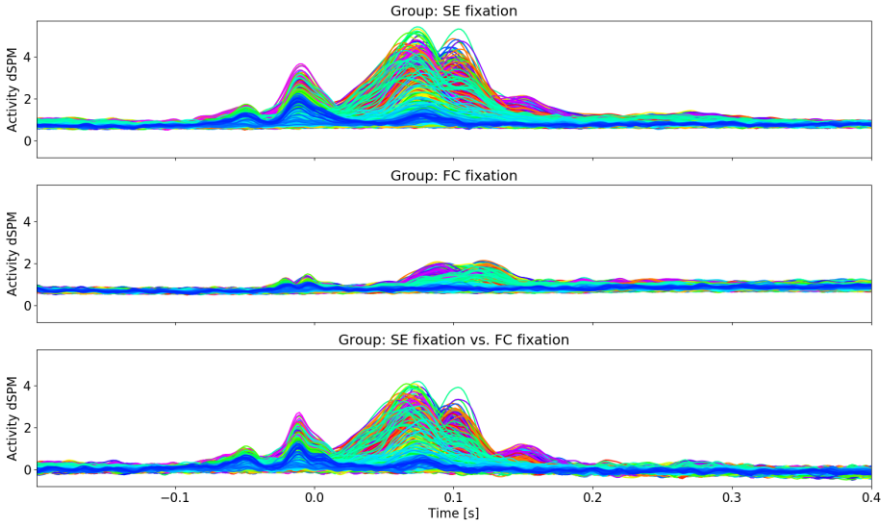

Figure 41: Grand average of FRA across subjects and epochs for fixations during search task (top), fixations during the fixation cross presentation (middle) and the contrast (bottom).

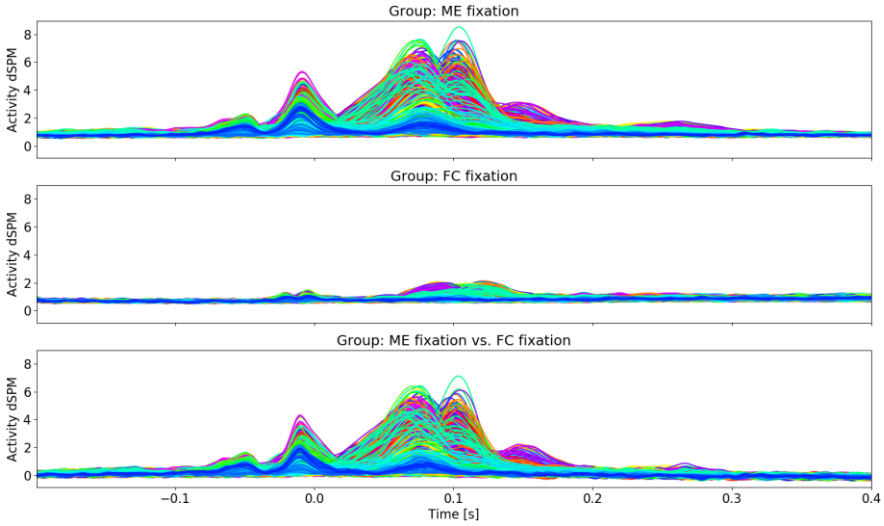

Figure 42 : Grand average of FRA across subjects and epochs for fixations during memory task (top), fixations during the fixation cross presentation (middle) and the contrast (bottom).

For ME, five clusters were found in total. Four clusters were, up to a few vertices, identical to the clusters found during the free viewing task. However, there was an additional cluster which overlapped with areas already covered by the dorsal cluster. This additional cluster is referred to as the dorsal stream cluster as it covered the pericalcarine cortex (#17), the cuneus (#16), and the precuneus (#5). This cluster was active during a comparatively late time interval between approximately 125 and 175 ms from fixation onset (Figure 21).

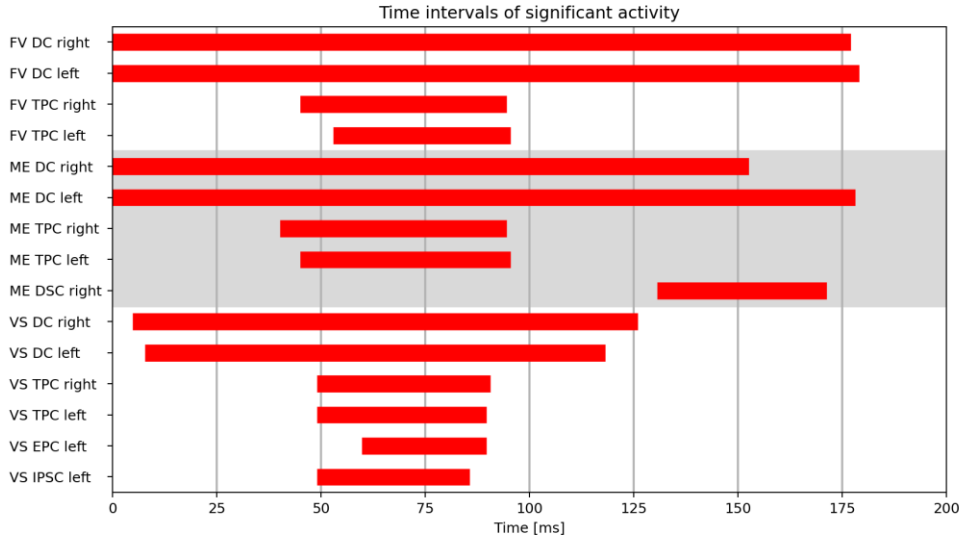

Figure 43: Time intervals with significant activity during FV, ME, and VS based on the SCPT clusters (DC: dorsal cluster, TPC: temporoparietal cluster, IPSC: intraparietal sulcus cluster, EPC: entorhinal-parahippocampal cluster, DSC: dorsal stream cluster) with fixation onset at t = 0 ms during FV and VS. Figure adapted from (Kiefer et al. 2022). Copyright 2022 by Kiefer et al.

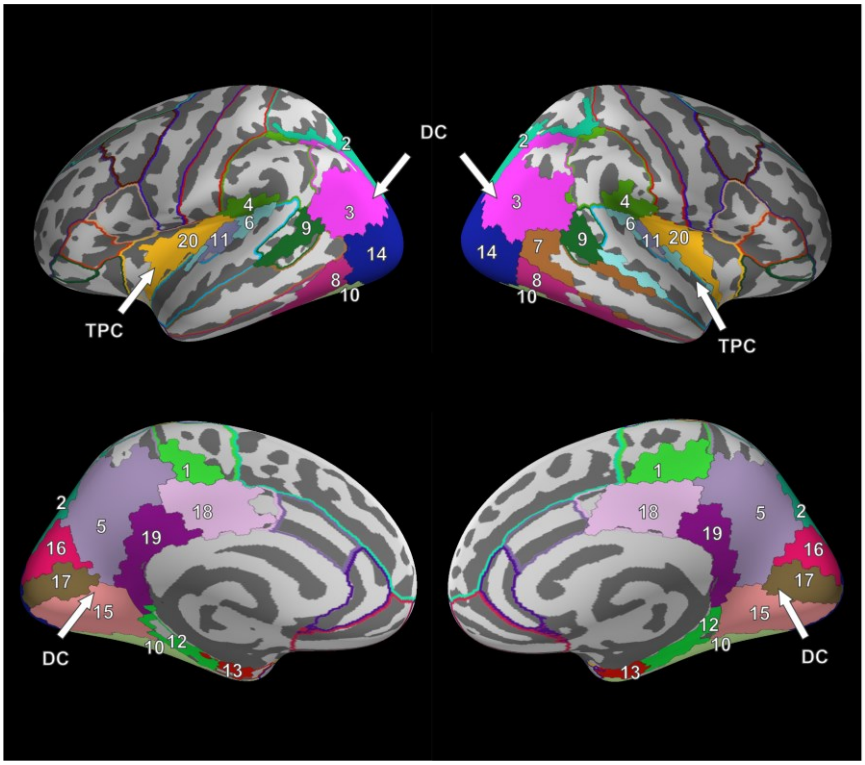

Figure 44: ME cluster results for the contrast of FRA during the image presentation versus FRA during the fixation cross presentation (DC: dorsal cluster, TPC: temporoparietal cluster). Separate ROIs are highlighted in different colors according to the Desikan-Killiany atlas (Desikan et al. 2006). Table 2 lists the ROIs corresponding to the numbers.

Table 2: Regions of interest (ROIs) exhibiting significant FRA differences for the image-fixation and fixation-cross-fixation contrasts. For each ROI, the MNI coordinates from the vertices with maximum activity are presented. The dash '-' indicates that no significant differences in FRA were found. TPC regions are marked in bold. Table adapted from (Kiefer et al. 2022). Copyright 2022 by Kiefer et al.

ROI	#	Anatomical label	Free Viewing (FV) ROI MNI coordinates		Visual Search (VS) ROI MNI coordinates		Memory (ME) ROI MNI coordinates	
			Left hemi.	Right hemi.	Left hemi.	Right hemi.	Left hemi.	Right hemi.
Frontal lobe								
ParaCeL	1	Paracentral lobule	-17, -31, 43	18, -42, 43	-	18, -42, 43	-17, -31, 43	18, -42, 43
Parietal lobe								
SPC	2	Superior parietal cortex	-8, -90, 25	14, -81, 32	-8, -90, 25	14, -81, 32	-8, -90, 25	11, -90, 21
IPC	3	Inferior parietal cortex (angular gyrus)	-29, -81, 13	33, -75, 18	-29, -81, 13	40, -67, 13	-29, -81, 13	33, -75, 18
SMG	**4**	**Supramarginal gyrus**	**-36, -36, 18**	**40, -36, 18**	**-**	**40, -36, 18**	**-36, -36, 18**	**40, -36, 18**
PreC	5	Precuneus	-21, -61, 9	20, -56, 9	-21, -61, 9	17, -55, 14	-21, -61, 9	20, -56, 9
Temporal lobe								
STG	**6**	**Superior temporal gyrus**	**-38, -37, 11**	**40, -35, 13**	**-**	**1, -16, 23**	**-42, -40, 16**	**40, -35, 13**
MTG	7	Middle temporal gyrus	-	49, -59, 6	-	49, -59, 6	-	49, -59, 6
ITG	8	Inferior temporal gyrus	-43, -53, -10	45, -63, -9	-43, -53, -10	45, -63, -9	-43, -53, -10	45, -63, -9
BSTS	9	Banks superior temporal sulcus	-44, -54, 9	46, -46, 10	-48, -53, 6	46, -46, 10	-44, -54, 9	46, -44, 8
FG	10	Fusiform gyrus	-29, -74, -7	27, -74, -7	-29, -74, -13	27, -74, 7	-29, -74, -7	27, -74, -7
TTG	**11**	**Transverse temporal gyri**	**-38, -27, 5**	**44, -21, 5**	**-41, -26, 2**	**44, -21, 5**	**-41, -26, 2**	**44, -21, 5**
EC	12	Entorhinal cortex	-20, -10, -30	21, -11, -29	-22, -22, -23	21, -11, -29	-22, -22, -23	21, -11, -29
PHG	13	Parahippocampal gyrus	-20, -18, -26	23, -17, -28	-20, -18, -26	23, -17, -28	-20, -18, -26	24, -25, -23
Occipital lobe								
LOC	14	Lateral occipital cortex	-16, -97, -2	30, -86, 1	-16, -97, -2	30, -86, 1	-16, -97, -2	30, -86, 1
LG	15	Lingual gyrus	-11, -85, -13	30, -86, 1	-11, -85, -13	17, -62, 1	-11, -85, -13	17, -62, 1
C	16	Cuneus	-10, -73, 19	10, -79, 28	-10, -73, 19	10, -79, 28	-10, -73, 19	10, -79, 28
PeriCC	17	Pericalcarine cortex	-15, -94, 1	18, -94, 0	-15, -94, 1	18, -94, 0	-15, -94, 1	18, -94, 0
Cingulate cortex								
PCC	18	Posterior cingulate cortex	-16, -37, 39	11, -38, 41	-2, -23, 27	5, -28, 27	-2, -23, 27	11, -38, 41
ICC	19	Isthmus cingulate cortex	-14, -51, 4	17, -50, 4	-14, -51, 4	17, -50, 4	-14, -51, 4	17, -50, 4
Insula								
Insula	**20**	**Insula**	**-35, -20, 1**	**35, -19, 11**	**-35, -20, 1**	**34, -19, 7**	**-35, -20, 1**	**34, -19, 7**

11.5 CAUSALITY ANALYSIS

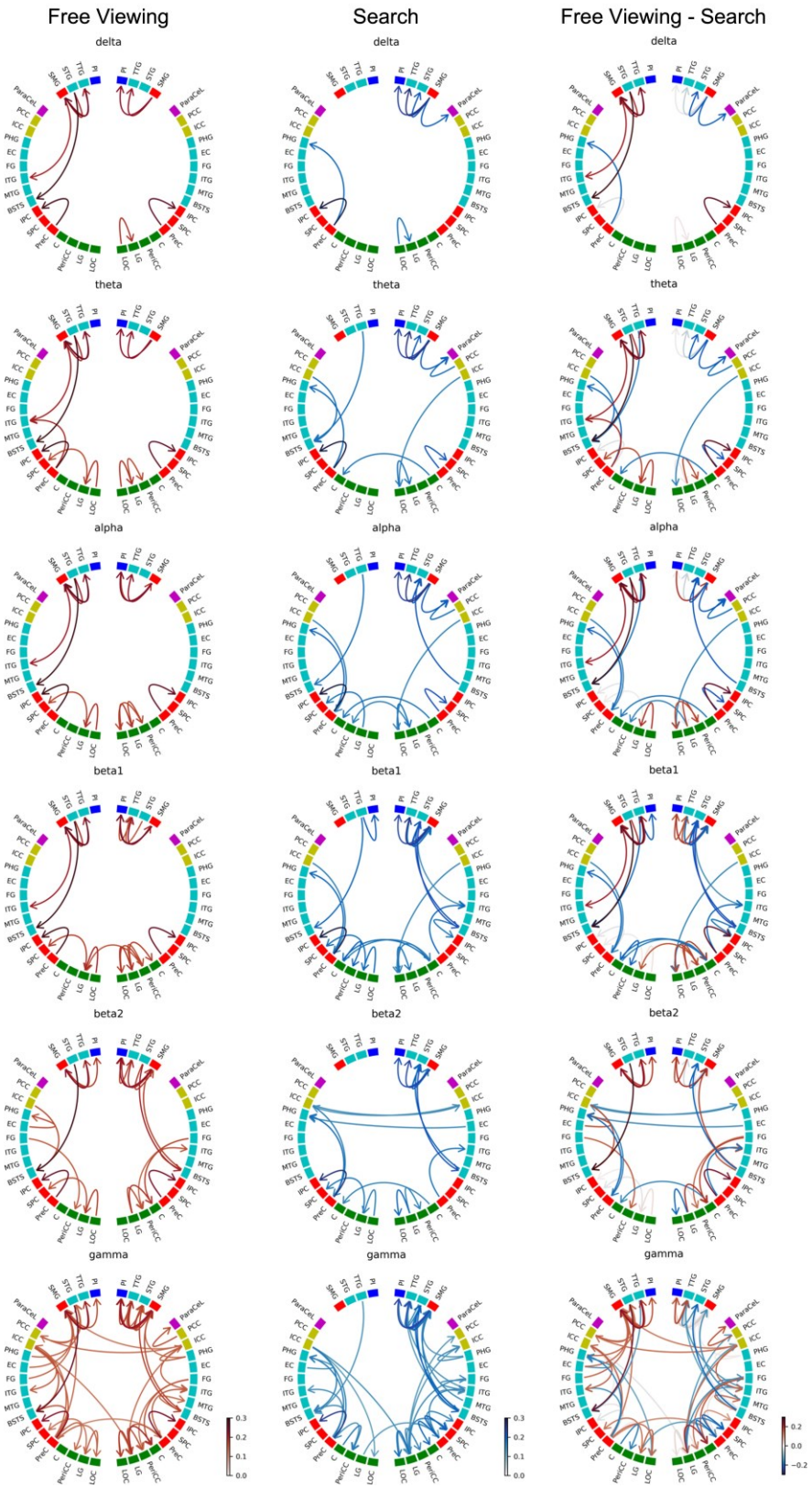

Figure 45: GPDC group-level results for fixation onset during FV, VS, and FV minus VS. Stronger connections during FV are indicated by red arrows and stronger connections during VS are indicated by blue arrows. If the connections were of similar strength during FV and VS, the arrows are grey. The ROIs are grouped by clusters and colored according to the anatomical higher-level regions (frontal lobe: magenta, insula: blue, cingulate cortex: yellow, temporal lobe: turquoise, parietal lobe: red, occipital lobe: green). Figure reprinted from (Kiefer et al. 2022). Copyright 2022 by Kiefer et al.

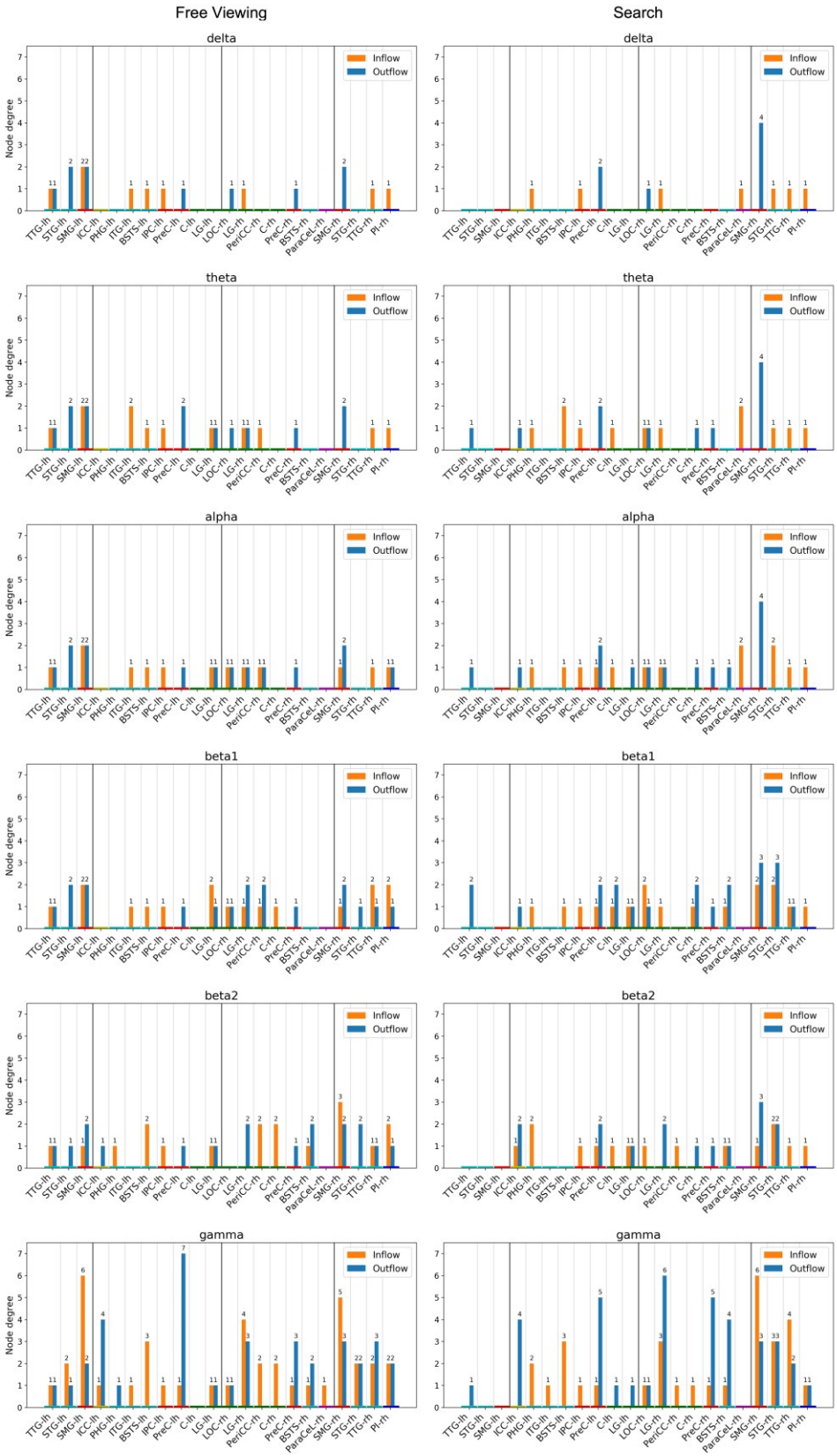

Figure 46: Node degree (the number of in- and outflowing connections) for each ROI. ROIs were only included if the node degree was equal to or above the 95th percentile according to the random permutation analysis in at least one frequency band. The ROIs are grouped by clusters and colored according to the anatomical higher-level regions (frontal lobe: magenta, insula: blue, cingulate cortex: yellow, temporal lobe: turquoise, parietal lobe: red, occipital lobe: green. Figure reprinted from (Kiefer et al. 2022). Copyright 2022 by Kiefer et al.

REFERENCES

4-D Neuroimaging. 2003. “Magnes 3600 WH Product Description,” 1–22.

———. 2006. “Magnes 2500 WH-X/3600 WH Hardware Reference Manual.” San Diego, CA.

Abiri, Reza, Soheil Borhani, Eric W. Sellers, Yang Jiang, and Xiaopeng Zhao. 2019. “A Comprehensive Review of EEG-Based Brain-Computer Interface Paradigms.” *Journal of Neural Engineering* 16 (1): aaf12e. https://doi.org/10.1088/1741-2552/aaf12e.

Agtzidis, Ioannis, Inga Meyhöfer, Michael Dorr, and Rebekka Lencer. 2020. “Following Forrest Gump: Smooth Pursuit Related Brain Activation during Free Movie Viewing.” *NeuroImage* 216 (December 2019): 116491. https://doi.org/10.1016/j.neuroimage.2019.116491.

Akaike, Hirotugu. 1974. “A New Look at the Statistical Model Identification.” *IEEE Transactions on Automatic Control* 19 (6): 716–23. https://doi.org/10.1109/TAC.1974.1100705.

Amico, Enrico, and Joaquín Goñi. 2018. “The Quest for Identifiability in Human Functional Connectomes.” *Scientific Reports* 8 (1): 1–14. https://doi.org/10.1038/s41598-018-25089-1.

Andrews, Donald W. K., and Werner Ploberger. 1994. “Optimal Tests When a Nuisance Parameter Is Present Only Under the Alternative.” *Econometrica* 62 (6): 1383. https://doi.org/10.2307/2951753.

Ángeles Fernández-Gil, M., R. Palacios-Bote, M. Leo-Barahona, and J. P. Mora-Encinas. 2010. “Anatomy of the Brainstem: A Gaze into the Stem of Life.” *Seminars in Ultrasound, CT and MRI* 31 (3): 196–219. https://doi.org/10.1053/j.sult.2010.03.006.

Baccalá, Luiz A., and Koichi Sameshima. 2001. “Partial Directed Coherence: A New Concept in Neural Structure Determination.” *Proceedings of the National Academy of Sciences of the United States of America* 84 (6): 463–74. https://doi.org/10.1007/PL00007990.

Baccalá, Luiz A., Koichi Sameshima, and D.Y. Takahashi. 2007. “Generalized Partial Directed Coherence.” In *2007 15th International Conference on Digital Signal Processing*, 163–66. Cardiff, UK: IEEE. https://doi.org/10.1109/ICDSP.2007.4288544.

Bagnall, Anthony, Michael Flynn, James Large, Jason Lines, and Matthew Middlehurst. 2020. “On the Usage and Performance of the Hierarchical Vote Collective of Transformation-Based Ensembles Version 1.0 (HIVE-COTE v1.0).” *Lecture Notes in Computer Science (Including Subseries Lecture Notes in Artificial Intelligence and Lecture Notes in Bioinformatics)* 12588 LNAI: 3–18. https://doi.org/10.1007/978-3-030-65742-0_1.

Bagnall, Anthony, Jason Lines, Aaron Bostrom, James Large, and Eamonn Keogh. 2017. “The Great Time Series Classification Bake off: A Review and Experimental Evaluation of Recent Algorithmic Advances.” *Data Mining and Knowledge Discovery* 31 (3): 606–60. https://doi.org/10.1007/s10618-016-0483-9.

Baillet, Sylvain. 2017. “Magnetoencephalography for Brain Electrophysiology and Imaging.” *Nature Neuroscience* 20 (3): 327–39. https://doi.org/10.1038/nn.4504.

Baltaretu, Bianca R., Simona Monaco, Jena Velji-Ibrahim, Gaelle N. Luabeya, and J. Douglas Crawford. 2020. "Parietal Cortex Integrates Saccade and Object Orientation Signals to Update Grasp Plans." *Journal of Neuroscience* 40 (23): 4525–35. https://doi.org/10.1523/JNEUROSCI.0300-20.2020.

Bari, Sumra, Enrico Amico, Nicole Vike, Thomas M. Talavage, and Joaquín Goñi. 2019. "Uncovering Multi-Site Identifiability Based on Resting-State Functional Connectomes." *NeuroImage* 202 (November): 115967. https://doi.org/10.1016/j.neuroimage.2019.06.045.

Barnett, Lionel, and Anil K. Seth. 2011. "Behaviour of Granger Causality under Filtering: Theoretical Invariance and Practical Application." *Journal of Neuroscience Methods* 201 (2): 404–19. https://doi.org/10.1016/j.jneumeth.2011.08.010.

Başar, Erol. 1990. *Chaos in Brain Function*. Edited by Erol Başar. Berlin, Heidelberg: Springer Berlin Heidelberg. https://doi.org/10.1007/978-3-642-75545-3.

Beck, Aaron T, Robert A Steer, and Gregory Brown. 1996. "Beck Depression Inventory-II." *Psychological Assessment*.

Benjamini, Yoav, and Yosef Hochberg. 1995. "Controlling the False Discovery Rate: A Practical and Powerful Approach to Multiple Testing." *Journal of the Royal Statistical Society: Series B (Methodological)* 57 (1): 289–300. https://doi.org/10.1111/j.2517-6161.1995.tb02031.x.

Berger, Denise, Antonio Pazienti, Francisco J. Flores, Martin P. Nawrot, Pedro E. Maldonado, and Sonja Grün. 2012. "Viewing Strategy of Cebus Monkeys during Free Exploration of Natural Images." *Brain Research* 1434: 34–46. https://doi.org/10.1016/j.brainres.2011.10.013.

Billinger, Martin, Clemens Brunner, and Gernot R. Müller-Putz. 2014. "SCoT: A Python Toolbox for EEG Source Connectivity." *Frontiers in Neuroinformatics* 8 (MAR): 22. https://doi.org/10.3389/fninf.2014.00022.

Bommel, Franz R., Rudolf Rockelein, and Laxmikant Urankar. 1993. "Boundary Element Solution of Biomagnetic Problems." *IEEE Transactions on Magnetics* 29 (2): 1395–98. https://doi.org/10.1109/20.250663.

Bonferroni, Carlo Emilio. 1936. "Teoria Statistica Delle Classi e Calcolo Delle Probabilità." *Pubblicazioni Del R. Istituto Superiore Di Scienze Economiche e Commerciali Di Firenze* 8: 3–62.

Bressler, Steven L., and Anil K. Seth. 2011. "Wiener-Granger Causality: A Well Established Methodology." *NeuroImage* 58 (2): 323–29. https://doi.org/10.1016/j.neuroimage.2010.02.059.

Breuer, Lukas. 2016. "Identification of Neuromagnetic Responses for Real-Time Analysis in Magnetoencephalography." RWTH Aachen University, Aachen, Germany. https://publications.rwth-aachen.de/record/569556/files/569556.pdf.

Brookes, Matthew J., George C. O'Neill, Emma L. Hall, Mark W. Woolrich, Adam Baker, Sofia Palazzo Corner, Siân E. Robson, Peter G. Morris, and Gareth R. Barnes. 2014. "Measuring Temporal, Spectral and Spatial Changes in Electrophysiological Brain Network Connectivity." *NeuroImage* 91: 282–99. https://doi.org/10.1016/j.neuroimage.2013.12.066.

Brouwer, Anne Marie, Boris Reuderink, Joris Vincent, Marcel A.J. van Gerven, and Jan B.F. van Erp. 2013. "Distinguishing between Target and Nontarget Fixations in a Visual Search Task Using Fixation-Related Potentials." *Journal of Vision* 13 (3): 17. https://doi.org/10.1167/13.3.17.

Campain, Robert, and Jeff Minckler. 1976. “A Note on the Gross Configurations of the Human Auditory Cortex.” *Brain and Language* 3 (2): 318–23. https://doi.org/10.1016/0093-934X(76)90026-2.

Cave, K. R, and J. M Wolfe. 1999. “The Psychophysical Evidence for a Binding Problem in Human Vision.” *Neuron* 24 (1): 11–17, 111–25. https://doi.org/https://doi.org/10.1016/S0896-6273(00)80818-1.

Chen, Xin, and Gregory J. Zelinsky. 2006. “Real-World Visual Search Is Dominated by Top-down Guidance.” *Vision Research* 46 (24): 4118–33. https://doi.org/10.1016/j.visres.2006.08.008.

Chow, Gregory C. 1960. “Tests of Equality Between Sets of Coefficients in Two Linear Regressions.” *Econometrica* 28 (3): 591. https://doi.org/10.2307/1910133.

Clerc, M, A Dervieux, and O Faugeras. 2002. “Comparison of BEM and FEM Methods for the E/MEG Problem.” In *Proceedings of BIOMAG 2002*. http://citeseerx.ist.psu.edu/viewdoc/download?doi=10.1.1.118.1130&rep=rep1&type=pdf.

Cloutman, Lauren L., Richard J. Binney, Mark Drakesmith, Geoffrey J.M. Parker, and Matthew A. Lambon Ralph. 2012. “The Variation of Function across the Human Insula Mirrors Its Patterns of Structural Connectivity: Evidence from in Vivo Probabilistic Tractography.” *NeuroImage* 59 (4): 3514–21. https://doi.org/10.1016/j.neuroimage.2011.11.016.

Cohen, David. 1968. “Magnetoencephalography: Evidence of Magnetic Fields Produced by Alpha-Rhythm Currents.” *Science* 161 (3843): 784–86. https://doi.org/10.1126/science.161.3843.784.

Corbetta, Maurizio, Gaurav Patel, and Gordon L. Shulman. 2008. “The Reorienting System of the Human Brain: From Environment to Theory of Mind.” *Neuron* 58 (3): 306–24. https://doi.org/10.1016/j.neuron.2008.04.017.

Corbetta, Maurizio, and Gordon L. Shulman. 2002. “Control of Goal-Directed and Stimulus-Driven Attention in the Brain.” *Nature Reviews Neuroscience* 3 (3): 201–15. https://doi.org/10.1038/nrn755.

Costa, Sandra da, Wietske van der Zwaag, Jose P. Marques, Richard S.J. Frackowiak, Stephanie Clarke, and Melissa Saenz. 2011. “Human Primary Auditory Cortex Follows the Shape of Heschl’s Gyrus.” *Journal of Neuroscience* 31 (40): 14067–75. https://doi.org/10.1523/JNEUROSCI.2000-11.2011.

Cuffin, B. Neil. 1990. “Effects of Head Shape on EEG’s and MEG’s.” *IEEE Transactions on Biomedical Engineering* 37 (1): 44–52. https://doi.org/10.1109/10.43614.

———. 1995. “A Method for Localizing EEG Sources in Realistic Head Models.” *IEEE Transactions on Biomedical Engineering* 42 (1): 68–71. https://doi.org/10.1109/10.362917.

Cuffin, B. Neil, and David Cohen. 1977. “Magnetic Fields of a Dipole in Special Volume Conductor Shapes.” *IEEE Transactions on Biomedical Engineering* BME-24 (4): 372–81. https://doi.org/10.1109/TBME.1977.326145.

Dale, Anders M., Bruce Fischl, and Martin I. Sereno. 1999. “Cortical Surface-Based Analysis: I. Segmentation and Surface Reconstruction.” *NeuroImage* 9 (2): 179–94. https://doi.org/10.1006/nimg.1998.0395.

Dale, Anders M., Arthur K. Liu, Bruce R. Fischl, Randy L. Buckner, John W. Belliveau, Jeffrey D. Lewine, and Eric Halgren. 2000. “Dynamic Statistical Parametric Mapping: Combining FMRI and MEG for High-Resolution Imaging of Cortical Activity.” *Neuron* 26 (1): 55–67. https://doi.org/10.1016/S0896-6273(00)81138-1.

Dale, Anders M, and Martin I. Sereno. 1993. “Improved Localization of Cortical Activity by Combining EEG and MEG with MRI Cortical Surface Reconstruction: A Linear Approach.” *Journal of Cognitive Neuroscience* 5 (2): 162–76. https://doi.org/10.1162/jocn.1993.5.2.162.

Dammers, Jürgen, Michael Schiek, Frank Boers, Carmen Silex, Mikhail Zvyagintsev, Uwe Pietrzyk, and Klaus Mathiak. 2008. “Integration of Amplitude and Phase Statistics for Complete Artifact Removal in Independent Components of Neuromagnetic Recordings.” *IEEE Transactions on Biomedical Engineering* 55 (10): 2353–62. https://doi.org/10.1109/TBME.2008.926677.

Dandekar, Sangita, Jian Ding, Claudio Privitera, Thom Carney, and Stanley A. Klein. 2012. “The Fixation and Saccade P3.” *PLoS ONE* 7 (11): 1–14. https://doi.org/10.1371/journal.pone.0048761.

Dau, Hoang Anh, Anthony Bagnall, Kaveh Kamgar, Chin Chia Michael Yeh, Yan Zhu, Shaghayegh Gharghabi, Chotirat Annh Ratanamahatana, and Eamonn Keogh. 2019. “The UCR Time Series Archive.” *IEEE/CAA Journal of Automatica Sinica* 6 (6): 1293–1305. https://doi.org/10.1109/JAS.2019.1911747.

Deaver, Bascom S., and William M. Fairbank. 1961. “Experimental Evidence for Quantized Flux in Superconducting Cyclinders.” *Physical Review Letters* 7 (2): 43–46. https://doi.org/10.1103/PhysRevLett.7.43.

Delorme, Arnaud, Guillaume A. Rousselet, Marc J.M. Macé, and Michèle Fabre-Thorpe. 2004. “Interaction of Top-down and Bottom-up Processing in the Fast Visual Analysis of Natural Scenes.” *Cognitive Brain Research* 19 (2): 103–13. https://doi.org/10.1016/j.cogbrainres.2003.11.010.

Dempster, Angus, François Petitjean, and Geoffrey I. Webb. 2020. “ROCKET: Exceptionally Fast and Accurate Time Series Classification Using Random Convolutional Kernels.” *Data Mining and Knowledge Discovery* 34 (5): 1454–95. https://doi.org/10.1007/s10618-020-00701-z.

Demuru, M., A. A. Gouw, A. Hillebrand, C. J. Stam, B. W. Van Dijk, P. Scheltens, B. M. Tijms, et al. 2017. “Functional and Effective Whole Brain Connectivity Using Magnetoencephalography to Identify Monozygotic Twin Pairs.” *Scientific Reports* 7 (1): 1–11. https://doi.org/10.1038/s41598-017-10235-y.

Desikan, Rahul S., Florent Ségonne, Bruce Fischl, Brian T. Quinn, Bradford C. Dickerson, Deborah Blacker, Randy L. Buckner, et al. 2006. “An Automated Labeling System for Subdividing the Human Cerebral Cortex on MRI Scans into Gyral Based Regions of Interest.” *NeuroImage* 31 (3): 968–80. https://doi.org/10.1016/j.neuroimage.2006.01.021.

Dimigen, Olaf, Werner Sommer, Annette Hohlfeld, Arthur M. Jacobs, and Reinhold Kliegl. 2011. “Coregistration of Eye Movements and EEG in Natural Reading: Analyses and Review.” *Journal of Experimental Psychology: General* 140 (4): 552–72. https://doi.org/10.1037/a0023885.

Ding, Mingzhou, Steven L Bressler, Weiming Yang, and Hualou Liang. 2000. “Short-Window Spectral Analysis of Cortical Event-Related Potentials by Adaptive Multivariate Autoregressive Modeling: Data Preprocessing, Model Validation, and Variability Assessment.” *Biological Cybernetics* 83 (1): 35–45. https://doi.org/https://doi.org/10.1007/s004229900137.

Ding, Mingzhou, Yonghong Chen, and Steven L. Bressler. 2006. “Granger Causality: Basic Theory and Application to Neuroscience.” In *Handbook of Time Series Analysis*, edited by Björn Schelter, Matthias Winterhalder, and Jens Timmer, 437–60. Weinheim, Germany: Wiley-VCH Verlag GmbH & Co. KGaA.

https://doi.org/10.1002/9783527609970.ch17.
Doll, R., and M. Näbauer. 1961. “Experimental Proof of Magnetic Flux Quantization in a Superconducting Ring.” *Physical Review Letters* 7 (2): 51–52. https://doi.org/10.1103/PhysRevLett.7.51.
Dragone, Alessio, Stefano Lasaponara, Massimo Silvetti, Emiliano Macaluso, and Fabrizio Doricchi. 2015. “Selective Reorienting Response of the Left Hemisphere to Invalid Visual Targets in the Right Side of Space: Relevance for the Spatial Neglect Syndrome.” *Cortex* 65: 31–35. https://doi.org/10.1016/j.cortex.2014.12.009.
Dunkley, Benjamin T., Bianca Baltaretu, and J. Douglas Crawford. 2016. “Trans-Saccadic Interactions in Human Parietal and Occipital Cortex during the Retention and Comparison of Object Orientation.” *Cortex* 82: 263–76. https://doi.org/10.1016/j.cortex.2016.06.012.
Duret, D., and P. Karp. 1983. “Instrumentation for Biomagnetism.” *Il Nuovo Cimento D* 2 (2): 123–41. https://doi.org/10.1007/BF02455917.
Ellison, Amanda, Igor Schindler, Lara L. Pattison, and A. David Milner. 2004. “An Exploration of the Role of the Superior Temporal Gyrus in Visual Search and Spatial Perception Using TMS.” *Brain* 127 (10): 2307–15. https://doi.org/10.1093/brain/awh244.
Engle, Robert F., and C. W. J. Granger. 1987. “Co-Integration and Error Correction: Representation, Estimation, and Testing.” *Econometrica* 55 (2): 251. https://doi.org/10.2307/1913236.
Ester, Martin, Hans-Peter Kriegel, Jörg Sander, and Xiaowei Xu. 1996. “A Density-Based Algorithm for Discovering Clusters in Large Spatial Databases with Noise.” *Kdd* 96 (34): 226–31.
Fagaly, R. L. 2006. “Superconducting Quantum Interference Device Instruments and Applications.” *Review of Scientific Instruments* 77 (10): 1–45. https://doi.org/10.1063/1.2354545.
Fasoula, Angie, Yohan Attal, and Denis Schwartz. 2013. “Comparative Performance Evaluation of Data-Driven Causality Measures Applied to Brain Networks.” *Journal of Neuroscience Methods* 215 (2): 170–89. https://doi.org/10.1016/j.jneumeth.2013.02.021.
Findlay, John M., and Iain D. Gilchrist. 2008. *Active Vision: The Psychology of Looking and Seeing*. *Active Vision: The Psychology of Looking and Seeing*. https://doi.org/10.1093/acprof:oso/9780198524793.001.0001.
Finke, Andrea, Kai Essig, Giuseppe Marchioro, and Helge Ritter. 2016. “Toward FRP-Based Brain-Machine Interfaces-Single-Trial Classification of Fixation-Related Potentials.” *PLoS ONE* 11 (1): 1–19. https://doi.org/10.1371/journal.pone.0146848.
Finn, Emily S., Xilin Shen, Dustin Scheinost, Monica D. Rosenberg, Jessica Huang, Marvin M. Chun, Xenophon Papademetris, and R. Todd Constable. 2015. “Functional Connectome Fingerprinting: Identifying Individuals Using Patterns of Brain Connectivity.” *Nature Neuroscience* 18 (11): 1664–71. https://doi.org/10.1038/nn.4135.
Fischl, Bruce, Martin I. Sereno, Roger B.H. Tootell, and Anders M. Dale. 1999. “High-Resolution Intersubject Averaging and a Coordinate System for the Cortical Surface.” *Human Brain Mapping* 8 (4): 272–84. https://doi.org/10.1002/(SICI)1097-0193(1999)8:4<272::AID-HBM10>3.0.CO;2-4.

Florin, Esther. 2010. *Causality Measures between Neural Signals from Invasively and Non-Invasively Obtained Local Field Potentials in Humans*. Jülich: Forschungszentrum Jülich GmbH Zentralbibliothek, Verlag. http://hdl.handle.net/2128/3776.

Florin, Esther, Joachim Gross, Johannes Pfeifer, Gereon R. Fink, and Lars Timmermann. 2010. "The Effect of Filtering on Granger Causality Based Multivariate Causality Measures." *NeuroImage* 50 (2): 577–88. https://doi.org/10.1016/j.neuroimage.2009.12.050.

Fraschini, Matteo, Arjan Hillebrand, Matteo Demuru, Luca Didaci, and Gian Luca Marcialis. 2015. "An EEG-Based Biometric System Using Eigenvector Centrality in Resting State Brain Networks." *IEEE Signal Processing Letters* 22 (6): 666–70. https://doi.org/10.1109/LSP.2014.2367091.

Friston, Karl J. 2011. "Functional and Effective Connectivity: A Review." *Brain Connectivity* 1 (1): 13–36. https://doi.org/10.1089/brain.2011.0008.

Friston, Karl J., L. Harrison, and W. Penny. 2003. "Dynamic Causal Modelling." *NeuroImage* 19 (4): 1273–1302. https://doi.org/doi.org/10.1016/S1053-8119(03)00202-7.

Geweke, John F. 1982. "Measurement of Linear Dependence and Feedback Between Multiple Time Series: Comment." *Journal of the American Statistical Association* 77 (378): 304–13. https://doi.org/10.2307/2287238.

———. 1984. "Measures of Conditional Linear Dependence and Feedback between Time Series." *Journal of the American Statistical Association* 79 (388): 907–15. https://doi.org/10.1080/01621459.1984.10477110.

Gharabaghi, Alireza, Monika Fruhmann Berger, Marcos Tatagiba, and Hans-Otto Karnath. 2006. "The Role of the Right Superior Temporal Gyrus in Visual Search-Insights from Intraoperative Electrical Stimulation." *Neuropsychologia* 44 (12): 2578–81. https://doi.org/10.1016/j.neuropsychologia.2006.04.006.

Ghaziri, Jimmy, Alan Tucholka, Gabriel Girard, Jean Christophe Houde, Olivier Boucher, Guillaume Gilbert, Maxime Descoteaux, Sarah Lippé, Pierre Rainville, and Dang Khoa Nguyen. 2017. "The Corticocortical Structural Connectivity of the Human Insula." *Cerebral Cortex (New York, N.Y. : 1991)* 27 (2): 1216–28. https://doi.org/10.1093/cercor/bhv308.

Golay, Laetitia, Armin Schnider, and Radek Ptak. 2008. "Cortical and Subcortical Anatomy of Chronic Spatial Neglect Following Vascular Damage." *Behavioral and Brain Functions* 4: 1–10. https://doi.org/10.1186/1744-9081-4-43.

Goodale, Melvyn A., and A. David Milner. 1992. "Separate Visual Pathways for Perception and Action." *Trends in Neurosciences* 15 (1): 20–25. https://doi.org/10.1016/0166-2236(92)90344-8.

Gramfort, Alexandre, Martin Luessi, Eric Larson, Denis A. Engemann, Daniel Strohmeier, Christian Brodbeck, Lauri Parkkonen, and Matti S. Hämäläinen. 2014. "MNE Software for Processing MEG and EEG Data." *NeuroImage* 86: 446–60. https://doi.org/10.1016/j.neuroimage.2013.10.027.

Gramfort, Alexandre, Martin Luessi, Eric Larson, Denis A Engemann, Daniel Strohmeier, Christian Brodbeck, Roman Goj, et al. 2013. "MEG and EEG Data Analysis with MNE-Python." *Frontiers in Neuroscience* 7 (7 DEC): 267. https://doi.org/10.3389/fnins.2013.00267.

Granger, C. W. J. 1969. "Investigating Causal Relations by Econometric Models and Cross-Spectral Methods." *Econometrica* 37 (3): 424–38. https://doi.org/10.2307/1912791.

———. 1980. “Testing for Causality. A Personal Viewpoint.” *Journal of Economic Dynamics and Control* 2 (C): 329–52. https://doi.org/10.1016/0165-1889(80)90069-X.

Greene, Abigail S., Siyuan Gao, Dustin Scheinost, and R. Todd Constable. 2018. “Task-Induced Brain State Manipulation Improves Prediction of Individual Traits.” *Nature Communications* 9 (1). https://doi.org/10.1038/s41467-018-04920-3.

Greene, William H. 2003. *Econometric Analysis*. 5th ed. Upper Saddle River, NJ: Prentice Hall International.

Grosbras, M. H., E. Lobel, P. F. Van de Moortele, D. LeBihan, and Alain Berthoz. 1999. “An Anatomical Landmark for the Supplementary Eye Fields in Human Revealed with Functional Magnetic Resonance Imaging.” *Cerebral Cortex* 9 (7): 705–11. https://doi.org/10.1093/cercor/9.7.705.

Gross, Joachim, Jan Kujala, Matti S. Hämäläinen, Lars Timmermann, Alfons Schnitzler, and Riitta Salmelin. 2001. “Dynamic Imaging of Coherent Sources: Studying Neural Interactions in the Human Brain.” *Proceedings of the National Academy of Sciences of the United States of America* 98 (2): 694–99. https://doi.org/10.1073/pnas.98.2.694.

Hämäläinen, Matti S., and Riitta Hari. 2002. “Magnetoencephalographic Characterization of Dynamic Brain Activation: Basic Principles and Methods of Data Collection and Source Analysis.” *Brain Mapping: The Methods*, 227–53. https://doi.org/10.1016/b978-012693019-1/50012-5.

Hämäläinen, Matti S., Riitta Hari, Risto J. Ilmoniemi, Jukka Knuutila, and Olli V. Lounasmaa. 1993. “Magnetoencephalography - Theory, Instrumentation, and Applications to Noninvasive Studies of the Working Human Brain.” *Reviews of Modern Physics* 65 (2): 413–97. https://doi.org/10.1103/RevModPhys.65.413.

Hämäläinen, Matti S., and Risto J. Ilmoniemi. 1984. “Interpreting Measured Magnetic Fields of the Brain: Estimates of Current Distributions.” *Univ. Helsinki, Finland Tech. Rep. TKK-F-A559*, 1–35.

———. 1994. “Interpreting Magnetic Fields of the Brain: Minimum Norm Estimates.” *Medical & Biological Engineering & Computing* 32 (1): 35–42. https://doi.org/10.1007/BF02512476.

Hämäläinen, Matti S., and Jukka Sarvas. 1989. “Realistic Conductivity Geometry Model of the Human Head for Interpretation of Neuromagnetic Data.” *IEEE Transactions on Biomedical Engineering* 36 (2): 165–71. https://doi.org/10.1109/10.16463.

Hannan, E. J., and B. G. Quinn. 1979. “The Determination of the Order of an Autoregression.” *Journal of the Royal Statistical Society: Series B (Methodological)* 41 (2): 190–95. https://doi.org/10.1111/j.2517-6161.1979.tb01072.x.

Hansen, Bruce E. 2000. “Testing for Structural Change in Conditional Models.” *Journal of Econometrics* 97 (1): 93–115. https://doi.org/10.1016/S0304-4076(99)00068-8.

Hauk, Olaf. 2004. “Keep It Simple: A Case for Using Classical Minimum Norm Estimation in the Analysis of EEG and MEG Data.” *NeuroImage* 21 (4): 1612–21. https://doi.org/10.1016/j.neuroimage.2003.12.018.

Heaviside, Oliver. 1892. “On the Forces, Stresses, and Fiuxes of Energy in the Electromagnetic Field.” *Philosophical Transactions of the Royal Society A: Mathematical, Physical and Engineering Sciences* 183 (0): 423–80. https://doi.org/10.1098/rsta.1892.0011.

Helmholtz, H. 1853. "Ueber Einige Gesetze Der Vertheilung Elektrischer Ströme in Körperlichen Leitern Mit Anwendung Auf Die Thierisch - elektrischen Versuche." *Annalen Der Physik* 165 (6): 211–33. https://doi.org/10.1002/andp.18531650603.

Horn, John Darrell van, Scott T. Grafton, and Michael B. Miller. 2008. "Individual Variability in Brain Activity: A Nuisance or an Opportunity?" *Brain Imaging and Behavior* 2 (4): 327–34. https://doi.org/10.1007/s11682-008-9049-9.

Hyvärinen, Aapo, and Erkki Oja. 2000. "Independent Component Analysis: Algorithms and Applications." *Neural Networks* 13 (4–5): 411–30. https://doi.org/10.1016/S0893-6080(00)00026-5.

Ilmoniemi, Risto J., Matti S. Hämäläinen, and J Knuutila. 1985. "The Forward and Inverse Problems." *Biomagnetism: Applications and Theory*, no. January 1985: 278–82.

Ismail Fawaz, Hassan, Germain Forestier, Jonathan Weber, Lhassane Idoumghar, and Pierre-Alain Muller. 2019. "Deep Learning for Time Series Classification: A Review." *Data Mining and Knowledge Discovery* 33 (4): 917–63. https://doi.org/10.1007/s10618-019-00619-1.

Ismail Fawaz, Hassan, Benjamin Lucas, Germain Forestier, Charlotte Pelletier, Daniel F. Schmidt, Jonathan Weber, Geoffrey I. Webb, Lhassane Idoumghar, Pierre Alain Muller, and François Petitjean. 2020. "InceptionTime: Finding AlexNet for Time Series Classification." *Data Mining and Knowledge Discovery* 34 (6): 1936–62. https://doi.org/10.1007/s10618-020-00710-y.

Ito, Junji, Yukako Yamane, Mika Suzuki, Pedro Maldonado, Ichiro Fujita, Hiroshi Tamura, and Sonja Grn. 2017. "Switch from Ambient to Focal Processing Mode Explains the Dynamics of Free Viewing Eye Movements." *Scientific Reports* 7 (1): 1–14. https://doi.org/10.1038/s41598-017-01076-w.

Jaklevic, R. C., John Lambe, A. H. Silver, and J. E. Mercereau. 1964. "Quantum Interference Effects in Josephson Tunneling." *Physical Review Letters* 12 (7): 159–60. https://doi.org/10.1103/PhysRevLett.12.159.

Jensen, Ole, and Christian Hesse. 2010. "Estimating Distributed Representations of Evoked Responses and Oscillatory Brain Activity." In *MEG: An Introduction to Methods*, edited by Peter Hansen, Morten Kringelbach, and Riitta Salmelin, 156–85. New York, NY: Oxford Scholarship Online. https://doi.org/10.1093/acprof:oso/9780195307238.003.0007.

Jimenez, Abelino, and Bhiksha Raj. 2019. "Time Signal Classification Using Random Convolutional Features." In *ICASSP 2019 - 2019 IEEE International Conference on Acoustics, Speech and Signal Processing (ICASSP)*, 3592–96. IEEE. https://doi.org/10.1109/ICASSP.2019.8682489.

Jo, Han-Gue, Junji Ito, Barbara Schulte Holthausen, Conrad Baumann, Sonja Grün, Ute Habel, and Thilo Kellermann. 2019. "Task-Dependent Functional Organizations of the Visual Ventral Stream." *Scientific Reports* 9 (1): 1–10. https://doi.org/10.1038/s41598-019-45707-w.

Jo, Han-Gue, Thilo Kellermann, Conrad Baumann, Junji Ito, Barbara Schulte Holthausen, Frank Schneider, Sonja Grün, and Ute Habel. 2019. "Distinct Modes of Top-down Cognitive Processing in the Ventral Visual Cortex." *NeuroImage* 193 (August 2018): 201–13. https://doi.org/10.1016/j.neuroimage.2019.02.068.

Josephson, B. D. 1962. "Possible New Effects in Superconductive Tunnelling." *Physics Letters* 1 (7): 251–53. https://doi.org/10.1016/0031-9163(62)91369-

0.
Kamienkowski, Juan E., Matias J. Ison, Rodrigo Quian Quiroga, and Mariano Sigman. 2012. “Fixation-Related Potentials in Visual Search: A Combined EEG and Eye Tracking Study.” *Journal of Vision* 12 (7): 1–20. https://doi.org/10.1167/12.7.4.
Kaminski, M. J., and K. J. Blinowska. 1991. “A New Method of the Description of the Information Flow in the Brain Structures.” *Biological Cybernetics* 65 (3): 203–10. https://doi.org/10.1007/BF00198091.
Karnath, Hans-Otto, Susanne Ferber, and Marc Himmelbach. 2001. “Spatial Awareness Is a Function of the Temporal Not the Posterior Parietal Lobe.” *Nature* 411 (6840): 950–53. https://doi.org/10.1038/35082075.
Karnath, Hans-Otto, Monika Fruhmann Berger, Wilhelm Küker, and Chris Rorden. 2004. “The Anatomy of Spatial Neglect Based on Voxelwise Statistical Analysis: A Study of 140 Patients.” *Cerebral Cortex* 14 (10): 1164–72. https://doi.org/10.1093/cercor/bhh076.
Kaufmann, Tobias, Dag Alnæs, Nhat Trung Doan, Christine Lycke Brandt, Ole A. Andreassen, and Lars T. Westlye. 2017. “Delayed Stabilization and Individualization in Connectome Development Are Related to Psychiatric Disorders.” *Nature Neuroscience* 20 (4): 513–15. https://doi.org/10.1038/nn.4511.
Kaunitz, Lisandro N., Juan E. Kamienkowski, Alexander Varatharajah, Mariano Sigman, Rodrigo Quian Quiroga, and Matias J. Ison. 2014. “Looking for a Face in the Crowd: Fixation-Related Potentials in an Eye-Movement Visual Search Task.” *NeuroImage* 89: 297–305. https://doi.org/10.1016/j.neuroimage.2013.12.006.
Kazai, Koji, and Akihiro Yagi. 1999. “Integrated Effect of Stimulation at Fixation Points on EFRP (Eye-Fixation Related Brain Potentials).” *International Journal of Psychophysiology* 32 (3): 193–203. https://doi.org/10.1016/S0167-8760(99)00010-0.
Keogh, Eamonn, and Shruti Kasetty. 2003. “On the Need for Time Series Data Mining Benchmarks: A Survey and Empirical Demonstration.” *Data Mining and Knowledge Discovery* 7 (4): 349–71. https://doi.org/10.1023/A:1024988512476.
Keysers, C., D. K. Xiao, P. Földiák, and D. I. Perrett. 2001. “The Speed of Sight.” *Journal of Cognitive Neuroscience* 13 (1): 90–101. https://doi.org/10.1162/089892901564199.
Kiefer, Christian M., Junji Ito, Ralph Weidner, Frank Boers, N. Jon Shah, Sonja Grün, and Jürgen Dammers. 2022. “Revealing Whole-Brain Causality Networks During Guided Visual Searching.” *Frontiers in Neuroscience* 16 (February). https://doi.org/10.3389/fnins.2022.826083.
Kleinfeld, David, Ehud Ahissar, and Mathew E. Diamond. 2006. “Active Sensation: Insights from the Rodent Vibrissa Sensorimotor System.” *Current Opinion in Neurobiology* 16 (4): 435–44. https://doi.org/10.1016/j.conb.2006.06.009.
Koenigs, Michael, Aron K. Barbey, Bradley R. Postle, and Jordan Grafman. 2009. “Superior Parietal Cortex Is Critical for the Manipulation of Information in Working Memory.” *Journal of Neuroscience* 29 (47): 14980–86. https://doi.org/10.1523/JNEUROSCI.3706-09.2009.
Kong, Wanzeng, Luyun Wang, Sijia Xu, Fabio Babiloni, and Hang Chen. 2019. “EEG Fingerprints: Phase Synchronization of EEG Signals as Biomarker for Subject

Identification." *IEEE Access* 7: 121165–73. https://doi.org/10.1109/ACCESS.2019.2931624.
Krizhevsky, Alex, Ilya Sutskever, and Geoffrey E. Hinton. 2012. "ImageNet Classification with Deep Convolutional Neural Networks." *Advances in Neural Information Processing Systems* 2: 1097–1105.
Kurth, Florian, Karl Zilles, Peter T. Fox, Angela R. Laird, and Simon B. Eickhoff. 2010. "A Link between the Systems: Functional Differentiation and Integration within the Human Insula Revealed by Meta-Analysis." *Brain Structure & Function* 214 (5–6): 519–34. https://doi.org/10.1007/s00429-010-0255-z.
Kwiatkowski, Denis, Peter C.B. Phillips, Peter Schmidt, and Yongcheol Shin. 1992. "Testing the Null Hypothesis of Stationarity against the Alternative of a Unit Root. How Sure Are We That Economic Time Series Have a Unit Root?" *Journal of Econometrics* 54 (1–3): 159–78. https://doi.org/10.1016/0304-4076(92)90104-Y.
Land, M. F. 1999. "Motion and Vision: Why Animals Move Their Eyes." *Journal of Comparative Physiology - A Sensory, Neural, and Behavioral Physiology* 185 (4): 341–52. https://doi.org/10.1007/s003590050393.
Lee, Tai Sing, David Mumford, Richard Romero, and Victor A.F. Lamme. 1998. "The Role of the Primary Visual Cortex in Higher Level Vision." *Vision Research* 38 (15–16): 2429–54. https://doi.org/10.1016/S0042-6989(97)00464-1.
Leech, Robert, and David J. Sharp. 2014. "The Role of the Posterior Cingulate Cortex in Cognition and Disease." *Brain* 137 (1): 12–32. https://doi.org/10.1093/brain/awt162.
Li, Fei Fei, Ruffin VanRullen, Christof Koch, and Pietro Perona. 2003. "Natural Scene Categorization in the near Absence of Attention: Further Explorations." *Journal of Vision* 3 (9). https://doi.org/10.1167/3.9.331.
Li, Wai Keung, and A. Ian McLeod. 1981. "Distribution of the Residual Autocorrelations in Multivariate Arma Time Series Models." *Journal of the Royal Statistical Society: Series B (Methodological)* 43 (2): 231–39. https://doi.org/10.1111/j.2517-6161.1981.tb01175.x.
Lin, Fa-Hsuan, Thomas Witzel, Seppo P. Ahlfors, Steven M. Stufflebeam, John W. Belliveau, and Matti S. Hämäläinen. 2006. "Assessing and Improving the Spatial Accuracy in MEG Source Localization by Depth-Weighted Minimum-Norm Estimates." *NeuroImage* 31 (1): 160–71. https://doi.org/10.1016/j.neuroimage.2005.11.054.
Linden, David E.J., David Prvulovic, Elia Formisano, Martin Völlinger, Friedhelm E. Zanella, Rainer Goebel, and Thomas Dierks. 1999. "The Functional Neuroanatomy of Target Detection: An FMRI Study of Visual and Auditory/Oddball Tasks." *Cerebral Cortex* 9 (8): 815–23. https://doi.org/10.1093/cercor/9.8.815.
Lobier, Muriel, Felix Siebenhühner, Satu Palva, and J. Matias Palva. 2014. "Phase Transfer Entropy: A Novel Phase-Based Measure for Directed Connectivity in Networks Coupled by Oscillatory Interactions." *NeuroImage* 85 (January): 853–72. https://doi.org/10.1016/j.neuroimage.2013.08.056.
Löning, Markus, Anthony Bagnall, Sajaysurya Ganesh, Viktor Kazakov, Jason Lines, and Franz J. Király. 2019. "Sktime: A Unified Interface for Machine Learning with Time Series." In *33rd Conference on Neural Information Processing Systems*. Vancouver, Canada. http://arxiv.org/abs/1909.07872.
Lopes Da Silva, Fernando H. 2010. "Electrophysiological Basis of MEG Signals." In

MEG: An Introduction to Methods, edited by Peter Hansen, Morten Kringelbach, and Riitta Salmelin, 1–24. New York, NY: Oxford Scholarship Online. https://doi.org/10.1093/acprof:oso/9780195307238.003.0001.

Luna, Beatriz, Keith R. Thulborn, Magdalena H. Strojwas, Benjamin J. McCurtain, Rebecca A. Berman, Christopher R. Genovese, and John A. Sweeney. 1998. "Dorsal Cortical Regions Subserving Visually Guided Saccades in Humans: An FMRI Study." *Cerebral Cortex* 8 (1): 40–47. https://doi.org/10.1093/cercor/8.1.40.

Lütkepohl, Helmut. 2005. *New Introduction to Multiple Time Series Analysis*. *New Introduction to Multiple Time Series Analysis*. 1st ed. Berlin: Springer-Verlag Berlin Heidelberg. https://doi.org/10.1007/978-3-540-27752-1.

MacKinnon, James. 2010. "Critical Values for Cointegration Tests." *Queen's Economics Department Working Paper No. 1227*, no. January 2010. https://doi.org/10.22004/ag.econ.273723.

Maris, Eric, and Robert Oostenveld. 2007. "Nonparametric Statistical Testing of EEG- and MEG-Data." *Journal of Neuroscience Methods* 164 (1): 177–90. https://doi.org/10.1016/j.jneumeth.2007.03.024.

Marko, H. 1973. "The Bidirectional Communication Theory - A Generalization of Information Theory." *IEEE Transactions on Communications* 21 (12): 1345–51. https://doi.org/10.1109/TCOM.1973.1091610.

Marton, Magda, and Jósef Szirtes. 1988a. "Context Effects on Saccade-Related Brain Potentials to Words during Reading." *Neuropsychologia* 26 (3): 453–63. https://doi.org/10.1016/0028-3932(88)90098-X.

Marton, Magda, and József Szirtes. 1988b. "Saccade-Related Brain Potentials during Reading Correct and Incorrect Versions of Proverbs." *International Journal of Psychophysiology* 6 (4): 273–80. https://doi.org/10.1016/0167-8760(88)90014-1.

Massey, James L. 1990. "Causality, Feedback and Directed Information." In *Proceedings of the International Sympoium on Information Theory and Its Applications*, 27–30. Waikiki, Hawaii.

Maxwell, James Clerk. 1865. "A Dynamical Theory of the Electromagnetic Field." *Philosophical Transactions of the Royal Society of London* 155: 459–512. https://doi.org/10.1098/rstl.1865.0008.

Meghanathan, Radha Nila, Cees van Leeuwen, and Andrey R. Nikolaev. 2015. "Fixation Duration Surpasses Pupil Size as a Measure of Memory Load in Free Viewing." *Frontiers in Human Neuroscience* 8 (JAN): 1–9. https://doi.org/10.3389/fnhum.2014.01063.

Meister, I. G., M. Wienemann, D. Buelte, C. Grünewald, R. Sparing, N. Dambeck, and B. Boroojerdi. 2006. "Hemiextinction Induced by Transcranial Magnetic Stimulation over the Right Temporo-Parietal Junction." *Neuroscience* 142 (1): 119–23. https://doi.org/10.1016/j.neuroscience.2006.06.023.

Milner, David, and Mel Goodale. 2006. *The Visual Brain in Action*. *The Visual Brain in Action*. Vol. 9780198524. OUP Oxford. https://doi.org/10.1093/acprof:oso/9780198524724.001.0001.

Miranda-Dominguez, Oscar, Brian D. Mills, Samuel D. Carpenter, Kathleen A. Grant, Christopher D. Kroenke, Joel T. Nigg, and Damien A. Fair. 2014. "Connectotyping: Model Based Fingerprinting of the Functional Connectome." Edited by Satoru Hayasaka. *PLoS ONE* 9 (11): e111048. https://doi.org/10.1371/journal.pone.0111048.

Morosan, P., J. Rademacher, A. Schleicher, K. Amunts, T. Schormann, and K. Zilles. 2001. “Human Primary Auditory Cortex: Cytoarchitectonic Subdivisions and Mapping into a Spatial Reference System.” *NeuroImage* 13 (4): 684–701. https://doi.org/10.1006/nimg.2000.0715.

Morrow, Alyssa, Vaishaal Shankar, Devin Petersohn, Anthony Joseph, Benjamin Recht, and Nir Yosef. 2017. “Convolutional Kitchen Sinks for Transcription Factor Binding Site Prediction,” no. Iid (May). http://arxiv.org/abs/1706.00125.

Mosher, John. C., Paul S. Lewis, and Richard M. Leahy. 1992. “Multiple Dipole Modeling and Localization from Spatio-Temporal MEG Data.” *IEEE Transactions on Biomedical Engineering* 39 (6): 541–57. https://doi.org/10.1109/10.141192.

Mosher, John C., Richard M. Leahy, and Paul S. Lewis. 1999. “EEG and MEG: Forward Solutions for Inverse Methods.” *IEEE Transactions on Biomedical Engineering* 46 (3): 245–59. https://doi.org/10.1109/10.748978.

Mugler, John P., and James R. Brookeman. 1990. “Three-dimensional Magnetization-prepared Rapid Gradient-echo Imaging (3D MP RAGE).” *Magnetic Resonance in Medicine* 15 (1): 152–57. https://doi.org/10.1002/mrm.1910150117.

Neumaier, Arnold, and Tapio Schneider. 2001. “Estimation of Parameters and Eigenmodes of Multivariate Autoregressive Models.” *ACM Transactions on Mathematical Software* 27 (1): 27–57. https://doi.org/10.1145/382043.382304.

Nikolaev, Andrey R, Radha Nila Meghanathan, and Cees van Leeuwen. 2016. “Combining EEG and Eye Movement Recording in Free Viewing: Pitfalls and Possibilities.” *Brain and Cognition* 107: 55–83. https://doi.org/10.1016/j.bandc.2016.06.004.

Nolte, Guido, Ou Bai, Lewis Wheaton, Zoltan Mari, Sherry Vorbach, and Mark Hallett. 2004. “Identifying True Brain Interaction from EEG Data Using the Imaginary Part of Coherency.” *Clinical Neurophysiology* 115 (10): 2292–2307. https://doi.org/10.1016/j.clinph.2004.04.029.

Nyblom, Jukka. 1989. “Testing for the Constancy of Parameters Over Time.” *Journal of the American Statistical Association* 84 (405): 223. https://doi.org/10.2307/2289867.

Nyström, Marcus, Ignace Hooge, and Richard Andersson. 2016. “Pupil Size Influences the Eye-Tracker Signal during Saccades.” https://doi.org/10.1016/j.visres.2016.01.009.

Ohyama, Tatsuya, William L. Nores, Matthew Murphy, and Michael D. Mauk. 2003. “What the Cerebellum Computes.” *Trends in Neurosciences* 26 (4): 222–27. https://doi.org/10.1016/S0166-2236(03)00054-7.

Oldfield, R. C. 1971. “The Assessment and Analysis of Handedness: The Edinburgh Inventory.” *Neuropsychologia* 9 (1): 97–113. https://doi.org/10.1016/0028-3932(71)90067-4.

Ossandón, José P., Andrea V. Helo, Rodrigo Montefusco-Siegmund, and Pedro E. Maldonado. 2010. “Superposition Model Predicts EEG Occipital Activity during Free Viewing of Natural Scenes.” *Journal of Neuroscience* 30 (13): 4787–95. https://doi.org/10.1523/JNEUROSCI.5769-09.2010.

Over, E. A.B., I. T.C. Hooge, B. N.S. Vlaskamp, and C. J. Erkelens. 2007. “Coarse-to-Fine Eye Movement Strategy in Visual Search.” *Vision Research* 47 (17): 2272–80. https://doi.org/10.1016/j.visres.2007.05.002.

Pannasch, Sebastian, Jens R. Helmert, Katharina Roth, and Henrik Walter. 2008. "Visual Fixation Durations and Saccade Amplitudes : Shifting Relationship in a Variety of Conditions." *Journal of Eye Movement Research* 2 (2): 1–19. https://doi.org/10.16910/jemr.2.2.4.

Parkkonen, Lauri. 2010. "Instrumentation and Data Preprocessing." In *MEG: An Introduction to Methods*, edited by Peter Hansen, Morten Kringelbach, and Riitta Salmelin, 24–64. New York, NY: Oxford Scholarship Online. https://doi.org/10.1093/acprof:oso/9780195307238.003.0002.

Parr, Thomas, M. Berk Mirza, Hayriye Cagnan, and Karl J. Friston. 2019. "Dynamic Causal Modelling of Active Vision." *The Journal of Neuroscience* 39 (32): 6265–75. https://doi.org/10.1523/jneurosci.2459-18.2019.

Parton, Andrew, Parashkev Nachev, Timothy L. Hodgson, Dominic Mort, David Thomas, Roger Ordidge, Paul S. Morgan, Stephen Jackson, Geraint Rees, and Masud Husain. 2007. "Role of the Human Supplementary Eye Field in the Control of Saccadic Eye Movements." *Neuropsychologia* 45 (5): 997–1008. https://doi.org/10.1016/j.neuropsychologia.2006.09.007.

Pascual-Marqui, R. D. 2002. "Standardized Low-Resolution Brain Electromagnetic Tomography (SLORETA): Technical Details." *Methods and Findings in Experimental and Clinical Pharmacology* 24 (SUPPL. D): 5–12.

Pedregosa, Fabian, Gaël Varoquaux, Alexandre Gramfort, Vincent Michel, Bertrand Thirion, Olivier Grisel, Mathieu Blondel, et al. 2011. "Scikit-Learn: Machine Learning in Python." *Journal of Machine Learning Research* 12 (85): 2825–30.

Peirce, Jonathan, Jeremy R. Gray, Sol Simpson, Michael MacAskill, Richard Höchenberger, Hiroyuki Sogo, Erik Kastman, and Jonas Kristoffer Lindeløv. 2019. "PsychoPy2: Experiments in Behavior Made Easy." *Behavior Research Methods* 51 (1): 195–203. https://doi.org/10.3758/s13428-018-01193-y.

Pernet, C. R., M. Latinus, T. E. Nichols, and G. A. Rousselet. 2015. "Cluster-Based Computational Methods for Mass Univariate Analyses of Event-Related Brain Potentials/Fields: A Simulation Study." *Journal of Neuroscience Methods* 250: 85–93. https://doi.org/10.1016/j.jneumeth.2014.08.003.

Perrin, F., J. Pernier, O. Bertrand, and J. F. Echallier. 1989. "Spherical Splines for Scalp Potential and Current Density Mapping." *Electroencephalography and Clinical Neurophysiology* 72 (2): 184–87. https://doi.org/10.1016/0013-4694(89)90180-6.

Petit, L., C. Orssaud, N. Tzourio, G. Salamon, B. Mazoyer, and A. Berthoz. 1993. "PET Study of Voluntary Saccadic Eye Movements in Humans: Basal Ganglia-Thalamocortical System and Cingulate Cortex Involvement." *Journal of Neurophysiology* 69 (4): 1009–17. https://doi.org/10.1152/jn.1993.69.4.1009.

Ploberger, Werner, and Walter Kramer. 1992. "The Cusum Test with Ols Residuals." *Econometrica* 60 (2): 271. https://doi.org/10.2307/2951597.

Rao, Hengyi, Jiongjiong Wang, Kathy Tang, Wei Pan, and John A. Detre. 2007. "Imaging Brain Activity during Natural Vision Using CASL Perfusion FMRI." *Human Brain Mapping* 28 (7): 593–601. https://doi.org/10.1002/hbm.20288.

Robinson, Stephen E. 1989. "Environmental Noise Cancellation for Biomagnetic Measurements." *Advances in Biomagnetism*, no. 11: 721–24. https://doi.org/10.1007/978-1-4613-0581-1_162.

Rocca, D. La, P. Campisi, B. Vegso, P. Cserti, G. Kozmann, F. Babiloni, and F. De Vico Fallani. 2014. "Human Brain Distinctiveness Based on EEG Spectral Coherence Connectivity." *IEEE Transactions on Biomedical Engineering* 61 (9): 2406–12.

https://doi.org/10.1109/TBME.2014.2317881.
Rosenberg, Monica D., Dustin Scheinost, Abigail S. Greene, Emily W. Avery, Young Hye Kwon, Emily S. Finn, Ramachandran Ramani, Maolin Qiu, R. Todd Constable, and Marvin M. Chun. 2020. "Functional Connectivity Predicts Changes in Attention Observed across Minutes, Days, and Months." *Proceedings of the National Academy of Sciences* 117 (7): 3797–3807. https://doi.org/10.1073/pnas.1912226117.
Roskies, A. L. 1999. "The Binding Problem." *Neuron* 24 (1): 7–9. https://doi.org/10.1016/S0896-6273(00)80817-X.
Ruiz, Alejandro Pasos, Michael Flynn, James Large, Matthew Middlehurst, and Anthony Bagnall. 2021. *The Great Multivariate Time Series Classification Bake off: A Review and Experimental Evaluation of Recent Algorithmic Advances*. *Data Mining and Knowledge Discovery*. Vol. 35. Springer US. https://doi.org/10.1007/s10618-020-00727-3.
Rutecki, Paul A. 1992. "Neuronal Excitability: Voltage-Dependent Currents and Synaptic Transmission." *Journal of Clinical Neurophysiology*. https://doi.org/10.1097/00004691-199204010-00003.
Sareen, Ekansh, Sélima Zahar, Dimitri Van De Ville, Anubha Gupta, Alessandra Griffa, and Enrico Amico. 2021. "Exploring MEG Brain Fingerprints: Evaluation, Pitfalls, and Interpretations." *NeuroImage* 240: 118331. https://doi.org/10.1016/j.neuroimage.2021.118331.
Sarvas, Jukka. 1987. "Basic Mathematical and Electromagnetic Concepts of the Biomagnetic Inverse Problem." *Physics in Medicine and Biology* 32 (1): 11–22. https://doi.org/10.1088/0031-9155/32/1/004.
Saxe, Andrew M, Pang Wei Koh, Zhenghao Chen, Maneesh Bhand, Bipin Suresh, and Andrew Y Ng. 2011. "On Random Weights and Unsupervised Feature Learning." In *Proceedings of the 28th International Conference on Machine Learning*, 1089–96. Bellevue, WA, USA: Omnipress, USA.
Schlag, J., and M. Schlag-Rey. 1987. "Evidence for a Supplementary Eye Field." *Journal of Neurophysiology* 57 (1): 179–200. https://doi.org/10.1152/jn.1987.57.1.179.
———. 1992. "Neurophysiology of Eye Movements." *Advances in Neurology* 57: 135–47. https://doi.org/10.1016/b978-0-12-071050-8.50006-9.
Schlögl, Alois, and Gernot Supp. 2006. "Analyzing Event-Related EEG Data with Multivariate Autoregressive Parameters." In *Progress in Brain Research, Vol. 159*, 135–47.
Schwarz, Gideon. 1978. "Estimating the Dimension of a Model." *The Annals of Statistics* 6 (2): 461–64. https://doi.org/10.1214/aos/1176344136.
Seabold, Skipper, and Josef Perktold. 2010. "Statsmodels: Econometric and Statistical Modeling with Python." In *Proceedings of the 9th Python in Science Conference*, edited by S van der Walt and Jarrod Millman, 92–96. Austin, Texas. https://doi.org/10.25080/Majora-92bf1922-011.
Seidkhani, Hossein, Andrey R. Nikolaev, Radha Nila Meghanathan, Hamid Pezeshk, Ali Masoudi-Nejad, and Cees van Leeuwen. 2017. "Task Modulates Functional Connectivity Networks in Free Viewing Behavior." *NeuroImage* 159 (July): 289–301. https://doi.org/10.1016/j.neuroimage.2017.07.066.
Shulman, Gordon L., Serguei V. Astafiev, Mark P. McAvoy, Giovanni D'Avossa, and Maurizio Corbetta. 2007. "Right TPJ Deactivation during Visual Search: Functional Significance and Support for a Filter Hypothesis." *Cerebral Cortex* 17

(11): 2625–33. https://doi.org/10.1093/cercor/bhl170.
Shulman, Gordon L., Daniel L.W. Pope, Serguei V. Astafiev, Mark P. McAvoy, Abraham Z. Snyder, and Maurizio Corbetta. 2010. "Right Hemisphere Dominance during Spatial Selective Attention and Target Detection Occurs Outside the Dorsal Frontoparietal Network." *Journal of Neuroscience* 30 (10): 3640–51. https://doi.org/10.1523/JNEUROSCI.4085-09.2010.
Silva Castanheira, Jason da, Hector Domingo Orozco Perez, Bratislav Misic, and Sylvain Baillet. 2021a. "Brief Segments of Neurophysiological Activity Enable Individual Differentiation." *Nature Communications* 12 (1): 1–11. https://doi.org/10.1038/s41467-021-25895-8.
———. 2021b. "MEG, Myself, and I: Individual Identification from Neurophysiological 1 Brain Activity." *BioRxiv*, 2021.02.18.431803. https://doi.org/10.1101/2021.02.18.431803.
Silvetti, Massimo, Stefano Lasaponara, Francesca Lecce, Alessio Dragone, Emiliano Macaluso, and Fabrizio Doricchi. 2016. "The Response of the Left Ventral Attentional System to Invalid Targets and Its Implication for the Spatial Neglect Syndrome: A Multivariate Fmri Investigation." *Cerebral Cortex* 26 (12): 4551–62. https://doi.org/10.1093/cercor/bhv208.
Snow, Jacqueline C., and Jody C. Culham. 2021. "The Treachery of Images: How Realism Influences Brain and Behavior." *Trends in Cognitive Sciences* 25 (6): 506–19. https://doi.org/10.1016/j.tics.2021.02.008.
Snow, Jacqueline C., Charles E. Pettypiece, Teresa D. McAdam, Adam D. McLean, Patrick W. Stroman, Melvyn A. Goodale, and Jody C. Culham. 2011. "Bringing the Real World into the FMRI Scanner: Repetition Effects for Pictures versus Real Objects." *Scientific Reports* 1: 1–10. https://doi.org/10.1038/srep00130.
Sobel, Kenith V., Matthew P. Gerrie, Bradley J. Poole, and Michael J. Kane. 2007. "Individual Differences in Working Memory Capacity and Visual Search: The Roles of Top-down and Bottom-up Processing." *Psychonomic Bulletin and Review* 14 (5): 840–45. https://doi.org/10.3758/BF03194109.
Sonkusare, Saurabh, Michael Breakspear, and Christine Guo. 2019. "Naturalistic Stimuli in Neuroscience: Critically Acclaimed." *Trends in Cognitive Sciences* 23 (8): 699–714. https://doi.org/10.1016/j.tics.2019.05.004.
Souza Rodrigues, Júlia de, Fernanda Lenita Ribeiro, João Ricardo Sato, Rickson Coelho Mesquita, and Claudinei Eduardo Biazoli Júnior. 2019. "Identifying Individuals Using FNIRS-Based Cortical Connectomes." *Biomedical Optics Express* 10 (6): 2889. https://doi.org/10.1364/boe.10.002889.
SR Research Ltd. 2009. "EyeLink® 1000 User Manual v1.5.0." Mississauga, Ontario, Canada.
Stein, Richard B., E. Roderich Gossen, and Kelvin E. Jones. 2005. "Neuronal Variability: Noise or Part of the Signal?" *Nature Reviews Neuroscience* 6 (5): 389–97. https://doi.org/10.1038/nrn1668.
Stewart, Emma E.M., and Alexander C. Schütz. 2018. "Attention Modulates Trans-Saccadic Integration." *Vision Research* 142 (November 2017): 1–10. https://doi.org/10.1016/j.visres.2017.11.006.
Stuphorn, Veit. 2015. "The Role of Supplementary Eye Field in Goal-Directed Behavior." *Journal of Physiology Paris* 109 (1–3): 118–28. https://doi.org/10.1016/j.jphysparis.2015.02.002.
Tanji, Jun. 1994. "The Supplementary Motor Area in the Cerebral Cortex." *Neuroscience Research* 19 (3): 251–68. https://doi.org/10.1016/0168-

0102(94)90038-8.
Tatler, Benjamin W., and Benjamin T. Vincent. 2008. “Systematic Tendencies in Scene Viewing.” *Journal of Eye Movement Research* 2 (2): 1–18. https://doi.org/10.16910/jemr.2.2.5.
Tehovnik, Edward J. 1995. “The Dorsomedial Frontal Cortex: Eye and Forelimb Fields.” *Behavioural Brain Research* 67 (2): 147–63. https://doi.org/10.1016/0166-4328(94)00151-5.
Tesche, Claudia D., and John Clarke. 1977. “Dc SQUID: Noise and Optimization.” *Journal of Low Temperature Physics* 29 (3–4): 301–31. https://doi.org/10.1007/BF00655097.
Theeuwes, Jan. 2010. “Top-down and Bottom-up Control of Visual Selection.” *Acta Psychologica* 135 (2): 77–99. https://doi.org/10.1016/j.actpsy.2010.02.006.
———. 2014. “Spatial Orienting and Attentional Capture.” In *The Oxford Handbook of Attention*, edited by Anna C. (Kia) Nobre and Sabine Kastner. Oxford University Press. https://doi.org/10.1093/oxfordhb/9780199675111.013.005.
Thickbroom, G. W., W. Knezevič, W. M. Carroll, and F. L. Mastaglia. 1991. “Saccade Onset and Offset Lambda Waves: Relation to Pattern Movement Visually Evoked Potentials.” *Brain Research* 551 (1–2): 150–56. https://doi.org/10.1016/0006-8993(91)90927-N.
Thickbroom, G W, and L Mastaglia. 1985. “Presaccadic ’ Spike ’ Potential : Investigation of Topography and Source Opisthochronic Averaging EEG Recording.” *Science* 339: 271–80.
Ticini, Luca F. 2013. “On the Debated Role of Temporo-Parietal Dysfunction in Patients with Basal Ganglia Neglect.” *Frontiers in Behavioral Neuroscience* 50 (NOV): 561–66. https://doi.org/10.3389/fnbeh.2013.00168.
Tootell, Roger B.H., Nouchine K. Hadjikhani, Wim Vanduffel, Arthur K. Liu, Janine D. Mendola, Martin I. Sereno, and Anders M. Dale. 1998. “Functional Analysis of Primary Visual Cortex (V1) in Humans.” *Proceedings of the National Academy of Sciences of the United States of America* 95 (3): 811–17. https://doi.org/10.1073/pnas.95.3.811.
Treisman, Anne M. 1982. “Perceptual Grouping and Attention in Visual Search for Features and for Objects.” *Journal of Experimental Psychology: Human Perception and Performance* 8 (2): 194–214. https://doi.org/10.1037/0096-1523.8.2.194.
———. 1996. “The Binding Problem.” *Current Opinion in Neurobiology* 6 (2): 171–78. https://doi.org/10.1016/S0959-4388(96)80070-5.
Treisman, Anne M., and Garry Gelade. 1980. “A Feature-Integration Theory of Attention.” *Cognitive Psychology* 12 (1): 97–136. https://doi.org/10.1016/0010-0285(80)90005-5.
Uchida, Naoshige, and Zachary F. Mainen. 2003. “Speed and Accuracy of Olfactory Discrimination in the Rat.” *Nature Neuroscience* 6 (11): 1224–29. https://doi.org/10.1038/nn1142.
Uddin, Lucina Q. 2020. “Bring the Noise: Reconceptualizing Spontaneous Neural Activity.” *Trends in Cognitive Sciences* 24 (9): 734–46. https://doi.org/10.1016/j.tics.2020.06.003.
Uddin, Lucina Q., Jason S. Nomi, Benjamin Hébert-Seropian, Jimmy Ghaziri, and Olivier Boucher. 2017. “Structure and Function of the Human Insula.” *Journal of Clinical Neurophysiology* 34 (4): 300–306.

https://doi.org/10.1097/WNP.0000000000000377.
Unema, Pieter J.A., Sebastian Pannasch, Markus Joos, and Boris M. Velichkovsky. 2005. "Time Course of Information Processing during Scene Perception: The Relationship between Saccade Amplitude and Fixation Duration." *Visual Cognition* 12 (3): 473–94. https://doi.org/10.1080/13506280444000409.
Valizadeh, Seyed Abolfazl, Franziskus Liem, Susan Mérillat, Jürgen Hänggi, and Lutz Jäncke. 2018. "Identification of Individual Subjects on the Basis of Their Brain Anatomical Features." *Scientific Reports* 8 (1): 1–9. https://doi.org/10.1038/s41598-018-23696-6.
Veen, Barry D. Van, Wim Van Drongelen, Moshe Yuchtman, and Akifumi Suzuki. 1997. "Localization of Brain Electrical Activity via Linearly Constrained Minimum Variance Spatial Filtering." *IEEE Transactions on Biomedical Engineering* 44 (9): 867–80. https://doi.org/10.1109/10.623056.
Vilberg, Kaia L., and Michael D. Rugg. 2008. "Memory Retrieval and the Parietal Cortex: A Review of Evidence from a Dual-Process Perspective." *Neuropsychologia* 46 (7): 1787–99. https://doi.org/10.1016/j.neuropsychologia.2008.01.004.
Vinje, William E., and Jack L. Gallant. 2000. "Sparse Coding and Decorrelation in Primary Visual Cortex during Natural Vision." *Science* 287 (5456): 1273–76. https://doi.org/10.1126/science.287.5456.1273.
Vrba, J., A. A. Fife, M. B. Burbank, H. Wienberg, and P. A. Brickett. 1982. "Spatial Discrimination in Squid Gradiometers and 3Rd Order Gradiometer Performance." *Canadian Journal of Physics* 60 (7): 1060–73. https://doi.org/10.1139/p82-144.
Wachinger, Christian, Polina Golland, William Kremen, Bruce Fischl, and Martin Reuter. 2015. "BrainPrint: A Discriminative Characterization of Brain Morphology." *NeuroImage* 109: 232–48. https://doi.org/10.1016/j.neuroimage.2015.01.032.
Waller, Lea, Henrik Walter, Johann D. Kruschwitz, Lucia Reuter, Sabine Müller, Susanne Erk, and Ilya M. Veer. 2017. "Evaluating the Replicability, Specificity, and Generalizability of Connectome Fingerprints." *NeuroImage* 158 (May): 371–77. https://doi.org/10.1016/j.neuroimage.2017.07.016.
Wang, Liang, Ryan E.B. Mruczek, Michael J. Arcaro, and Sabine Kastner. 2015. "Probabilistic Maps of Visual Topography in Human Cortex." *Cerebral Cortex* 25 (10): 3911–31. https://doi.org/10.1093/cercor/bhu277.
Weinstock, Harold. 1996. *SQUID Sensors: Fundamentals, Fabrication and Applications*. Edited by Harold Weinstock. *SQUID Sensors: Fundamentals, Fabrication and Applications*. Dordrecht: Springer Netherlands. https://doi.org/10.1007/978-94-011-5674-5.
Welch, B. L. 1947. "The Generalisation of Student's Problems When Several Different Population Variances Are Involved." *Biometrika* 34 (1–2): 28–35. https://doi.org/10.1093/biomet/34.1-2.28.
Wen, Zhenfu, Tianyou Yu, Xinbin Yang, and Yuanqing Li. 2019. "Goal-Directed Processing of Naturalistic Stimuli Modulates Large-Scale Functional Connectivity." *Frontiers in Neuroscience* 12 (January): 1–12. https://doi.org/10.3389/fnins.2018.01003.
Wiener, Norbert. 1949. *Extrapolation, Interpolation, and Smoothing of Stationary Time Series*. *Extrapolation, Interpolation, and Smoothing of Stationary Time Series*. New York, NY, USA: The MIT Press.

https://doi.org/10.7551/mitpress/2946.001.0001.
———. 1956. “The Theory of Prediction.” In *Modern Mathematics for Engineers*, 58:323–29. New York, NY: McGraw-Hill.
Winkler, Irene, Stefan Debener, Klaus-Robert Muller, and Michael Tangermann. 2015. “On the Influence of High-Pass Filtering on ICA-Based Artifact Reduction in EEG-ERP.” In *2015 37th Annual International Conference of the IEEE Engineering in Medicine and Biology Society (EMBC)*, 2015-Novem:4101–5. Milan, Italy: IEEE. https://doi.org/10.1109/EMBC.2015.7319296.
Wolfe, Jeremy M. 1994a. “Guided Search 2.0 A Revised Model of Visual Search.” *Psychonomic Bulletin & Review* 1 (2): 202–38. https://doi.org/10.3758/BF03200774.
———. 1994b. “Visual Search in Continuous, Naturalistic Stimuli.” *Vision Research* 34 (9): 1187–95. https://doi.org/10.1016/0042-6989(94)90300-X.
———. 2014. “Approaches to Visual Search.” In *The Oxford Handbook of Attention*, edited by Anna C. (Kia) Nobre and Sabine Kastner. Oxford University Press. https://doi.org/10.1093/oxfordhb/9780199675111.013.002.
———. 2021. “Guided Search 6.0: An Updated Model of Visual Search.” *Psychonomic Bulletin and Review* 28 (4): 1060–92. https://doi.org/10.3758/s13423-020-01859-9.
Wolters, C. H., L. Grasedyck, and W. Hackbusch. 2004. “Efficient Computation of Lead Field Bases and Influence Matrix for the FEM-Based EEG and MEG Inverse Problem.” *Inverse Problems* 20 (4): 1099–1116. https://doi.org/10.1088/0266-5611/20/4/007.
Yagi, Akihiro. 1981. “Visual Signal Detection and Lambda Responses.” *Electroencephalography and Clinical Neurophysiology* 52 (6): 604–10. https://doi.org/10.1016/0013-4694(81)91434-6.
Yamashita, Masahiro, Yujiro Yoshihara, Ryuichiro Hashimoto, Noriaki Yahata, Naho Ichikawa, Yuki Sakai, Takashi Yamada, et al. 2018. “A Prediction Model of Working Memory across Health and Psychiatric Disease Using Whole-Brain Functional Connectivity.” *ELife* 7 (December). https://doi.org/10.7554/eLife.38844.
Yang, Qiang, and Xindong Wu. 2006. “10 CHALLENGING PROBLEMS IN DATA MINING RESEARCH.” *International Journal of Information Technology & Decision Making* 05 (04): 597–604. https://doi.org/10.1142/S0219622006002258.
Yoo, Kwangsun, Monica D. Rosenberg, Wei-Ting Hsu, Sheng Zhang, Chiang-Shan R. Li, Dustin Scheinost, R. Todd Constable, and Marvin M. Chun. 2018. “Connectome-Based Predictive Modeling of Attention: Comparing Different Functional Connectivity Features and Prediction Methods across Datasets.” *NeuroImage* 167 (February): 11–22. https://doi.org/10.1016/j.neuroimage.2017.11.010.
Yosinski, Jason, Jeff Clune, Yoshua Bengio, and Hod Lipson. 2014. “How Transferable Are Features in Deep Neural Networks?” *Advances in Neural Information Processing Systems* 4 (January): 3320–28.
Yu, Fisher, and Vladlen Koltun. 2016. “Multi-Scale Context Aggregation by Dilated Convolutions.” *Fourth International Conference on Learning Representations*, November. http://arxiv.org/abs/1511.07122.
Zeiler, Matthew D., and Rob Fergus. 2014. “Visualizing and Understanding Convolutional Networks.” In , 818–33. https://doi.org/10.1007/978-3-319-

10590-1_53.
Zeki, S., J. D.G. Watson, C. J. Lueck, Karl J. Friston, C. Kennard, and R. S.J. Frackowiak. 1991. “A Direct Demonstration of Functional Specialization in Human Visual Cortex.” *Journal of Neuroscience* 11 (3): 641–49. https://doi.org/10.1523/jneurosci.11-03-00641.1991.
Zimmerman, J. E., Paul Thiene, and J. T. Harding. 1970. “Design and Operation of Stable Rf-Biased Superconducting Point-Contact Quantum Devices, and a Note on the Properties of Perfectly Clean Metal Contacts.” *Journal of Applied Physics* 41 (4): 1572–80. https://doi.org/10.1063/1.1659074.

ACKNOWLEDGEMENTS

Over the course of this dissertation, I was supported by many great people:

I would like to start by saying thank you to Prof. Dr. N. Jon Shah, my doctoral adviser, who provided the resources for this project. Furthermore, I would like to thank him and Prof. Dr. Ansgar Steland for a critical review of this dissertation.

Then, I would like to particularly thank my immediate supervisors Prof. Dr. Sonja Grün and Dr. Jürgen Dammers. Thank you for choosing me for this fascinating project. You have always been there for me to ask questions and you have guided me with your wisdom and expertise. Without you, this project would not have been possible.

Similarly, I would like to thank Dr. Junji Ito. In our meetings with Sonja and Jürgen, your contributions were highly valued. Moreover, your critical thinking and ideas were immensely helpful for the success of this project. During the writing process of our manuscript, I was amazed by your ability to break down the complex nature of the project and help me formulate my thoughts and ideas in a clear and concise manner.

Furthermore, I would like to thank PD Dr. Ralph Weider. In a group consisting mostly of physicists, your expertise was most welcome and helped shape the interpretation of our results.

A special thanks is dedicated to the members of AG Dammers. In particular, I would like to thank Dr. Eberhard Eich for our numerous discussions and his deep pool of knowledge regarding MEG, Praveen Sripad for his advice regarding all things related to Python, Linux, and connectivity, and Frank Boers and Andrea Muren for their help in setting up and performing the experiment.

Finally, I would like to thank my family for their support and their love. A special thanks goes out to my parents for providing me with an office during the pandemic that more closely resembled a hotel with room and board. But most importantly, I would like to thank my wife.